

**Removal of C and SiC
from Si and FeSi
during
ladle refining and solidification**

Dr.ing. thesis

Ole Svein Klevan
January, 1997



Department of Metallurgy
The Norwegian University of Science and Technology
MI-rapport 1997:40

This thesis has been submitted to the Department of Metallurgy, The Norwegian University of Science and Technology (NTNU), in partial fulfilment of the requirements for the doctoral degree "Doktor Ingeniør".

Preface

This doctoral thesis mainly concerns total carbon removal from silicon and ferrosilicon. The decarburization includes removal of SiC particles by stirring and during casting in addition to reduction of dissolved carbon by gas purging. The work has been carried out at the Department of Metallurgy, the Norwegian University of Science and Technology (NTNU), Trondheim. The industrial experiments were performed at Elkem Thamshavn, Orkanger.

I am grateful for the opportunity given me to carry out this work by my employer Elkem Thamshavn. Special thanks to plant manager Einar M. Skjølberg for his support making it possible for me to accomplish this work. The people at the tapping area at both furnaces at Elkem Thamshavn are thanked for their assistance and patient during the industrial trials. The interest in research and development by the people at the plant is very much appreciated.

Mr. Leif Kristiansen has been of invaluable assistance during the experiments. His enthusiasm and interest during this work are very much appreciated. All the carbon analyses have been performed at the laboratory at Elkem Thamshavn, and Svein Svorkmo is to be thanked.

The support and valuable comments and advice from Dr. Halvard Tveit is acknowledged. Dr. Eirik Bathen is acknowledged for his conscientious work on image analysis and Dr. Frede Frisvold for his assistance with the calculation of the number size distributions, and for his constructive suggestions on writing this part of the thesis. Prof. Johan Kr. Tuset is to be thanked for his valuable advice when compiling the thermodynamic data and Prof. Bo Lindqvist is acknowledged for advice with the statistical part.

My supervisor during these years has been Prof. Thorvald A. Engh, whom I owe my debt of gratitude. It has been encouraging to discuss with him, and I feel that my confidence as a researcher has grown from working with him.

I am grateful for the support and understanding my wife Jorunn has shown me during these years.

Finally, it should be mentioned that references [1] and [2] have been published. Reference [3] has been submitted for Infacon 1998.

1. Klevan, O. S. and Engh, T. A., "Dissolved Impurities and Inclusions in FeSi and Si, Development of a Filter Sampler", *INFACON 7, Proceedings of the 7th International Ferroalloys Congress*, FFF, Trondheim (1995), pp. 441 - 451.
2. Bakke, P. and Klevan, O. S., "Thermodynamics of Liquid Silicon Bases Alloys," *Process Technology Conference Proceedings*, Vol. 14, ISS (1995), pp. 155-165
3. Klevan, O. S. and Engh, T. A., "Removal of Carbon from Liquid Silicon and Ferrosilicon", *INFACON 8*, Beijing (1998).

Table of Contents

Preface	iii
List of Symbols	xi
Abstract	xiii
1. Introduction	1
1.1 Liquid metal refining of silicon and ferrosilicon	7
1.2 Carbon in some commercial types of FeSi75	8
References	16
2. Thermodynamic and Physical Data	19
2.1 Introduction	19
2.2 Thermodynamics of liquid silicon-based alloys	19
2.3 Thermal and physical data of silicon and ferrosilicon	31
2.3.1 Density	31
2.3.2 Heat capacity and enthalpy	35
2.3.3 Surface and interfacial tension	39
2.3.4 Viscosity	42
2.3.5 Electrical and thermal conductivity	43
2.4 Thermal and physical data and wettability of silicon carbide	45
2.4.1 Density	45
2.4.2 Specific heat capacity	47
2.4.3 Thermal conductivity	48
2.4.4 Wettability of SiC	49
References for chapter 2.3 and 2.4	52
3. Sampling of Ferrosilicon for C-Analyses	55
3.1 Stream sampling	55

3.2 Sampling in the ladle during metal treatment - Immersion sampling	58
3.3. Sampling statistics	61
3.4 Inclusion filter sampling	64
3.4.1 Automatic image analysis	67
3.4.2 Filter sampling of ferrosilicon from production runs	69
References	75
4. Removal of C from Silicon and Ferrosilicon	76
4.1 Decarburization of silicon and ferrosilicon melts	76
4.1.1 The rate of decarburization	78
4.1.2 Numerical solution of the decarburization rate	85
4.2 Physical removal of SiC particles to slag and lining	94
4.2.1 Removal by settling	94
4.2.2 Turbulent removal to walls and top slag	94
4.3 Experimental setup and results	95
4.3.1 Carbon removal by pouring from one ladle to another and bottom plug stirring.	95
4.3.2 Carbon removal by gas stirring with refractory lance	109
4.3.3 Comparison between the results from stirring with plug and lance.	112
4.4 Change in carbon during casting, solidification and crushing and screening	113
4.4.1 Oxidation of C and SiC during teeming	114
4.4.2 Segregation	114
4.4.3 Pushing of SiC particles by the solidification front	118
4.4.4 Transfer of SiC particles to an oxidic phase	119
References	123
5. Discussion	125
5.1 Particle pushing or particle engulfment	125
5.2 Sampling of liquid (ferro)silicon	130
5.3 Filter sampling of ferrosilicon	132
5.4 Removal of C from liquid Si and FeSi	133
5.4.1 Decarburization model	133

5.4.2 Removal of particles to wall by stirring	135
5.4.3 Removal of carbon during casting, solidification and crushing and screening	136
References	137
6. Conclusions	139
Appendix A: Statistics	141
Appendix B: Saltykov's Table	146
Appendix C: Numerical solution of eqn (4.26) - Powersim Model	147
Appendix D: Rising Velocity of Bubbles in Liquids	157
Appendix E: Turbulent Removal of Particles and Specific Stirring Power . .	161
Appendix F: Fe-Si Phase-Diagram	166
Appendix G: Chemical analyses of fines and lumpy FeSi75	167

List of Symbols

A	constant = $\frac{V\rho_{\text{melt}}}{M_C 100 \dot{G}_{\text{inert}}}$	s
A_0	Surface area occupied by one adsorbed molecule of gas	
A_b	Bubble surface area	m^2
a_i	activity of component i	
a	radius of particle or inclusion	m
a_0	lattice constant	m
B	constant = $\frac{a_{\text{Si}}^{1/2}}{a_{\text{SiO}_2}^{1/2} f_C K_{6.5}}$	
C	constant	
$c(a)$	number of inclusion of diameter $2a$ per unit volume	m^{-3}
c_l	concentration in liquid	
c_m	concentration of particles per unit amount of melt	
c_v	concentration of particles per unit volume of melt	
c_p	specific heat capacity	$\text{J K}^{-1} \text{mol}^{-1}$
c_s	concentration in solid	
D	diffusion coefficient	$\text{m}^2 \text{s}^{-1}$
d	diameter, inclusion diameter	m, μm
d_p	particle radius	m, μm
d_b	equivalent bubble diameter	m
d_0	interatomic distance	m
e	protrusion height	m
e	1st order interaction coefficient	
\dot{G}_{inert}	flow of inert gas	kmol s^{-1}
g	acceleration of gravity	9.81 m s^{-2}
H	height of bath	m
	or enthalpy	J

ΔH_f	heat of formation	J mol ⁻¹
ΔH_{mix}	heat of mixing	J mol ⁻¹
ΔH_m	heat of melting	J mol ⁻¹
h_j	the distance where size distribution $n_A(d_p, z_j)$ is valid	m
i	component i	
j	component j	
K	constant or equilibrium constant	
k	Boltzmann's constant	1.38×10 ⁻²³ J K ⁻¹
k_C	mass transfer coefficient for carbon	m s ⁻¹
k_{eq}	equilibrium segregation coefficient	
k_{eff}	effective segregation coefficient	
L	Lorenz number = $\lambda \rho_e / T$	WΩK ⁻²
l_e	characteristic length of energy containing eddies	m
M	mass of metal bath or Morton number, $M = g\mu^4 \Delta\rho / \rho^2 \sigma^3$	kg
M_i	molar weight of component i	g mol ⁻¹ , kg kmol ⁻¹
m_{melt}	amount of melt	kg
n	integer or number	
\dot{n}_a	flux of inclusion of size a	m ⁻³ s ⁻¹
$n_A(d_p, z_j)$	averaged size distribution of inclusions of size d_i and at depth z_j per unit melt area and depth in the filter	m ⁻² m ⁻¹
N_b	number of bubbles	
\dot{N}_b	number of bubbles produced per second	s ⁻¹
N_A	Avogadro's number	6.022 14×10 ²³ atoms mol ⁻¹
$N_A(d_i)$	number size distribution of inclusions per unit melt area	m ⁻²
$N_V(d_i)$	number size distribution of inclusions per unit melt volume	m ⁻³
p	pressure	bar, N m ⁻²
p_{CO}	partial pressure of CO	bar, N m ⁻²
p_{in}	inlet pressure	bar, N m ⁻²
p_{inert}	partial pressure of inert gas	bar, N m ⁻²
p_o	outlet pressure	bar, N m ⁻²
p_0	saturation pressure	
p_{tot}	total pressure	bar, N m ⁻²
\dot{Q}_{inert}	flow of inert gas	Nl min ⁻¹ , Nm ³ h ⁻¹
Re	Reynolds number	

r	second order interaction coefficient	
r_p	particle radius	m, μm
SD_x	standard deviation	
\bar{s}_x	standard error of mean	
T	temperature	$^{\circ}\text{C}$, K
T_{in}	initial temperature	$^{\circ}\text{C}$, K
t	time	s
u	velocity, velocity of a solidification front (growth velocity)	m s^{-1}
u_b	velocity of a single bubble	m s^{-1}
u_{cr}	critical growth velocity	m s^{-1}
u_m	mean velocity in melt	m s^{-1}
u_r	terminal velocity of raising particle	m s^{-1}
u_0	shear velocity along wall	m s^{-1}
V	volume or coefficient of variation	m^3
V_m	molar volume	$\text{m}^3 \text{mol}^{-1}$
V_{melt}	volume of melt	m^3
W	weight	kg or mt
X_i	mole fraction of component i	
\bar{X}	mean value	
x	variable	
z	dimensionless variable or vertical position	m

Greek letters

α	thermal diffusivity	
$\alpha_{i,j}$	Saltykov's weights for relating the number size distribution in a polydispersed system in two dimensions to the number size distribution per volume	
Δ	width of particle size class	m
δ_b	thickness of turbulent wall boundary layer	m
δ_1	thickness of restricted turbulent boundary layer	m
δ_2	thickness of viscous (laminar flow) boundary layer	m

ε	first order interaction coefficient	
$\dot{\varepsilon}$	specific stirring power	$\text{m}^2 \text{s}^{-3}$
Γ	molar surface area	mol m^{-2}
μ	dynamic viscosity	Ns m^{-2}
	or chemical potential	J
λ	thermal conductivity	$\text{Wm}^{-1}\text{K}^{-1}$
ν	kinematic viscosity	$\text{m}^2 \text{s}^{-1}$
ρ	density	$\text{gcm}^{-3}, \text{kg m}^{-3}$
ρ_{melt}	density of melt	kg m^{-3}
ρ_{m}	density at the melting point	g cm^{-3}
ρ_{FeSi75}	density of liquid ferrosilicon with 75 mass% Si	3185 kg m^{-3}
ρ_{e}	electrical resistivity	Ωm
ρ_{p}	density of particles	g cm^{-3}
σ	surface tension	mN m^{-1}
σ_{ps}	surface tension between particle and solid	mN m^{-1}
σ_{pl}	surface tension between particle and liquid	mN m^{-1}
σ_{sl}	surface tension between solid and liquid	mN m^{-1}
σ_{pv}	surface tension between particle and vapour	mN m^{-1}
σ_{lv}	surface tension between liquid and vapour	mN m^{-1}
σ_{sv}	surface tension between solid and vapour	mN m^{-1}
τ_{b}	residence time for a bubble in the bath	s
θ	contact angle	
ϕ	friction factor	
ϕ_{A}	dimensionless group for contact area of bubbles	

Abstract

Silicon and ferrosilicon produced by carbothermic reduction in submerged electric arc furnaces unavoidably contain impurities. Customer requirements with respect to chemical composition become steadily more strict. Thus, greater emphasis is required on control and removal of dissolved elements and inclusions from silicon and ferrosilicon. To model and understand the limitations of ladle refining processes, physical and thermodynamic data has been collected for silicon and ferrosilicon. Ferrosilicon is regarded as a Si alloy. The solubility of carbon in silicon and ferrosilicon in equilibrium with SiC(s) becomes:

$$\log[\%C]_{\text{Si(l)}} = 3.53 - \frac{9,736}{T} \quad [\text{mass}\%]$$

$$\log[\%C]_{\text{FeSi75(l)}} = 3.5 - \frac{10,003}{T} \quad [\text{mass}\%]$$

Also, some physical data for SiC has been collected and presented. The density at 1450 °C was calculated to be 3.13 g/cm³. This is close to the density of liquid ferrosilicon with 75 mass% silicon (FeSi75), $\rho_{\text{FeSi75}}(1450 \text{ °C}) = 3.185 \text{ g/cm}^3$. Employing Stoke's equation, this indicates that SiC particles in practice cannot be removed by settling.

Carbon is present in silicon and ferrosilicon as dissolved carbon and SiC particles. The metal temperature in the furnace hearth is estimated to be between 1800 and 2000 °C. Extrapolating the above data for carbon solubility gives 1000 ppm C at 1950 °C for FeSi75. This is in reasonable accordance with the total carbon content of 700-1100 ppm found in liquid ferrosilicon (FeSi75) out of the furnace.

The total carbon found in the final product depends on type of secondary treatment - refining and casting. A statistical treatment of 779 shipments of ferrosilicon from Elkem Thamshavn over a period of three years has been performed, showing that

average total carbon in standard lumpy FeSi75 was 301 ppm, whereas the average figures for granulated and refined ferrosilicon were 211 and 118 ppm respectively. The variation in total carbon content expressed as the coefficient of variation, $V = SD_x/\bar{x}$, was analysed to be 0.37 for Gransil and 0.4 for refined FeSi75, whereas for the standard lumpy grade $V = 0.67$.

Sampling is a problem when examining the total carbon content in liquid (ferro)silicon. The existing sampling methods using graphite scoops in normal operation were not suitable. It was necessary to develop sampling methods for measuring total carbon. A Minco immersion sampler gives a rapid solidification of the melt that minimizes the segregation of dissolved elements in the specimen. This sampler also seems to give engulfment of silicon carbide particles present in the melt and thus should provide the correct value for total carbon.

An oxidic scoop sampler made of chamotte was tested. It underestimated the total carbon content in the alloy due to transfer of SiC particles to the scoop wall. Samples of the wall of the scoop including the deposited metal layer were analysed by Microprobe Analyser (EPMA). The X-ray mapping pictures demonstrated that SiC-particles had penetrated into the oxidic wall. The wettability of SiC particles by Al_2O_3 - SiO_2 - CaO slags are found to be almost perfect; contact angles $\theta < 30^\circ$. Probably, this perfect wettability is one reason for the low content of total carbon in ferrosilicon refined by oxidative removal of Al and Ca.

In order to explain the behaviour of the SiC particles during sampling and casting, theories of pushing and engulfment of particles are discussed. Thermal criteria to characterize particle behaviour in front of a melt interface have been considered and the critical velocity for engulfment of silicon carbide particles in the liquid silicon has been calculated.

Based on work regarding light metals, a filter inclusion sampler was developed for liquid (ferro)silicon. Thus, the number size distribution for standard grade and refined FeSi75 from production runs was measured. The amount of particles found in the filter was low compared to that expected from the difference between carbon content in the melt and in the filtered metal. The reason is probably that a filter has a limited depth filtration capacity and is only able to capture a certain number of

particles of a given size distribution. Cake filtration starts when the depth filter capacity is exhausted. To preserve the cake in front of the filter can be difficult due to flow of metal back from the canister. However, even though the method underestimates the amount of SiC particles, the size distributions should be valid.

To obtain the low levels of total carbon in silicon and ferrosilicon required in various special markets, it is important to reduce the amount of silicon carbide particles in the molten alloy. Industrial scale removal of SiC particles by stirring in a ladle - pouring and inert gas purging - has been investigated, and total carbon in the melt was reduced to about 200 ppm. Analyses of the transition area between refractory and metal deposits showed that silicon carbide particles had been transferred to the wall and captured in a layer similar to what was found in the oxidic scoop. X-ray mapping indicates that this viscous oxidic layer has been saturated with silicon carbide particles. Thus it seems that the removal of carbon as SiC is limited by the capacity of a semi-molten layer to capture particles.

Reduction of the carbon content below the solubility level could be obtained by decarburization of the molten alloy by gas purging. A mathematical model describing the carbon removal from liquid silicon and ferrosilicon has been developed. The model shows that decarburization of silicon at atmospheric pressure is a slow process. The formation of a dense silica layer on the bubble surface may explain this low rate of carbon removal. The possibility to attain higher decarburization rates by employing vacuum and addition of silica particles has been considered.

The carbon content fell from roughly 200 to 100 ppm in gas-purged FeSi75 during teeming, casting and solidification. Partly silicon carbide particles can be transferred to oxides in the top layer and to the mould walls due to the stirring effect of teeming. Also, this reduction can be due to segregation of carbon to the molten zone during solidification. The remaining melt, enriched in Fe as the temperature falls, finally solidifies into an iron-silicon high temperature phase, ζ_α , and a secondary Si-phase. The abrasion resistance for ferrosilicon decreases with the amount of ζ_α - phase in the alloy. Thus, fines created during crushing and screening will be enriched in Fe and other alloying elements like carbon that accumulate in the molten zone during solidification. According to the theories on

pushing and engulfment, SiC particles are found to be rejected by the solidification front during chill casting and therefore will be found in the last liquid.

1. Introduction

Silicon and ferrosilicon produced by carbothermic reduction in submerged electric arc furnaces unavoidably contain impurities. The content of Al, Ca, Ti, Mn, Mg, Cu, Cr, Ni and V is generally in the 100 - 1000 ppm mass range or above. Inherently, due to the presence of dissolved C and SiC in the furnace, carbon in tapped metal will be saturated with carbon. Carbon solubility in silicon increases in an exponential manner with the temperature as shown in chapter 2.2 [1]. The metal temperature in the furnace hearth is not known, but it is estimated to be between 1800 and 2000 °C [2]. Data for carbon solubility in equilibrium with SiC is not available at these elevated temperatures, but extrapolating the solubility curve in figure 3, ch. 2.2 gives 1000 ppm C at 1950 °C. This is in reasonable accordance with the total carbon content of 700-1100 ppm found in samples drawn from the tapping stream from the furnace.

The carbon content in refined FeSi is about 100 ppm. Thus during refining and casting carbon is reduced by a factor of ten. In this work this removal is studied in detail. Hopefully, this knowledge will help us to attain the low levels of carbon required in various special markets.

Other impurities, such as S, B and P are usually encountered in the 10 - 100 ppm mass range or below [3-5]. In addition, oxides may be present as liquid or solid inclusions in the molten metal depending on the oxide composition and temperature, while carbides appear as solid inclusions [5-8].

The detrimental effect of these alloy contaminations depends on the use of the alloys and it is therefore reasonable to discuss silicon and ferrosilicon separately.

Silicon to the chemical industry and the photovoltaic industry

Silicon metal is mainly produced in two qualities, metallurgical grade silicon and chemical grade silicon. The main area of use for metallurgical grade silicon is the aluminium industry where the quality requirements generally are not as stringent as given by the chemical industry. However some manufacturers of foundry ingot for wheel alloy require silicon metal with less than 0.2 % Fe and 0.03% Ca [9]. For the chemical industry the quality requirements are generally strict but with large variations in the specifications from one producer to another [10]. The quality requirements are not only connected to chemistry, but also the structure of the silicon metal and its intermetallics is found to be of great importance in the Methyl Direct Process (the catalysed reaction of CH_3Cl and silicon). Inclusions in form of oxides and carbides are also disadvantageous to the Direct Process [7,11].

The purity of solar grade silicon (SOG-Si) required for solar cells is between 0.1-10 ppmw total impurities [4,12-18]. The maximum possible content of carbon in SOG-Si is 5×10^{17} atoms/cm³ (4.3 ppm mass) [17,18]. The market for solar grade silicon is today met by employing scrap from the expensive semiconductor grade silicon [15,16].

Polysilicon for semiconductor grade silicon (SEG-Si) is mainly produced by the Siemens process using trichlorosilane as starting material. According to H. Kohnno et al. [12], to maximise the production of trichlorosilane, the silicon metal employed should have;

- ▶ low content of elements that forms accretion in the fluidized bed, Ca and Fe are examples of such elements
- ▶ low content of inactive silica
- ▶ low content of elements interfering with sustained operation of the fluidized bed, for example aluminium will form AlCl_3 (g) in the reactor that solidifies and sticks to pipes and walls.
- ▶ low content of elements such as C and B that are difficult to remove by distillation.

Since boron and carbon must be strictly controlled in semiconductor devices, these

two elements are the target elements in the design of distillation columns in the production process for polysilicon [12]. Metallurgical grade silicon low in C and B could make the distillation tower in the Siemens process superfluous, which would reduce the production cost considerably [12].

The photovoltaic property¹ of silicon depends closely on the content of metallic impurities. Elements such as Au, Cu and Fe are so-called “lifetime killers” [13], and have to be kept on a very low level (ppb level). Carbon is classified as both a lifetime killer and a dopant. Other elements acting as dopants, such as P, B, O, Al, have also to be kept on a low level [13,14].

To serve the need for large-scale solar cell fabrication, low cost solar grade silicon production is required. One problem is to remove carbon from metallurgical grade silicon in an inexpensive and effective way. Several investigators have given valuable contributions to the effort to reduce the C content in silicon melts [15,17,18,20-24]. The methods employed have been filtration, decarburizing (with inert gas or under vacuum), plasma techniques, directional solidification etc., but the solutions have worked only on a laboratory scale. There is therefore still ample room for further investigations to develop methods giving cheap low carbon silicon.

Silicon and ferrosilicon to steel

Most of the world ferrosilicon production is consumed by the steel industry. Silicon, as ferrosilicon, is employed for deoxidation and as an alloying element in steelmaking. Silicon increases the elasticity and the tensile yield as well as the annealing resistance.

¹ Temperature or light is used to excite the valence electrons in pure semiconductors, such as silicon, out of their bonds, leaving them free to conduct current. Deficiencies, or “holes,” are left behind that contribute to the flow of electricity. Adding impurities to, or to “dope,” the semiconductor is another method to produce free carriers of electricity. The difference in the number of valence electrons between the doping material, or dopant (either donors or acceptors of electrons), and host gives rise to negative (n-type) or positive (p-type) carriers of electricity. P is an example of n-type donator, while Al is a p-type donator [19].

Addition of silicon in sufficient amounts eliminates the allotropic transformation of iron. Consequently, Si-Fe alloys can be annealed at high temperatures to promote grain growth [25]. This is utilized in the production of non grain oriented (NGO) steels, where grain size should be as large as possible to obtain low hysteresis loss [25]. For special compositions of silicon steels, rolling and heat treating techniques are employed to have the grains oriented. In these grain oriented (GO) steels the core loss has a minimum at a grain size between 2 and 10 mm [25].

NGO steels, containing between 0.5 and 3.5 mass% Si, are mainly employed in rotating applications. Grain oriented steels contains typically 3.15 mass% Si and have highly directional magnetic properties with lowest core loss and highest permeability when flux is parallel to the rolling direction. Grain oriented steel sheets are typically used in transformers.

The most critical elements in NGO are C, S and N. The reason is that C-, S- or N-precipitates can affect the movement of both grain boundaries and magnetic domains so that the grains do not grow as they should, i.e. become as large as possible. With the carbon content low; less than 0.003 mass%, high grade silicon electrical steels do not age significantly. Aging is the increase in core loss with time due to carbide precipitation [25]. When producing steel qualities such as NGO and GO steel, employing ferroalloys with low content of impurities like carbon is therefore necessary [26].

Stainless steel production is another steel sector where silicon is used to a great extent. This area is of special interest for two reasons.

- i. high specific consumption of ferrosilicon and other silicon rich alloys
- ii. high yearly growth rate in stainless steel consumption; 6-7 % compared with 0-1% for steel in general [27].

Figure 1.1 shows how stainless steel production has developed over the last 13 years as compared with steel in general.

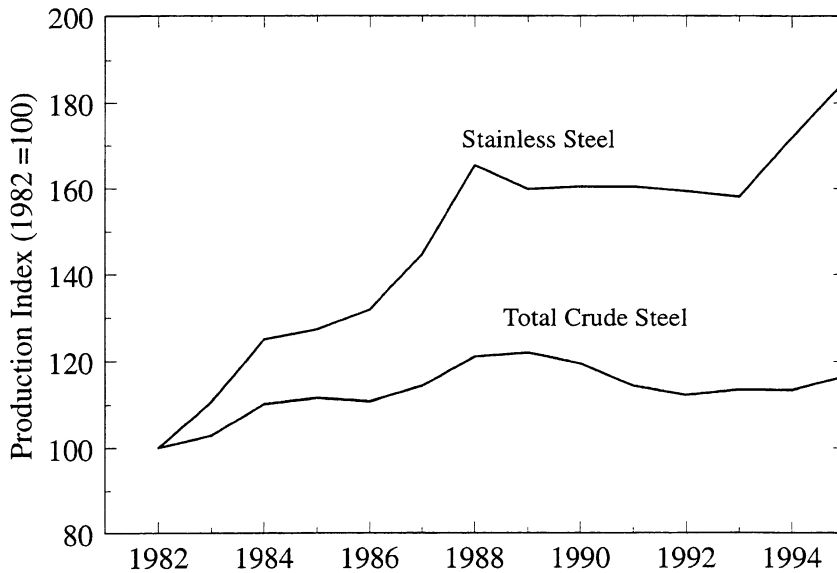


Figure 1.1: World Crude Steel Production from 1982-1995.

Sources: IISI, INCO and CRU International Ltd

The world stainless steel production reached 14.8 million metric ton in 1995, a doubling over the last 25 years. The consumption of stainless steel is expected to continue to grow in the future [27] due to the quality improvements and improvement in productivity. Another factor in favour of stainless steel over many other type of materials is the environmental aspect; favourable low Life Cycle Cost and 100% recyclable [27].

The most common route for stainless steel is to produce a high chromium steel in an Electric Arc Furnace. The carbon content in this high chromium melt is reduced by blowing oxygen in combination with an inert gas in an Argon Oxygen Decarburization (AOD) converter [28]. During this decarburization unavoidably some chromium is oxidized that has to be recovered. By adding silicon, in the form of ferrosilicon and other silicon rich alloys, the Cr-rich slag (30-40 mass% Cr_2O_3) is reduced and most of the valuable elements in the slag, such as chromium and manganese, are recovered. Typically around 15 kg Si/mt steel is added. Adding

such a high amount of alloy at this stage of the process, it is important to keep unwanted elements like carbon on a low level. The typical carbon specification for FeSi75 (FeSi75 = Ferrosilicon with 75 mass% Si) for slag reduction in AOD is today 0.04 mass% compared with 0.1 mass% for ferrosilicon to regular C-steel. Today many stainless steel producers require ferrosilicon with even lower carbon content, less than 200 ppm on a mass basis. Especially when producing stainless steel grades demanding high resistance against intergranular corrosion, such as the 304L, 316L and 317L grades ², the carbon content has to be low to avoid formation of detrimental chromium carbides [29].

Another example of steel with strict impurity requirements is silicon stainless steel containing 5 to 6 mass % Si. This steel has interesting corrosion resistance to concentrated H₂SO₄ due to formation of a tenacious silicon-rich film [29]. With a carbon specification of 0.02 %, the silicon additive must be low in carbon.

Steel as a construction material has been and still is challenged by new and lighter materials such as aluminium, magnesium, plastics and composite material. This challenge has over the latest years been met with development of new and improved steel grades, making it true that very often the best alternative to steel is even better quality of steel. Critical for the development of such new and improved steel grades is a low and controlled content of unwanted dissolved elements and inclusions. An example of dissolved elements greatly affecting the final steel quality is the amount of the elements S, P, O, N, C, H in deep drawing steels [30]. Another examples is production of ball bearing steels where the challenge is to lower a wide range of trace elements (Ca, C, H, Ti, O etc.). Figure 1.2 shows the development in the content of total oxygen in ball bearing steel at Ovako Hofors, Sweden [31]

² These are grades in the American Iron Steel Institute (AISI) 3-digit numbering system, where the 200 and 300 series are generally austenitic stainless steel, whereas the 400 series are either ferritic or martensitic. Some of the grades have a one- or two-letter suffix indicating a particular modification of the composition; for example the grade 304L is a 304-steel with low C-content, less than 0.03% C compared to 0.085% C in the 304-grade [29].

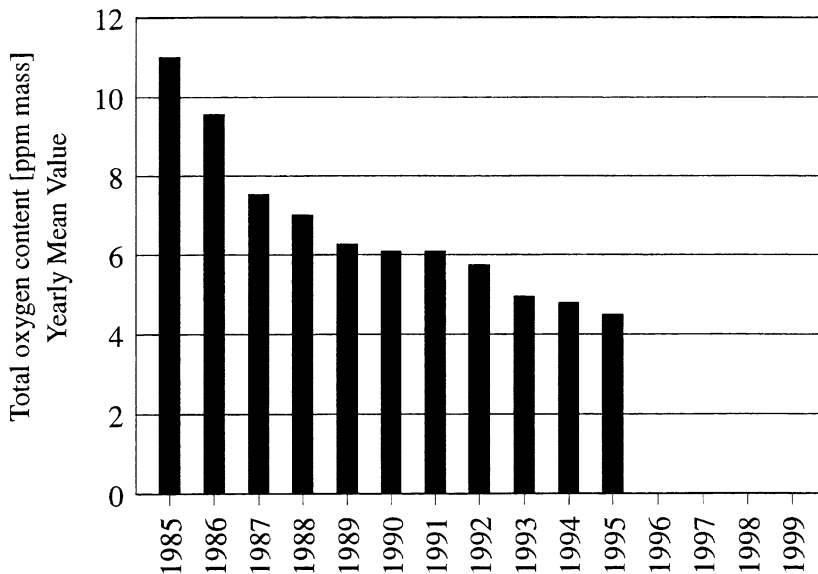


Figure 1.2: Development of total oxygen in ball bearing steel at Ovako Hofors [31]

With these stricter requirements on “clean steel”, impurities from alloy additions become more and more unacceptable. Dissolved elements and nonmetallic inclusions in the ferroalloy can increase the total level of unwanted elements.

1.1 Liquid metal refining of silicon and ferrosilicon

Liquid metal refining of silicon and ferrosilicon is mainly carried out for removal of Al and Ca, and the most common method is based on oxidation and removal of these impurities to a top slag. The development of the Tinject plug [32] in the early 1980's revolutionized the refining of (ferro)silicon, and today bottom gas injection is the most common practice employed in the industry. In addition to the removal of aluminium, which is the main purpose of the refining processes employed, we experience that some carbon is eliminated from the alloy. Customer requirements for low C ferrosilicon are therefore often met by offering low Al or High Purity FeSi.

1.2 Carbon in some commercial types of FeSi75

As mentioned above, secondary treatment, such as refining and method of casting, can influence the level of carbon in ferrosilicon. This is illustrated by an investigation of ferrosilicon with 75 mass% Si (FeSi75) shipped from Elkem Thamshavn presented in the following.

Elkem Thamshavn produces ~65,000 mt per year of ferrosilicon (basis 75 mass% Si) from two submerged electric arc furnaces. The metal is tapped in ladles and either cast directly or refined before cast. Silicon and ferrosilicon are today cast in principal two different ways, which is chill casting and water-granulation. The most common method world wide is chill casting. The liquid alloy is poured into moulds made of cast-iron or (ferro)silicon fines. The alloy is cast in one or several layers and cooled by natural convection. After solidified and cooled, the alloy is crushed and screened to give a suitable size distribution before shipping. This casting method is also most commonly employed for refined ferrosilicon. Another and more modern casting method today are water-granulation of silicon rich alloys, a casting method giving a size distribution of the alloy making that no crushing is needed.

Figure 1.3 shows in principle the different production routes from the furnace through refining and casting to shipment. The screened alloy, chill cast or granulated, is sampled and analysed according to standard procedure before shipping. These samples are prepared for chemical analysis, including carbon analysis. The way of preparing the samples for analyses and the method of analyses employed is described in chapter 3.2.

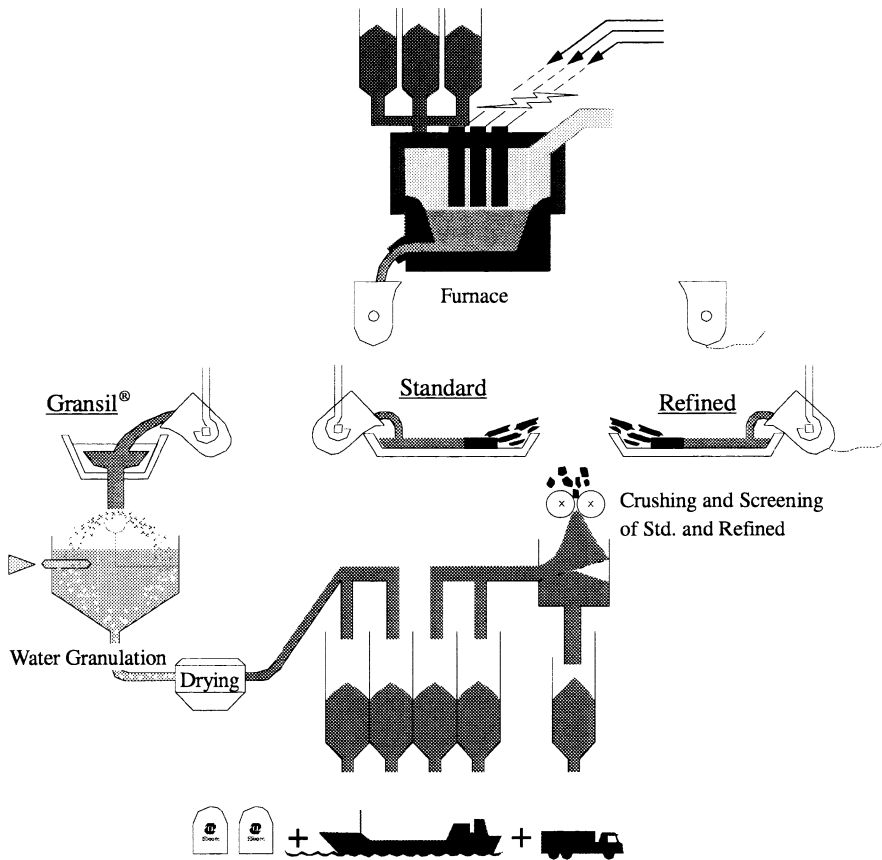


Figure 1.3: Production flow chart for the different qualities; granulated, refined and standard ferrosilicon [33].

The products from Elkem Thamshavn included in the following examination can be split into three main groups

- i. Gransil®; the trade mark of water granulated ferrosilicon from Elkem. Gransil is screened into mainly two sizes, 1-10 and 7-25 mm.
- ii. Standard FeSi75; ferrosilicon with 75 mass% Si tapped into ladle and cast directly into cast iron moulds. Standard ferrosilicon is crushed and screened into several different sizes.

- iii. Refined FeSi75; ferrosilicon with 75 mass% Si refined by bottom blowing and slag treatment to remove aluminium and calcium. The main quality is max. 0.10% Al, but several other qualities are produced. Refined FeSi75 is cast into iron moulds and crushed and screened in the same way as standard ferrosilicon.

The statistical treatment presented here includes all shipments of these three groups of alloys that were analysed for carbon with two exceptions; deliveries of low carbon FeSi75 and deliveries of fines. Low carbon means here deliveries of Gransil or standard crushed FeSi75 with carbon content less than 0.02 mass%. These deliveries are excluded since we are here comparing processing basically not aiming at lowering the carbon content.

Crushing of ferrosilicon creates fines, which is screened out as a 0-3 mm fraction. A larger part of the fines stem from the iron rich rest-melt where also contaminations such as Al, Ca and Ti are upconcentrated [34]. Whether C segregates in the same way in ferrosilicon is not quite clear. Part of this fines are used internally but someone is shipped. These shipment are excluded in the following examination.

The period examined was 1. January 1994 to 1. October 1996. For each year 1994, 1995 and 3 first quarter of 1996 the deliveries are split in the three product groups Gransil, refined and standard FeSi.

For each group the mean value of carbon content, the standard deviation and the standard error of the mean were calculated. The standard deviation, SD_x , for the carbon content in the samples is given as

$$SD_x = \sqrt{\frac{n \sum_{i=1}^n (x_i)^2 - (\sum_{i=1}^n x_i)^2}{n(n-1)}} \quad (1.1)$$

where x_i is the C content in sample i and n the number of samples. The standard

error of mean is given as

$$\bar{s}_x = \frac{SD_x}{\sqrt{n}} \quad (1.2)$$

A total number of 779 shipments are included in the statistical treatment and should give a good picture of how the carbon content in the alloys varies.

Figure 1.4 - 1.6 shows a plot of the carbon analysis of all shipment for the years 1994, 1995 and the three first quarters of 1996 respectively. The carbon analyses for the shipments, marked with *, shows a wide scatter for all three groups, but there are obvious differences. The mean value is consistently lowest for refined ferrosilicon for all the three years examined. Granulated FeSi75 has a lower average carbon content compared with standard lumpy ferrosilicon, but somewhat higher than the refined quality. The standard deviation and standard error of the mean, see frames inside the figures, shows that there seems to be a significant difference in carbon content in the samples from these three products.

The results from this investigation are summarized in table 1.1 where the mean value, standard deviation, standard error of mean and coefficient of variation, $V = SD_x/\bar{x}$, is given for all the samples from 1. January 1994 to 30. September 1996. The table shows that Standard FeSi75 content has approximate 300 ppm C on mass basis on average, whereas the carbon content is found to be 210 ppm on average in Gransil. In refined FeSi75 the carbon content is on average just below 120 ppm C.

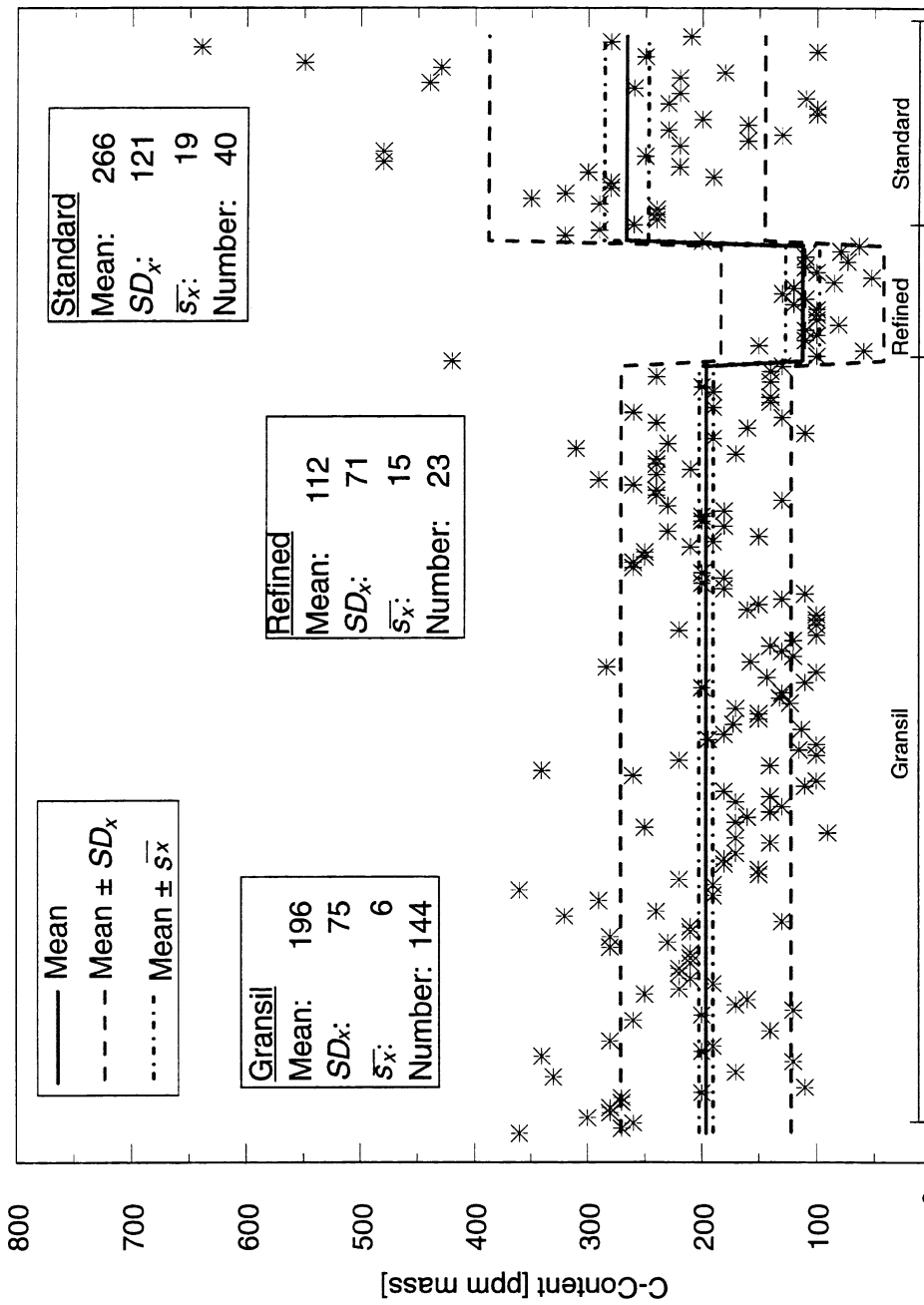


Figure 1.4: C-content in FeSi75-shipment from Elkem Thamshavn in 1994. Actual C-analysis is marked with *

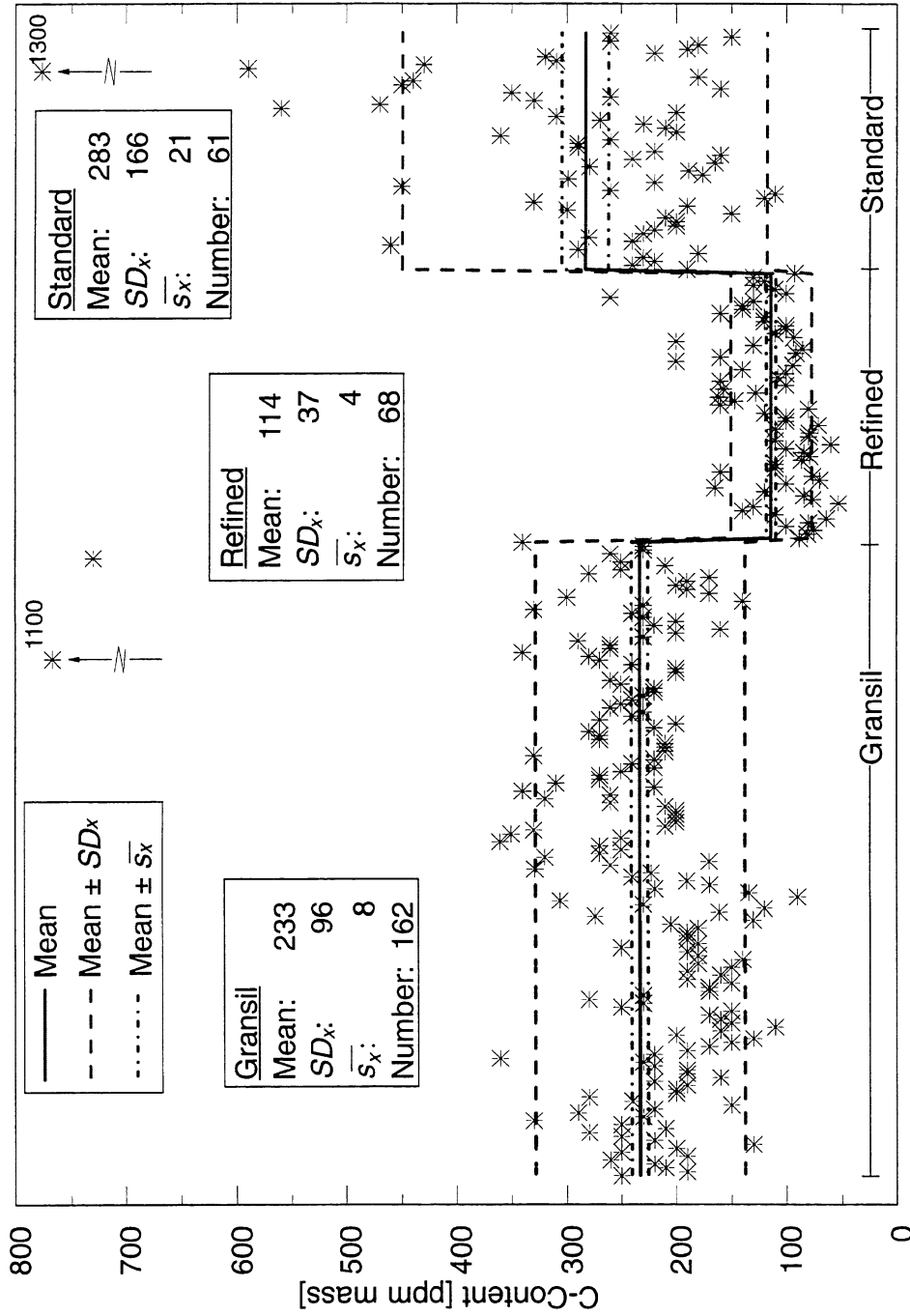


Figure 1.5: C-content in FeSi75-shipment from Elkem Thamshavn in 1995. Actual C-analysis is marked with *

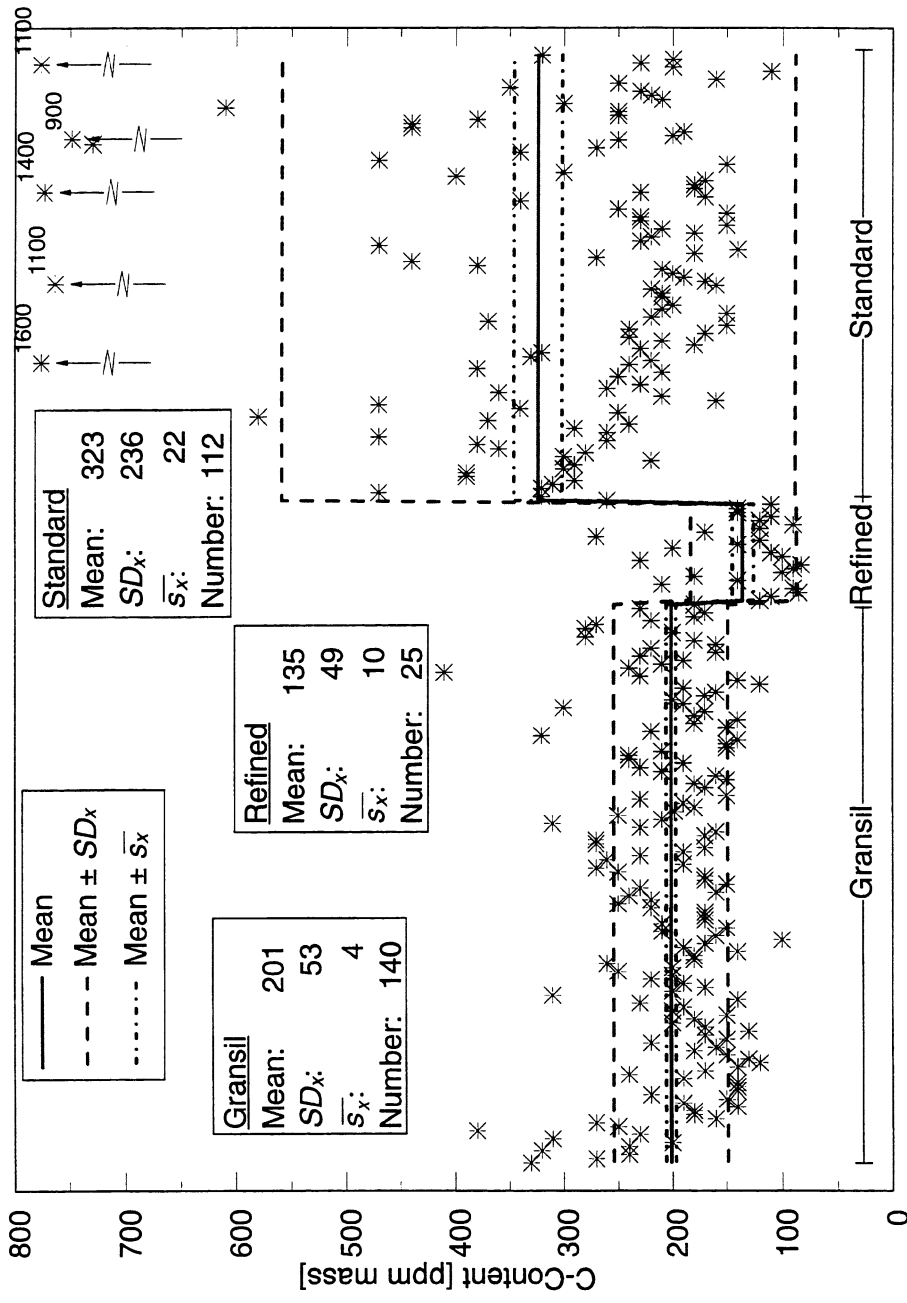


Figure 1.6: C-content in FeSi75-shipment from Elkem Thamshavn in Q1-Q3 1996. Actual C-analysis is marked with *

TABLE 1.1: Mean value of Carbon content in samples of water-granulated FeSi75 (Gransil), Refined FeSi75 and Standard FeSi75 from Elkem Thamshavn in the in the period 1.1.1994 - 30.09.1996.

	Gransil®	Refined FeSi75	Standard FeSi75
Mean C-content [ppm mass]	211	118	301
SD_x [ppm mass]	78.9	48.2	200.5
\bar{s}_x [ppm mass]	3.7	4.5	13.72
SD_x/\bar{x}	0.37	0.40	0.67
Number of samples	446	120	213

To verify if this difference in C content is by chance or a result of the different production routes, a 'Student' *t*-test has been performed, see appendix A. In these tests the refined quality is compared with Gransil and Gransil is compared with the standard grade ferrosilicon. The tests show high observed $|t|$ -values and the conclusion is that Refined FeSi75 gives a lower content of carbon than Gransil, and that Gransil is lower in C than Standard FeSi75, cf. Appendix A.

These results and the fact that there is an increasing need for silicon and silicon rich alloys with reduced content of impurities such as carbon has been the driving force to investigate how carbon exists in ferrosilicon and the mechanism for removal of carbon from (ferro)silicon.

References

1. Bakke, P. and Klevan, O. S., "Thermodynamics of Liquid Silicon Bases Alloys," *Process Technology Conference Proceedings*, Vol. 14, ISS (1995), pp. 155-165
2. Schei, A., "Ferrosiliumprosessen metallurgi", *Report for A/S FESIL & Co, Elkem-Spigerverket a/s R&D Center, Norway, (1976-1977)* (in Norwegian)
3. Tuset, J.K., "Principles of silicon refining", *International seminar on refining and alloying of liquid aluminium and ferro-alloys*, August 26 - 28, (1985) pp. 50 - 69
4. Schei, A., "High purity silicon production", *International seminar on refining and alloying of liquid aluminium and ferro-alloys*, August 26 - 28, (1985) pp. 71 - 89
5. Balbi, M., Tosi, G., Zoja, R. and Borile, F., "Sulle inclusioni non metalliche nel ferro silico", *La Fonderia Italiana*, No.10, (1976) pp. 45 - 49 (in Italian)
6. Klevan, O. S. and Engh, T. A., "Dissolved Impurities and Inclusions in FeSi and Si, Development of a Filter Sampler", *INFACON 7, Proceedings of the 7th International Ferroalloys Congress*, FFF, Trondheim (1995), pp. 441 - 451.
7. Forwald, A.G., Rong, H.M. and Vogelaar, G., "Oxygen in silicon; occurrence and influence on the direct process to methylchlorosilanes", *Silicon for the Chemical Industry II, Loen, Norway, 8 - 10. June*, Editors, Øye et al., Tapir Forlag, Trondheim, Norway, pp. 107 - 119
8. Balbi, M. and Caironi, G., "Non-metallic inclusions in ferro-alloys used in stainless steel manufacture", *Avesta Stainless Bulletin*, No.4 (1982) pp. 14 -19
9. de Linde, J. P., "The outlook for silicon metal", *Silicon for the Chemical Industry II, Loen, Norway, 8 - 10. June 1994*, Editors, Øye et al., Tapir Forlag, Trondheim, Norway, (1994) pp. 257 - 269
10. Halm, R., "Silicon for Methylchlorosilane Manufacture", *Silicon for the Chemical Industry II, Loen, Norway, 8 - 10. June 1994*, Editors, Øye et al., Tapir Forlag, Trondheim, Norway, (1994) pp. 159 -164
11. Margaria, T., "Identification and Control of the Characteristics of Silicon Used in the Direct Synthesis", *Silicon for the Chemical Industry II, Loen,*

-
- Norway, 8 - 10. June 1994, Editors, Øye et al., Tapir Forlag, Trondheim, Norway, (1994) pp.69 - 80
12. Kohno, H., Kuroka, T. and Itoh, H., "Quality requirements for silicon metal in polysilicon production", *Silicon for the Chemical Industry II, Loen, Norway, 8 - 10. June 1994, Editors, Øye et al., Tapir Forlag, Trondheim, Norway, (1994) pp. 165 - 170*
 13. Fahrenbruch, A. L. and Bube, R. H., *Fundamentals of solar cells*. Academic Press (1983), chapter 7
 14. Amouroux, J. and Morvan, D., "Heat and mass transfer phenomena during plasma/slag interaction. Applications on the production of ultrapur material", *High Temp. Chem- Processes* **1** (1992) pp. 537-560
 15. Ikeda, T and Maeda, M., "Purification of Metallurgical Silicon for Solar-grade Silicon by Electron Beam Button Melting", *ISIJ International* **32** (1992) pp. 635-642
 16. Suzuki, K., Kumagai, T. and Sano, N., "Removal of Boron from Metallurgical-grade Silicon by Applying the Plasma Treatment", *ISIJ International* **32** (1992) pp. 630-634
 17. Sakaguchi, Y., Yuge, N., Babe, H., Nishikawa, H., Terasshima, H. and Aratani, F., "Metallurgical Purification of Metallic Grade Silicon up to Solar Grade", *12th European Photovoltaic Solar Energy Conference*, 11-15 April 1994, Amsterdam, The Netherlands, pp. 971-974
 18. Babe, H., Hanazawa, K., Yuge, N., Sakaguchi, Y., Terasshima, H. and Aratani, F., "Metallurgical Purification for Production of Solar Grade Silicon from Metallic Grade Silicon", *13th European Photovoltaic Solar Energy Conference*, 23-27 October 1995, Nice, France, pp. 390-394
 19. Funk & Wagnall's 29-volume Encyclopedia, Infopedia, Future Vision Multimedia Inc., Spring Valley NY, USA (1994)
 20. Sakaguchi, K and Maeda, M., "Decarburization of Silicon Melt for Solar Cells by Filtration and Oxidation", *Metallurgical Transactions B* **23B** (1992) pp. 423-427
 21. Mühlbauer, V., Diers, A. and Walther, A., "Removal of C/SiC from Liquid Silicon by Directional Solidification", *Journal of Crystal Growth* **108** (1992) pp. 41-52
 22. Thomas, R. E., Mantini, M. J., Rudder, R. A., Malta, D. P., Hattangady, S. V. and Markunas R.J. "Carbon and Oxygen Removal from Silicon (100)

- Surfaces by Remote Plasma Cleaning Techniques”, *Journal of Vacuum Science Technology A* **10** (4) (1992) pp. 817-822
23. Bakke, P., “Carbon Removal from Molten Silicon by Gas Purging”, *Internal Memo Elkem* (1993)
 24. Tsutsumitake, H. and Haida, O., “Process for producing high purity Si”, *Japanese Patent No. 62-292613*, (1987)
 25. Metals Handbook 9th Ed. Volume 3, ASM (1980) pp. 597-614
 26. Jacobi, H. and Rakoski, F., “Hohe Reinheit der Stähle als Kriterium der Werkstoffentwicklung”, *Stahl und Eisen* **116** (5) (1996) pp. 59-68
 27. Stawowy, H., “Die Erzeugung nichtrostender Stähle, gegenwärtiger Stand und Entwicklung in Technologie und Wirtschaftlichkeit”, *Stahl und Eisen* **116** (9) (1996) pp. 37-41
 28. Engh, T.A., *Principles of metal refining*. Oxford University Press (1992), pp. 280-301
 29. Davis, J.R. *ASM Specialty Handbook - Stainless Steel*, ASM International (1994) pp. 3-30, 153
 30. Haastert, H.P., “Entwicklungsrichtungen der Sekundärmetallurgie, im besonderen das RH-Verfahren zur Vakuumbehandlung”, *Stahl und Eisen* **111** (3) (1991), pp. 103-109
 31. Lund, T., “Rent stål stärker lagret”, *Evolution, Affärs- och teknikmagasin från SKF nr1/1996* (in Swedish)
 32. Skei, B., “Refining of silicon alloys by the Tinject Process”, *48th Electric Furnace Conference Proceedings*, (1990)
 33. Information Pamphlet from Elkem Thamshavn
 34. Tveit, H., “Størkning av 75 % Ferrosilisium, Forløp, Struktur og Styrke”, *Dr.ing. avh. 1988:53, Metallurg. Inst. NTH, Trondheim* (1988).

2. Thermodynamic and Physical Data

2.1 Introduction

In order to understand the limitations of the refining processes of silicon and silicon alloys, access to reliable thermodynamic data of silicon-based alloys is mandatory. For alloys based on iron, copper, nickel, cobalt and aluminium extensive lists of activity data and interaction coefficients are tabulated in textbooks. In the case of silicon, such tables have - as far as we know - yet to be worked out.

To be able to model metallurgical processes such as refining and casting, it is also necessary to have access to physical property data for the metals and alloys of interest. The most important properties are density, heat capacity, surface and interfacial tension, viscosity and thermal conductivity.

In this chapter both thermodynamic data and some physical data for (ferro)silicon is collected and presented. Also, some physical data for SiC is included. The thermodynamics of liquid silicon is a reprint of a paper from the 14th Process Technology Conference Proceedings.

2.2 Thermodynamics of liquid silicon-based alloys

As stated above thermodynamic data of liquid silicon and silicon alloys was presented at the 14th Process Technology Conference in Orlando, Fl, November 12-15, 1995 where the subject was Ladle Processing: Metallurgy and Operations. This section is a reprint of the paper, and references for this part are included in the reprint and not repeated at the end of chapter 2.

THERMODYNAMICS OF LIQUID SILICON BASED
ALLOYS

Per Bakke¹ and Ole-Svein Klevan²

¹) Elkem a/s. Research, PO Box 40, Vaagsbygd, N-4602
Kristiansand S, Norway. Present address: Norsk Hydro a.s.,
Research Centre, N-3901 Porsgrunn, Norway

²) Elkem Thamshavn, PO Box 10, N-7301 Orkanger,
Norway

ABSTRACT

The thermodynamics of liquid silicon based alloys, solubilities, activity coefficients and interaction coefficients in the Wagnerian representation, have been collected and tabulated extensively. The collected data reveal some discrepancies in the solubility data for carbon, hydrogen, oxygen and nitrogen. The available thermodynamic data have been used to calculate the solubility of oxygen and carbon in some commercial silicon based alloys. The relatively large effects of low aluminium contents on carbon and oxygen solubility in the alloys are illustrated. The solubilities of oxygen and carbon may determine the lowest limits for the oxygen and carbon contents that can be achieved by ladle metallurgy operations.

1. INTRODUCTION

Silicon alloys produced in electric furnaces unavoidably contain C, Fe, Al, Ca, Ti, Mn, Mg, Cu, Cr, Ni and V in the 100 - 1000 ppm by mass (ppmw) range or above. Other metallic impurities, S, B and P are usually encountered in the 10 - 100 ppmw range or below [1-3]. In addition, oxides may be present as liquid or solid inclusions in the molten metal depending on the oxide composition and temperature, while carbides appear as solid inclusions [3-6].

Customers requirements with respect to chemical composition as well as oxide and carbide content are steadily becoming more strict, enforcing greater focus towards control and removal of inclusions and some dissolved elements. Ladle refining of metallurgical silicon for removal of Al, Ca and Mg [7-10] as well as addition of other elements [11] may be necessary to meet specific demands for the chemical market. In the production of silicon based alloys for the foundry market, the alloying of high cost elements is perhaps the most important part of the production process. Silicon for photovoltaic applications requires impurity levels in the sub-ppm range for nearly all elements. Molten metal refining of metallurgical silicon to photovoltaic quality has thus proven to be difficult, although

several technologies have been tested [12-16].

In order to understand the limitations of the refining processes of silicon and silicon alloys, access to reliable thermodynamic data of silicon based alloys is mandatory. For alloys based on iron, copper, nickel, cobalt and aluminium extensive lists of activity data and interaction coefficients are tabulated in textbooks [17-20]. In the case of silicon, such tables have -as far as we know- yet to be worked out.

In this paper the aim has been to collect and present available thermodynamic data relevant to silicon based alloys. Practical use of thermodynamic data is illustrated by discussing oxygen and carbon solubilities in some commercial silicon based alloys.

2 BASIC FORMULAE

The interaction coefficients in dilute solutions were defined by Wagner from a Taylor series expansion of the logarithm of the activity coefficient [21-24]

$$\ln \gamma_i = \ln \gamma_i^0 + \sum_{j=2}^{N_j} \epsilon_i^j x_j + \sum_{j=2}^{N_j} \sum_{k=2}^{N_j} \rho_i^{j,k} x_j x_k + O(x^3) \quad (1)$$

The ϵ_i^j 's and $\rho_i^{j,k}$'s are first and second order interaction coefficients, respectively, referring to the pure solvent as the standard state. The sums are taken over all alloy components except the solvent metal (component 1). γ_i^0 is the Raoultian activity coefficient if there had been no interaction between the solute components, and it therefore corresponds to Henry's law [19]. $N_j - 1$ is the number of alloy elements, thus the number of components in the system is N_j . For convenience $\rho_i^{j,j} \equiv \rho_i^j$. For the second order cross interaction coefficients the symmetry $\rho_i^{j,k} = \rho_i^{k,j}$ applies.

In metallurgy, the reference state is very often chosen as the hypothetical concentration 1% by mass, [%X_i] = 1 rather than the pure solvent $x_1 = 1$. In this representation the 10-based logarithm is used, and the Taylor series expansion of the activity coefficient becomes

$$\log_{10} f_i = \sum_{j=2}^{N_j} e_i^j [\%j] + \sum_{j=2}^{N_j} \sum_{k=2}^{N_j} r_i^{j,k} [\%j][\%k] + O([\%]^3) \quad (2)$$

The e_i^j 's and $r_i^{j,k}$'s are first and second order interaction coefficients, respectively, referring to the 1 mass % as the standard state. (Still $r_i^{j,j} \equiv r_i^j$ and $r_i^{j,k} = r_i^{k,j}$). Note that in eqn. (2) the zeroth order term in eqn. (1) has vanished. The free energy of dissolution defined for reference state [%X_i] = 1 is

$$\Delta G_i^0 = RT \ln \left(\gamma_i^0 \frac{m_i}{100 m_i} \right) \quad (3)$$

The m_i 's are molar weights (kg/kmol), and R is the gas constant (8.314 kJ/K kmol).

Changing the first order interaction coefficients between the two reference states e_i^j and ε_i^j yields [23]

$$e_i^j = e_i^j \left(\frac{m_j 100 \ln 10}{m_i} \right) + \left(1 - \frac{m_j}{m_i} \right) \quad (4 a)$$

and

$$e_i^j = e_i^j \frac{m_j}{m_i} + \frac{1}{100 \ln 10} \left(1 - \frac{m_j}{m_i} \right) = e_i^j \frac{m_j}{m_i} \quad (4 b)$$

Shifting the second order interaction coefficients from one reference state to the other is slightly more complicated, involving first order interaction coefficients as well [23].

Some relationships that may be useful for metallurgists are [23]

$$e_i^j = e_i^j \quad (5 a)$$

$$\rho_i^{j,j} + \varepsilon_i^j = 2 \rho_i^j + \varepsilon_i^j \quad (5 b)$$

and

$$\rho_i^{j,k} + \varepsilon_j^k = \rho_j^{i,k} + \varepsilon_i^k = \rho_k^{i,j} + \varepsilon_i^j \quad (5 c)$$

Notice that since generally $e_i^j \neq e_j^i$, eqns. (5 a - c) are *not* valid for the e_i^j 's and the $\rho_i^{j,k}$'s.

It has been shown [25-26] that in terms of interaction coefficients for the solutes the activity coefficient for the solvent (component 1) can be written

$$\ln \gamma_1 = -\frac{1}{2} \sum_{j=2}^{N_1} \sum_{k=2}^{N_1} \varepsilon_j^k x_j x_k \quad (6 a)$$

and for the solutes

$$\ln \gamma_i = \ln \gamma_i^0 + \ln \gamma_i + \sum_{j=2}^{N_1} \varepsilon_i^j x_j \quad (6 b)$$

Equations (6 a) and (6 b) which are called "The Unified Interaction Parameter Formalism" are valid at all compositions, thus making the use of interaction coefficients interesting not only for dilute alloys.

3 TABLES

Solubilities of various elements in liquid silicon are listed in Table I. We have chosen to present the solubility data in the form

$$[\%X_i] = [\%X_i]_{T_m} \exp \left(E \left(\frac{1}{T} - \frac{1}{T_m} \right) \right) \quad (7)$$

where $[\%X_i]_{T_m}$ is the solubility (ppmw) at the melting point of pure Si ($T_m = 1685$ K [27]) and E is an energy term (K). $[\%X_i]_{T_m}$, and E are tabulated. Solubility data presented in this form are more easy to compare than in the usual form

$$\log_{10} [\%X_i] = \frac{a}{T} + b$$

Dissolution energies and activity coefficients are listed in Table II. The *first order* interaction coefficients are listed in Table III (self interaction coefficients) and Table IV first order interaction coefficients. The *second order* interaction coefficients are listed in Table V (self interaction coefficients) and Table VI (interaction coefficients ρ_i^j and cross interaction coefficients $\rho_i^{j,k}$). Notice that more interaction coefficients may be generated by using the formulas given in eqns. (4) and (5).

Italicised number in the tables are values identical to those appearing in the referenced papers. Numbers in ordinary types are mainly calculated from original experimental data employing eqns. (4) and (5). Ordinary typed numbers enclosed in parentheses indicate values recalculated from tabulated activity data, graphs or other representations and should be considered as estimates or speculative values. If

Table I Solubility as a function of temperature of various elements in liquid silicon.

Element	Precipitated phase	Solubility at T_m ¹ [$\%X_i$] _{T_m} (ppmw)	Solubility ¹ , temperature dependence (K)	References
C	SiC (s)	55	-22417	28, 29, 30, 31, 32, 33, 34, 46, 47, 48, 49, 50
H	1/2 H ₂ (g)	7.5	-12300	51, 52, 53, 54, 55
N	1/4 Si ₃ N ₄	4	-22471	29, 57, 58, [59, 60, 61] ²
O	1/2 SiO ₂	24	-16060	28, 29, 35, 36, 37, 38, 39, 40, 57, 62, 63, 64, 65

¹ Solubility presented as in eqn. (7). ² Solubility determined towards 1/2 N₂ (g)

Table II The solution thermodynamics for elements *i* in liquid Si. Italicised figures are experimentally determined values. Estimates are enclosed in parentheses.

Element	$\ln \gamma_i^0$	ΔG_i^0 ((%X _i)) (J/mole)	Temp. range (°C)	References
Ag (l)	(1.7)	(-52000)	1200	20
Al (l)	<i>6.06 - 14048/T</i>	<i>-116795 + 12.4 T</i>	1420 - 1650	28, 20, 66, 67, 68, 69
B (s)	13.40 - 25560/T	-212510 + 81.1 T	1450 - 1650	59, 70, 71
C (s)	<i>0.086 + 7672/T</i>	<i>63785 - 30.5 T</i>	1420 - 1650	28, 29, 30, 31, 32, 33, 48, 49
Ca (l)	<i>5.45 - 23006/T</i>	<i>-191272 + 4.07 T</i>	1420 - 1650	28, 72, 73
Ce (l)	(-11.5)	(-280000)	1647	74
Co (l)	3.21 - 14595/T	-121340 - 17.8 T	1470 - 1610	75, 20, 76, 77
Cr (l)	-4.6	(-175000)	1610	79, 69, 77, 80
Cu (l)	-0.27 - 1320/T	-11000 - 47.3 T	1500	79, 20, 76, 77
Fe (l)	3.87 - 12934/T	-107530 - 11.8 T	1470 - 1610	75, 17, 20, 41, 75, 77, 78, 79, 81, 82, 83, 84, 85
1/2 H ₂ (g)	1.166 + 12277/T	102080 - 0.86 T	1550 - 1650	51, 52, 54, 56
Mg (l)	(-4.2)	(-97000)	1077	86, 87, 88
Mn (l)	1.68 - 9380/T	-78000 - 29.9 T	1427	79, 69, 76, 77, 89, 90, 91, 92, 93, 94, 95, 96, 97, 98
Mo (l)	(-2.5)	(-130000)	1597	99
1/2 N ₂	-5.64 + 24900/T	207000 - 79.4 T	1450 - 1650	59, 29
Nb (l)	(-8)	(-210000)	1640	99
Ni (l)	2.6 - 14800/T	-123000 - 22.8 T	1510	79, 20, 76, 77
1/2 O ₂	12.49 - 40933/T	-340316 + 70.3 T	1420 - 1650	28, 29, 35, 36, 36, 38, 39, 62
Sc (l)	(-7)	(-175000)	1500	77, 80
Ti (l)	(-10)	(-225000)	1500	77, 80, 100, 101
V (l)	(-6)	(-180000)	1640	99, 77, 80, 101
Y (l)	(-9.4)	(-235000)	1597	102
Zr (l)	(-12)	(-265000)	1500	100

the reader wishes to use these data in his calculations he is recommended to consult the references. Second order coefficients in general are uncertain and should be used with great care. The number appearing at first position in the reference column is that from which the actual tabulated data are derived.

4 CALCULATION OF OXYGEN AND CARBON SOLUBILITIES IN COMMERCIAL ALLOYS OF THE Si-Fe-AL SYSTEM

From standard Gibbs energy data and the Gibbs energies of solution given in Table II together with the interaction coefficients given in Table III - V we can calculate the solubility of for instance oxygen and carbon in liquid silicon with varying amounts of alloying elements. Here we will give some examples on the influence of iron on the solubility of oxygen and carbon in liquid silicon. Two levels of iron are investigated, 25 and 35 % by mass, that is equivalent to the iron level in the commercial alloys FeSi75 and FeSi65. We regard these alloys as "low alloy" melts of silicon

alloyed with iron. Then we look at the solubility of carbon and oxygen in liquid (ferro)silicon at 1600°C when the aluminium contents vary from zero to one mass %. There are some discrepancies in the published solubility data for C [28-34] and O [28,29,35-40]. However, only Ottem [28] has presented interaction coefficients for C and O with Al and Fe, and for that reason, we have chosen to use his solubility data.

4.1 Oxygen

The solubility of oxygen in liquid silicon and ferrosilicon is in the literature based on the equilibrium between SiO₂ (s) and Si (l) [28,29,35-40]. The solubility can be described by the equation

$$\log_{10}[\%O] = -\frac{6975}{T} + 1.52 - \frac{1}{2} \log a_{Si} - \log f_O \quad (8)$$

when the activity of silica is unity. The activity coefficient for oxygen in liquid silicon is given by eqn. (2) and can be written as

Table III First order self interaction coefficients ϵ_i^i and e_i^i in binary silicon alloys. Italicised figures are experimentally determined values. Estimates are enclosed in parantheses.

<i>i</i>	ϵ_i^i	e_i^i	Temp. (°C)	References
Ag	(-4.7)	(-2.1·10 ⁻³)	1200	20
Al	-0.31 + 38/T	-1.58·10 ⁻³ + 0.17/T	~ 1427	66, 20, 67, 68, 69
Ca	(7)	(0.023)	1350	72
Cc	(4.9)	(7.8·10 ⁻³)	1647	74
Co	(0.50 + 1258/T)	(3.3·10 ⁻³ + 2.60/T)	1470 - 1610	75, 20, 76, 78
Cr	(-3.2)	(-0.014)	1600	69
Cu	(0.2)	(2.8·10 ⁻³)	1487	76, 20
Fe	-4.94 - 15276/T	-8.63·10 ⁻³ - 33.37/T	1500 - 1600	81, 17, 20, 75, 78, 82, 83, 84, 85
Mg	(18)	(0.09)	1077	86, 87
Mn	8.1	0.02	1400	89, 91, 92, 93, 94, 95
Ni	(8.67 + 1323/T)	(0.0203 + 2.750/T)	1600	76, 20
Y	(-0.9)	(1.7·10 ⁻³)	1597	102

Table IV First order interaction coefficients ϵ_i^j and e_i^j in ternary silicon alloys. Italicized figures are experimentally determined values. Estimates are shown in parentheses.

<i>i, j</i>	ϵ_i^j	e_i^j	Temp. (°C)	References
B, N	238	2.07	1450	59
C, Al	6.76 - 38610/T	0.0304 - 174.54/T	1420 - 1650	28
C, Ca	(0)	(0.0013)	1420 - 1650	28
C, Fe	6.56 - 6980/T	0.0165 - 15.24/T	1552 - 1677	28
Co, Fe	< 0	(< 2·10 ⁻³)	1550	78
H, Co	10.94 - 10928/T	0.0249 - 22.62/T	1550 - 1650	51, 54
H, Fe	3.5	(0.01)	1600	103, 51, 52, 56
H, Mn	1.4	0.0052	1445	55
Mn, Fe	(99)	(0.22)	1427	94
N, Fe	< 0	< 0.002	~ 1600	104 ¹
O, Al	75.7 - 329281/T	0.342 - 1488.6/T	1445 - 1570	28
O, As	1276 - 2365100/T	2.08 - 3850/T	1420 - 1550	105
O, B	-2.04	-0.03	1420 - 1550	105
O, C	(0)	(-0.006)	1420 - 1650	28
O, Ca	< 0 (small but noticeable)	(< 0.0013)	1420 - 1650	28
O, Fe	-25.0 + 32310/T	-0.0524 + 70.57/T	1420 - 1650	28
O, P	406 - 766680/T	1.60 - 3020/T	1420 - 1550	105
O, Sb	-23.3	-0.02	1420 - 1550	105

¹) Experimental data for FeSi alloys ([%Si] < 45) indicate significantly higher nitrogen solubilities than in pure Si. As a result, the interaction coefficient e_N^{Fe} should be negative.

Table V Estimated second order self interaction coefficients ρ_i^i and r_i^i in binary silicon based alloys.

i	ρ_i^i	r_i^i	Temp. (°C)	References
Al	(400/T)	(2.14·10 ⁻⁵ - 0.0192/T)	- 1427	66, 67, 68, 69
Ca	(-2.5)	(1.35·10 ⁻⁵)	1350	72
Cc	(25)	(9.2·10 ⁻⁵)	1647	74
Co	(-10.3 + 7550/T)	(-1.19·10 ⁻⁵ + 0.137/T)	1470 - 1610	75, 76, 78
Cr	(10)	(5.78·10 ⁻⁵)	1600	69
Cu	(1.4)	(2.07·10 ⁻⁵)	1487	76
Fe	0	(-4.58·10 ⁻⁵ - 0.17/T)	1500 - 1600	81, 75, 78, 82, 83, 84, 85
Mg	(-45)	(-2.75·10 ⁻³)	1077	86, 87
Mn	(-4)	(4.7·10 ⁻⁵)	1400	89, 91, 92, 93, 94
Ni	(-38.6 + 16840/T)	(-8.33·10 ⁻⁵ - 0.184/T)	1600	76
Y	(26)	(1.14·10 ⁻⁴)	1597	102

Table VI Second order interaction coefficients $\rho_i^{j,k}$ and $r_i^{j,k}$ in ternary and quaternary silicon based alloys. Italicized figures are experimentally determined values. Estimates are enclosed in parentheses

i, j, k	$\rho_i^{j,k}$	$r_i^{j,k}$	Temp. (°C)	References
C, Fe, Fe	<i>-51 + 101344/T</i>	<i>-4.84×10⁻⁴ + 1.0374/T</i>	1552 - 1677	28
Co, Fe, Fe	(19)	(2.1×10 ⁻⁴)	1550	78
Fe, Co, Co	(79)	(7.8×10 ⁻⁴)	1550	78
H, Co, Co	(0.527 - 11343/T)	(1.268 ×10 ⁻⁴ - 0.2303/T)	1550 - 1650	51, 54
H, Fe, Fe	(3.91 - 17872/T)	(8.6 ×10 ⁻⁵ - 0.196/T)	1550 - 1650	51, 52, 56
Mn, Fe, Fe	(-597)	(-5.48×10 ⁻³)	1427	94
O, Al, Al	<i>-4566</i>	-0.215	1570	28
O, Fe, Fe	<i>258 - 416000/T</i>	<i>2.57×10⁻³ - 4.218/T</i>	1553 - 1616	28
Co, Co, Fe	(11)	(2.5×10 ⁻⁴)	1550	78
Fe, Co, Fe	(-54)	(-4.2×10 ⁻⁴)	1550	78
H, Co, Fe	(-80)	(-7.2×10 ⁻⁴)	1600	78
Mn, Fe, Mn	(-74)	(5.3×10 ⁻⁴)	1427	94

$$\log_{10} f_o = e_o^{Al} [\%Al] + e_o^{Fe} [\%Fe] + r_o^{Al} ([\%Al])^2 + r_o^{Fe} ([\%Fe])^2 \quad (9)$$

Here e_o^O , and $r_o^{Al,Fe}$ are assumed to be zero. Higher order interaction coefficients are also taken to be zero. At 1873 K, the activity of silicon, a_{Si} , in eqn. (8) is 0.82 and 0.71 for silicon alloyed with 25 and 35 mass % iron, respectively [41]. Here we assume that the activity of silicon is independent of the temperature. In Figure 1 the solubilities of oxygen in liquid silicon and the two ferrosilicon alloys are shown as functions of the temperature. We see that the

ferrosilicon alloys dissolve approximately twice as much oxygen as pure silicon.

In Figure 2 the solubility of oxygen at 1550°C is plotted against the aluminium content in the FeSi75 alloy. As seen from this figure the aluminium content has a great effect on the oxygen solubility. The oxygen solubility increases with approximately 10 ppmw per 0.1% mass% Al in FeSi75 up to 0.15 mass% Al. Above this aluminium level the activity of silica is less than one hence the oxygen solubility curve will not be so steep. The figures may indicate that if we remove Al from (ferro)silicon melts we should simultaneously precipitate SiO₂.

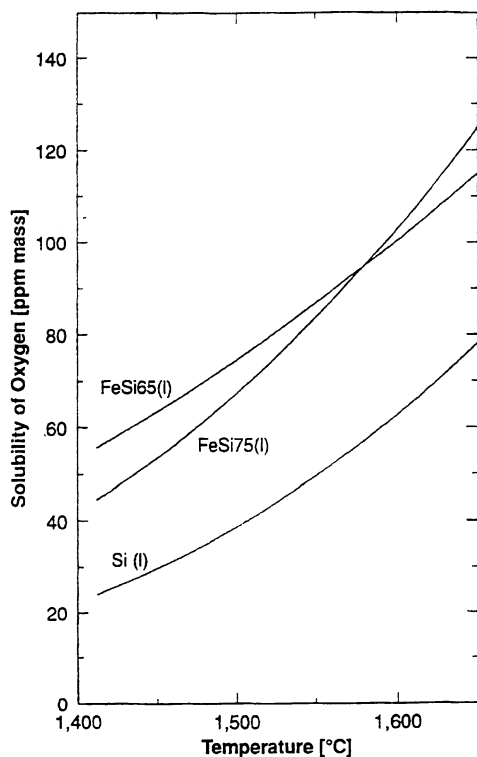


Figure 1. Solubility of oxygen in pure silicon, 75% FeSi and 65% FeSi based on thermodynamic data from Ottem [28]

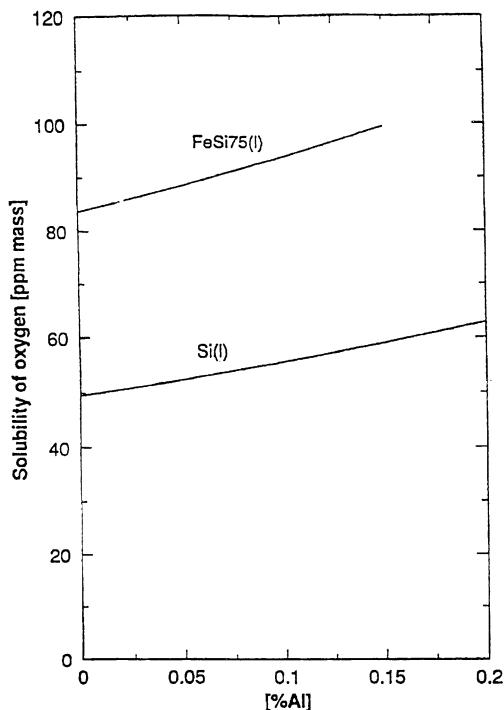


Figure 2. The effect of aluminium on the solubility of oxygen in pure silicon and 75% FeSi at 1550°C. The activity of silica is assumed to be one. (Based on thermodynamic data by Ottem [28])

Analyses of total oxygen content from samples of 75% FeSi indicate that oxygen levels generally are higher than the solubility. This indicates that some of the oxygen is present as oxides or slag [42].

4.2 Carbon

The solubility of carbon in liquid silicon and ferrosilicon is given in the literature by the equilibrium between SiC (s) and Si (l) [28-34]. The solubility can be described by the equation

$$\log_{10} [\% C] = -\frac{9736}{T} + 3.53 - \log a_{Si} - \log f_C \quad (10)$$

where the activity coefficient for carbon in liquid silicon can be expressed similar to eqn (9)

$$\log_{10} f_C = e_C^{Al} [\% Al] + e_C^{Fe} [\% Fe] + r_C^{Al} ([\% Al])^2 + r_C^{Fe} ([\% Fe])^2 \quad (11)$$

Here are e_C^C , $r_C^{Al,Fe}$ as well as higher order interaction coefficients assumed to be zero. In Figure 3 the solubility of carbon in liquid (ferro)silicon is shown as a function of the temperature. We see that carbon solubility decreases with increasing iron content. Carbon solubility in FeSi65 seems to be only half of that in pure silicon.

In Figure 4 the solubility of carbon is presented versus the amount of aluminium in the alloy at 1550°C. As seen from this figure the aluminium content has some effect on the carbon oxygen solubility in these alloys. One % Al by mass seems to increase the carbon solubility by about 50%. This may indicate that if we remove Al from (ferro)silicon melts we should simultaneously precipitate some SiC particles.

The ladle metallurgy operations normally used in (ferro)silicon industries (oxidation and slag treatment) are capable of bringing carbon contents from say 1000 - 2000 ppm by mass down to levels roughly 10 times lower. This seems to correspond to carbon contents slightly above the

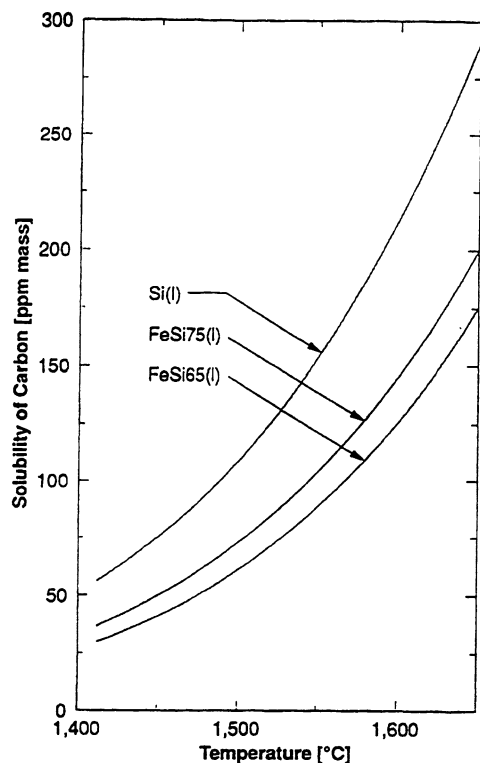


Figure 3. Solubility of carbon in pure silicon, 75% FeSi and 65% FeSi based on thermodynamic data from Ottem [28]

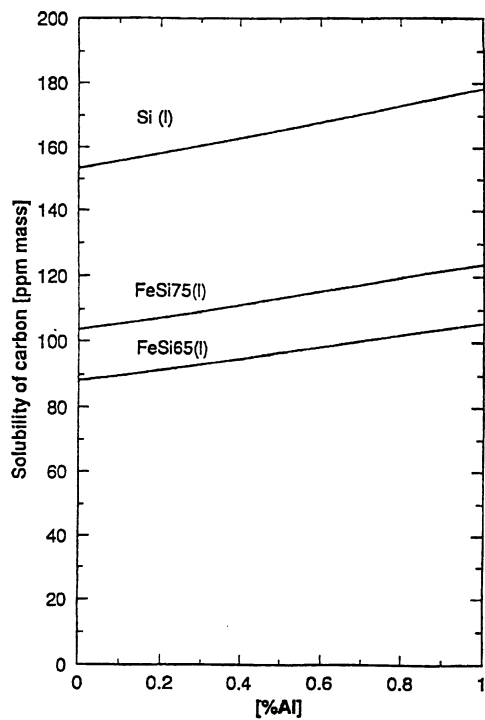


Figure 4. The effect of aluminium on the solubility of carbon in pure silicon, 75% FeSi and 65% FeSi at 1550°C. (Based on thermodynamic data by Ottem [28])

solubility limits at typical casting temperatures. Standard methods for analysing carbon do not normally distinguish between dissolved carbon and carbon bound as SiC particles. It is commonly believed that carbon during ladle refining is removed as SiC particles adhering to the slag phase and side walls. Investigations of SiC contents before and after refining indicate that the number of SiC particles is significantly lowered during refining [4,42]. However, thermodynamic calculations indicate that removal of dissolved carbon as CO (g) is also feasible [42]. Such removal has been performed in laboratory scale experiments [12,14]. Since we know very little about the kinetics of SiC formation in the (ferro)silicon melts we probably cannot exclude the possibility that carbon removal in practice is a combination of mechanical removal of SiC particles and oxidation of dissolved carbon [42].

5 SOME COMMENTS ON IMPORTANT TRACE ELEMENTS

Aluminium, calcium and magnesium can be removed to fairly low levels from the molten (ferro)silicon by an oxidation process [7,8]. The oxidation may include purging

in a ladle with an oxygen containing gas, refining with a slag containing silica or a combination of these processes.

Fairly low titanium contents are usually specified in silicon for the chemical industries as well as in some applications of ferrosilicon [7]. So-called High Purity FeSi used in grain oriented steel qualities has the most strict requirements on Ti. Some authors have claimed that chlorine additions to the melt removes some titanium [43]. However, chlorination is usually not considered as an environmentally acceptable process. The usual oxidation process for removing Al and Ca has no effect on the titanium content [1,7,8]. With todays practice there is hardly any way to remove Ti from the molten state, thus the only option at present seems to be the use of low Ti raw materials. A chemical purification process (leaching), utilising favourable segregation effects during solidification, might remove titanium as well as other metallic impurities [2]. However, a leaching process is costly and is presently not considered as an industrial scale alternative.

Low boron and phosphorus in (ferro)silicon are also specified for some applications [7]. Some boron can be removed by treatment with slag [8,44] or plasma [12,15,16] while it has been reported that phosphorus can be removed by vacuum treatment [12,45]. However, such processes are currently hardly an alternative for bulk products. At present, as for Ti careful selection of raw materials is the only practically feasible way to control the content of these elements.

6. CONCLUSIONS

The thermodynamics of liquid silicon based alloys, solubilities, activity coefficients and interaction coefficients in the Wagnerian representation, have been collected and tabulated. The collected data reveal some discrepancies in the solubility data for carbon, hydrogen, oxygen and nitrogen.

The available thermodynamic data have been employed to calculate the solubility of oxygen and carbon in some commercial silicon based alloys. Low Al contents (< 1% by mass) have a relatively large effect on carbon and oxygen solubility in the alloys.

The solubilities of oxygen and carbon may determine the lowest limits for the oxygen and carbon that can be achieved by ladle metallurgy operations.

ACKNOWLEDGEMENT

The professors T.A. Engh and J.K. Tuset at the Norwegian Institute of Technology are gratefully acknowledged for giving valuable comments and corrections to this work.

7. REFERENCES

1. J.K. Tuset, "Principles of silicon refining", International seminar on refining and alloying of liquid aluminium and ferro-alloys, August 26 - 28, 1985, pp.50 - 69
2. A. Schei, "High purity silicon production", International seminar on refining and alloying of liquid aluminium and ferro-alloys, August 26 - 28, 1985, pp.71 - 89
3. M. Balbi, G. Tosi, R. Zoja, and F. Borile, "Sulle inclusioni non metalliche nel ferro silico", La Fonderia Italiana, No.10, 1976, pp.45 - 49
4. O.S. Klevan and T.A. Engh, "Dissolved impurities and inclusions in FeSi and Si. Development of a filter sampler", INFACON 7, Trondheim, June 11-15, 1995, pp.441-453
5. A.G. Forwald, H.M. Rong and G. Vogelaar, "Oxygen in silicon; occurrence and influence on the direct process to methylchlorosilanes", Silicon for the Chemical Industry II, Loen, Norway, June 8 - 10, 1994, pp.107 - 119
6. M. Balbi and G. Caironi, "Non-metallic inclusions in ferro-alloys used in stainless steel manufacture", Avesta Stainless Bulletin, No.4, 1982, pp.14 - 19
7. J.K. Tuset, "Ferrosilicon and silicon refining", Silicon and Ferrosilicon Refining Course, Nashville, TN, Nov.13, 1994
8. T. Weiss and K. Schwerdtfeger "Chemical equilibria between silicon and slag melts", Met. Trans. B, Vol.25B, August, 1994, pp.497 - 504
9. D. Haaland, L. Lindstad and J.K. Tuset, "Use of alkali oxide slags in silicon refining", Silicon for the Chemical Industry II, Loen, Norway, June 8-10, 1994, pp.271-281
10. J.K. Tuset, L. Ottem and R. Livik, "Principles of silicon refining", Silicon for the Chemical Industry, Geiranger, Norway, June, 1992, pp.1 - 10
11. L. Nygård, "Alloying of silicon and its influence on reactivity", Silicon for the Chemical Industry, Geiranger, Norway, June, 1992, pp.47 - 52
12. Y. Sakaguchi, N. Yuge, H. Baba, K. Nishikawa, H. Terashima and F. Aratani, "Metallurgical purification of metallic grade silicon up to solar grade", 12th European PV solar energy conf., April 11-15, Amsterdam, 1994, pp.971 - 974
13. T. Ikeda and M. Maeda, "Refining of silicon for solar cells", 1st Processing Materials for Properties conf., Nov. 7 - 10, Honolulu, Hawaii, 1993, pp. 441-444
14. K. Sakaguchi and M. Maeda, "Decarburization of silicon melt for solar cells by filtration", Met. Trans. B, Vol. 23B, August, 1992, pp.423 - 427
15. P. Humbert, R.Combes, J.Erin, N. Madigou, D. Morvan and J. Amoroux, "Elaboration of photovoltaic silicon by a plasma process and its characterization", 10th European PV solar energy conf., April 8 - 12, 1991, Lisbon, pp.261 - 266
16. D.Morvan, J.Erin, I. Cazard-Juvenat and J.Amouroux, "Heat and mass balance on the silicon purification process. Properties of the material", 12th European PV solar energy conf., April 11-15, Amsterdam, 1994, pp.961-964
17. E.T. Turkdogan, Physical chemistry of high temperature technology, Academic Press, New York, 1980
18. D.R. Gaskell, Introduction to metallurgical thermodynamics, 2nd Edition, Hemisphere Publishing Corp., New York, 1981
19. T.A. Engh, Principles of metal refining, Oxford University Press, Oxford, 1992

20. O. Kubaschewski, C.B. Alcock and P.J. Spencer, Materials thermochemistry, 6th Ed., Pergamon Press, Oxford, 1993
21. C. Wagner, Thermodynamics of alloys, Addison-Wesley, Reading, Massachusetts, 1952
22. H. Schenk, M.G. Froberg and E. Steinmetz, "Ableitungen zur Begriffsbestimmung thermodynamischer Wirkungs-größen in Mehrstoffsysteme", Archiv Eisenhüttenwesen, Vol.31, H.11, Nov., 1960, pp. 671 - 676
23. C.H.P. Lupis and J.F. Elliott, "Generalised interaction coefficients", Acta Metallurgica, Vol.14, April, 1966, pp. 529 - 538
24. C.H.P. Lupis, "On the use of polynomials for the thermodynamics of dilute metallic solutions", Acta Metallurgica, Vol.16, Nov., 1968, pp. 1365 - 1375
25. A.D. Pelton and C.W. Bale, "A modified interaction parameter formalism for non-dilute solutions", Met. Trans. A., Vol.17 A, 1986, pp.1211 - 1215
26. C.W. Bale and A.D. Pelton, "The Unified Parameter Formalism: Thermodynamic Consistency and applications", Metall. Trans. A., Vol.21A, July, 1990, pp.1997 - 2007
27. C.L. Yaws, L.L. Dickens, R. Lutwack and G. Hsu, "Semiconductor silicon: Physical and thermodynamic properties", Solid State Techn., Jan., 1981, pp.87-92
28. L. Ottem, "Løselighet og termodynamiske data for oksygen og karbon i flytende legeringer av silisium og ferrosilisium", SINTEF report STF34 93027, 1993
29. Y. Iguchi and T. Narushima, "Solubility of oxygen, nitrogen and carbon in liquid silicon", 1st Processing Materials for Properties conf., Nov. 7-10, Honolulu, Hawaii, 1993, pp.437 - 440
30. L.L. Oden and R.A. McCune, "Phase equilibria in the Al-Si system", Met. Trans. A. 1987, Vol.18A, p. 2005 -
31. R.I. Scace and G.A. Slack, "Solubility of carbon in silicon and germanium", J. Chem.Phys., Vol.30, No.6, 1959, pp.1551-1555
32. R.N. Hall, "Electrical contacts to silicon carbide", J. Appl. Phys., Vol.29, No.6, 1958, pp.914 - 917
33. R.T. Dolloff, WADD Technical Report, Wright Air Development Division, 1969, pp.60 - 143
34. M. Hansen and S. Anderko, Constitution of Binary Alloys, 2nd Ed., McGraw Hill, New York/ London/ Toronto, 1958
35. T. Narushima, K. Matsuzawa, Y. Mukai and Y. Iguchi, "Oxygen solubility in liquid silicon", Materials Trans. JIM, Vol.35, No.8, 1994, pp.522 - 528
36. S.W. Tu and D. Janke, "On the oxygen solubility in molten silicon", Z. Metallkd., Vol.85, No.10, 1994, pp.701 - 704
37. H. Hirata and K. Hoshikawa, "Oxygen solubility and its temperature dependence in a silicon melt in equilibrium with solid silica", J. Crystal Growth, Vol.106, 1990, pp.657 - 664
38. A.E. Organ and N. Riley, "Oxygen transport in magnetic Czochralski growth of silicon", J. Crystal Growth, Vol. 82, 1987, pp.456 - 476
39. S. Otsuka and Z. Kozuka, "Thermodynamic study of the oxygen in liquid elements of group Ib to VIb", Trans. Japan Inst. Metals, Vol.22, No.8, 1981, pp.558 - 566
40. X. Huang, K. Terashima, H. Sasaki, E. Tokizaki and S. Kimura, Jpn. J. Appl. Phys., Vol.32, 1993, p.3671 -
41. A.I. Zaitsev, M.A. Zemchenko and B.M. Mogutnov, "Thermodynamic properties of $\{(1-x)\text{Si} + x\text{Fe}\}(l)$ ", J. Chem. Thermodynamics, 1991, Vol.23, pp.831 - 849
42. O.S. Klevan, "Inclusions and dissolved elements in ferrosilicon" Dr. Ing.-thesis in progress, Norwegian Institute of Technology, 1996
43. T. Grong, "Raffinering av ferrosilicium m.h.p. Al, Ca og Ti. Fremstilling av legering for anvendelse i produksjon av kornorientert elektroteknisk blikk", SINTEF report 340231, Jan. 26, 1967
44. K. Suzuki, T. Sugiyama, K. Takano and N. Sano, J. Jpn. Inst. Met., Vol.54, 1990, pp.168 - 172
45. J. Dietl, "A metallurgical route to solar grade silicon", Eight E.C. photovoltaic conf., 1988, pp.599 - 605
46. P.R. Elliot, Constitution of binary alloys. First Suppl., McGraw Hill, New York, 1965
47. G. Volkert and K.-D. Frank, Metallurgie der Ferrolegierungen, Springer Verlag, Berlin, 1972
48. R.W. Olesinski and G.J. Abbaschian, "The C-Si (Carbon-Silicon) system", Bull. Alloy Phase Diagr., Vol.5, No.5, Oct., 1984
49. T.B. Massalski, Ed, Binary Alloy Phase Diagrams, Am. Soc. for Metals, Metals Park, Ohio, 1986, pp.589-590
50. T. Nozaki, Y. Yatsuragi and N. Akiyama, "Concentration and behaviour of carbon in semiconductor silicon", J. Electrochem. Soc., Vol.117, No.2, 1970, pp.1566-1568

51. M. Mitra and K.W. Lange "Hydrogen solubility in liquid iron-cobalt-silicon system", Ironmaking and Steelmaking, Vol.11, 1984, pp.74 - 82
52. H. Bester and K.W. Lange, "Wasserstofflöslichkeit in Eisen und flüssigen Eisen-Mangan-Chrom- und -Silicium-Legierungen", Stahl und Eisen, Vol.97, 1977, pp.1037-1039
53. M.G. Froberg and S. Anik, "Über die Vorausbestimmung der Wasserstofflöslichkeit in binären Eisenschmelzen", Arch. Eisenhüttenwesen, Vol.55, No. 2, Februar, 1984, pp.45-48
54. B.A. Baum, T.K. Kostina, K.T. Kurochkin and P.V. Gel'd, Izv. VUZ Chernaya Metall., No.4, 1970, pp.34-39
55. T.K. Kostina, B.A. Baum, P.V. Gel'd and K.T. Kurochkin, Izv. Akad. Nauk SSSR, Met., Vol.4, 1971, pp.115-117
56. T.K. Kostina, B.A. Baum, K.T. Kurochkin and P.V. Gel'd, Zh. Fiz. Khim., Vol.45, No.4, 1971, pp.813-817 and T.K. Kostina, B.A. Baum, K.T. Kurochkin and P.V. Gel'd, Russ. J. Phys. Chem., Vol.45, 1971, pp.453-455
57. Y. Yatsuragi, N. Akiyama and Y. Endo "Concentration, solubility and equilibrium distribution coefficient of nitrogen and oxygen in semiconductor silicon", J. Electrochem. Soc., Vol.120, No.7, 1973, pp.975-979
58. W. Kaiser and C.D. Thurmond. "Nitrogen in silicon", J. Appl. Phys., Vol.30, No.3, 1959, pp.427-431
59. R. Noguchi, K. Suzuki, F. Tsukihashi and N. Sano, "Thermodynamics of boron in a silicon melt", Met. Trans. B, Vol.25B, Dec., 1994, pp.903-907
60. C.R. Taylor and J. Chipman, Trans. AIMME, Vol.154, 1943, p.228
61. E.A. Brandes, Ed. Smithell's Metals Reference Book, 6th Ed., Butterworth & Co, London, 1983, Ch.12
62. T. Carlberg, "Calculated solubilities of oxygen in liquid and solid silicon", J. Electrochem. Soc., Vol.133, No.9, 1986, pp.1940-1942
63. T. Carlberg, T.B. King and F. Witt, F., "Dynamic oxygen equilibrium in silicon melts during crystal growth by the Czochralski technique", J. Electrochem. Soc., Vol.129, No.1, 1982, pp.189 - 193
64. W. Kaiser and P.H. Keck, "Oxygen content of silicon single crystal", J. Appl. Phys., Vol.28, No.8, 1957, pp.882-887
65. V.E. Shevtsov, Izv. V.U.Z. Chernaya Metallurgia, Vol. 11, 1979, pp.5-7
66. P.D. Desai, "Thermodynamic properties of selected binary aluminium alloy systems", J. Phys. Chem. Ref. Data, VI.16, No.1, 1987, pp.109-124
67. A.F. Loseva, A.I. Al'mukhamedov, V.N. Tyumentsev and M.A. Luzhnova, "Thermodynamic properties of liquid aluminium-silicon alloys", Russ. J. Phys. Chem., Vol.51, No.2, 1977, pp.290-291
68. G.I. Batalin, E.A. Belobodorova, A.N. Shlapak, I.V. Nikolaenko and V.P. Kurach "Heats of formation of liquid aluminium-silicon alloys", Russ. J. Phys. Chem., Vol.55, No.6, 1981, pp.888-890
69. S.T. Rostovtsev, S.I. Khitrik, B.I. Emlin, M.I. Gasik and A.I. Pogrebnyak, "Activity of the components in binary Si-Al, Si-Mn and Si-Cr alloys", Izvest. VUZ Chernaya Met., No.2, 1971, pp.61-63
70. R.W. Olesinski and G.J. Abbaschian, "The B-Si (Boron - Silicon) system", Bull. Alloy Phase Diagrams, Vol.5, No.5, 1984, pp.478-484
71. Yu.O. Esin, S.P. Kolesnikov, V.M. Baer and A.F. Ermakov, "Enthalpies of formation of liquid alloys of silicon with boron", Tzisy Nauchn. soobshch. Uses konf. Str. Svoistvam Met. Shlavkovykh Rasplavov, 3rd Ed, Vol.2, 1978, pp.182 - 183
72. E. Schürmann, P. Fünders and H. Litterscheidt, "Dampfdruck des Calciums über Calcium-Silicium- und Calcium-Aluminium sowie über Calcium-Aluminium-Silicium-Legierungen", Arch. Eisenhüttenwesen, Vol.46, No.8, August, 1975, p.473
73. V.S. Sudavtsjova and G.I. Batalin,, "Thermodynamic properties of binary melts of the systems Ca - Si (Sn)", Izv. Akad. Nauk SSSR. Inorganic Materials, Vol.24, No.9, 1988, pp.352-354
74. M.S. Petrushevskii and G.M. Ryss, "Evaluation of activities of the components of Ce-Si and Ce-Al melts", Russ. Metall., No.4, 1986, pp.36-40
75. K. Schwerdtfeger and H.J. Engell, "Die freie Bildungsenthalpie von Siliziumoxyd und die Aktivitäten von Silizium in flüssigem Eisen und Kobalt", Arch. Eisenhüttenwesen, Vol.35, 1964, pp.533-544
76. T.G. Chart, "Thermochemical data for transition metal-silicon systems", High Temp.- High Press., Vol.5, 1973, pp.241-251
77. G.I. Batalin, T.P. Bondarenko and V.S. Sudavtsjova, "Heats of formation of molten alloys of the Si-Fe-Mn-system", Ukr. Khim. Zh., Vol.50, No.2, 1984, pp.187-190
78. M.S. Petrushevskii, "Calculating the activities if the components of the Fe-Co-Si system", Izv. VUZ Cherniya Metall., No.10, 1978, pp.16-19

79. V.T. Witusiewicz, "Thermodynamic properties of liquid alloys of 3d transition metals with metalloids (silicon, carbon and boron)", L. Alloys and Compounds, Vol.203, 1994, pp.103-116
80. B.S. Sudavtsjova, G.I. Batalin and Kurach, "Enthalpies of formation of alloys of silicon with scandium in liquid state", Ukr. Khim. Zh., Vol.50, No.4, 1984, pp.339-340
81. R.J. Freuhan, "The thermodynamic properties of liquid Fe-Si Alloys", Met. Trans., Vol.1, 1970, pp.865-870
82. T.G. Chart., "A critical assessment of the thermodynamic properties of the system iron-silicon", High Temp. - High. Press., Vol.2, 1970, pp.461 - 470
83. S. Tszen-Tszi, AV. Polyakov and A.M. Samarin, A.M., Izv. Vysshikh Uchebn. Zavedenii Chem. Met., No.1, 1961, pp.12-20
84. L.S. Darken, Trans. Metall. Soc. AIME, Vol.239, 1967, p.80 -
85. J. Chipman, J.C. Fulton, N.Gocke and G.R. Caskey, "Activity of silicon in liquid Fe-Si and Fe-C-Si alloys", Acta Metallurgica, Vol.2, May, 1954, pp.439 - 450
86. Y.K. Rao and G.R. Belton, "Thermodynamic properties of Mg-Si system", Conf. Chemical Metallurgy - a tribute to Carl Wagner, Chicago, 1981, pp.75 - 96
87. J.M. Eldridge, E. Miller and K.L. Komarek, "Thermodynamic properties of liquid magnesium-silicon alloys. Discussion of the Mg-Group IVB systems", Trans. met. Soc. AIME, Vol.239, 1967, pp.775-781
88. K.-C. Chou and J.-J. Wang, "Calculating activities from the phase diagram involving an intermediate compound using its entropy of formation", Met. Trans. A, Vol.18A, February 1987, pp.323-326
89. A. Tanaka, "The determination of the activities in Mn-C and Mn-Si melts by the vapor pressure measurement", Trans. Jpn. Inst. Met., Vol.20, No.9, 1979, pp. 516-522
90. M.S. Petrushevskii, P.V. Kocherov, P.V. Gel'd, V.M. Zamyatin and S.I. Suchil'nikov, "Thermodynamic properties of liquid manganese-silicon alloys", Russ. J. Phys. Chem., Vol.47, No.1, 1973, p.158-
91. G.I. Batalin and V.S. Sudavtsjova, Ukrain Khim. Zhur., Vol.40, 1974, pp.542-543
92. G.I. Batalin and V.S. Sudavtsjova, Izv. AN SSSR Neorg. Materiali, Vol.11, No.10, 1975, pp.1782-1786
93. N. Ahmad and J.N. Pratt, "Thermodynamic properties of liquid manganese - silicon alloys", Met. Trans., Vol.9A, 1978, pp.1857-1863
94. R. Gee and T. Rosenqvist, "Activities in liquid Fe-Mn-Si alloys", Scand. J. Met., Vol.7, 1978, pp.38-41
95. A.I. Zaitsev, M.A. Zemchenko and B.M. Mogutnov, "Thermodynamic properties of molten manganese-silicon alloys", Rasplav., Vol.3, No.2, 1989, pp.87-95
96. P.V. Gel'd, M.S. Petrushevskii, Yu.O. Esin and Yu.V. Gorbunov, "Enthalpy of formation and short range order structure of molten alloys of manganese with silicon, germanium and tin" Dokl. AN SSSR, Vol.217, No.5, 1974, pp.1114-1117
97. Yu.O. Esin, Yu.V. Gorbunov, M.S. Petrushevskii and P.V. Gel'd, "Enthalpies of formation of molten alloys of manganese with silicon", Izv. Vyzov. Chem. Met., No.2, 1975, pp. 8-11
98. R. Gee and T. Rosenqvist, "The vapour pressure of liquid manganese and activities in liquid Mn-Si and carbon saturated Mn-Si alloys", Scand. J. Met., Vol.5, 1976, pp.57-62
99. V.S. Sudavtsjova, G.I. Batalin and V.S. Tutevich, "Thermodynamic properties of binary Si - (V, Nb, Mo) melts", Russ. J. Phys. Chem., Vol.59, No.9, 1985, pp.1282-1283
100. V.S. Sudavtsjova, G.I. Batalin and V.S. Tutevich, "Thermodynamic properties of alloys of the Si - Ti (Zr) systems", Izv. Akad. Nauk SSSR, Inorg. Mat., Vol.21, No.5, 1985, pp.676-679
101. Yu.O. Esin, M.G. Valishev, A.F. Ermakov, P.V. Gel'd and M.S. Petrushevskii, "Enthalpy of formation of liquid binary alloys of vanadium and titanium with silicon", Izv. Akad. Nauk SSSR, Metall., No.2, 1981, pp.95-96
102. M.S. Petrushevskii and G.M. Ryss, "Calculation of the activities of the components in binary melts of yttrium with aluminium or silicon", Russ. J. Phys. Chem., Vol. 60, No.5, 1986, pp.915-917
103. M.G. Frohberg and S. Anik, "Thermodynamic relations between component activities and gas solubilities in binary metallic systems", Ber. Bunsenges. Phys. Chem., Vol.89, 1985, pp.130-134
104. V. Raghavan, Phase Diagrams of ternary iron alloys. Part I, The Indian Institute of Metals, 1987
105. T. Narushima, K. Matsuzawa, M. Mamiya and Y. Iguchi, "Oxygen solubility in liquid Si-X (X=Sb, B, P and As) alloys", To be published, 1995

2.3 Thermal and physical data of silicon and ferrosilicon

As mentioned in the introduction to chapter 2, the most important physical properties when modelling refining processes are density, heat capacity, surface and interfacial tension, viscosity and thermal conductivity. For pure metals or metals with small contents of alloying elements, such data exist to a large extent. However, properties of alloys with higher contents of alloying elements, such as FeSi, FeMn, SiMn and FeCr, do not seem to have been properly investigated in all cases. In this work the intention was to collect available physical data of ferrosilicon alloys, especially in the liquid state and with a silicon content from 50 to 100 mass%. Since we regard ferrosilicon as silicon alloyed with iron, the physical properties of pure silicon are also included in this section.

In some fields the physical data were rather scarce and there were large discrepancies between the different investigators, especially at high temperatures. The experimental method employed and the accuracy of the measurements was considered when selecting the actual physical data.

Due to lack of available data, it became necessary to estimate the enthalpy and heat capacity of ferrosilicon alloys.

2.3.1 Density

Liquid metal density is an important physical property working with refining or slag/metal interactions. The physical segregation of slags and liquid metals, or the terminal velocity of nonmetallic inclusions in melts is primarily determined by the density difference of the different phases. Accurate measurements of liquid metal density are therefore of great importance from a technological and scientific point of view.

Silicon

The density of silicon at room temperature (298K) has been measured by Yaws et al. [1] to be 2329 kg/m³. Yaws et al. [2] have also predicted the temperature dependence of the density from 293K up to the melting point $T_m = 1685$ K

$$\rho(\text{Si})_{\text{sol}} = 83.27 - 1.0525 \times 10^{-3} \times T \quad [\text{kmol/m}^3] \quad (2.1)$$

which gives

$$\rho(\text{Si})_{\text{sol}} = 2,338.7 - 0.0296 \times T \quad [\text{kg/m}^3] \quad (2.2)$$

Yaws et al. [2] have also measured the density of liquid silicon and given the relation between the density and the temperature as a ‘‘Rackett equation’’¹

$$\rho(\text{Si})_{\text{liq}} = \frac{1.3219}{0.10658^{(1+(1-T/4886)^{2/7})}} \quad [\text{kmol/m}^3] \quad (2.3)$$

This gives a density of liquid silicon at the melting point (1412 °C) of 2,533 kg/m³. Retaining the first two terms in the Taylor expansion at $T = T_m$, the equation

$$\rho(\text{Si})_{\text{liq}} = 2,533 - 0.45(T - T_m) \quad [\text{kg/m}^3] \quad (2.4)$$

is obtained. Iida and Guthrie [5] have proposed the following temperature dependence for the density of liquid silicon

$$\rho(\text{Si})_{\text{liq}} = 2,530 - 0.35(T - T_m) \quad [\text{kg/m}^3] \quad (2.5)$$

¹ The Rackett correlation is accurate in estimating the effect of temperature on liquid volumes [3,4].

In figure 2.1 the linear equation of Yaws is presented together with the equation from Iida and Guthrie [5] and it is seen that the difference between these curves is small at 1400 °C, but increasing up to 1900 °C.

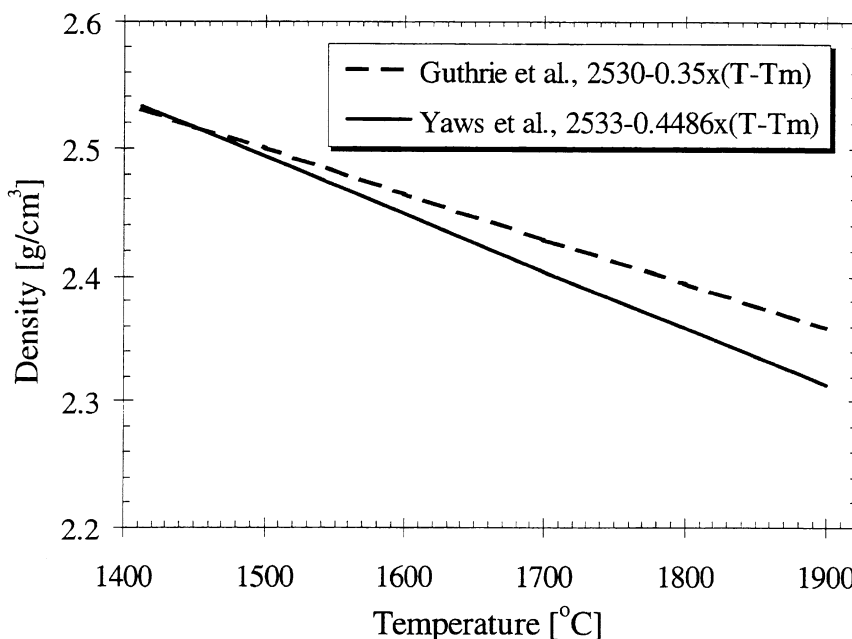


Figure 2.1: Density of liquid silicon in the temperature range T_m - 1900 °C after Yaws [2] and Iida and Guthrie [5]

Ferrosilicon

The density of liquid ferrosilicon alloys with different contents of silicon have been experimentally determined by a few investigators over the last years. Recently Dumay and Cramb [6] carried out measurements of the density of ferrosilicon alloys at 1450 °C. These measurements were performed by employing the X-ray sessile drop technique, which involves photographing the liquid metal drops and then determining their volume by geometrical analysis of the photographs. Reported error in the use of the sessile drop technique is ± 2 per cent for iron, cobalt and nickel up to 2023 K [5].

The experimental density measurements of liquid ferrosilicon alloys carried out by Dumay and Cramb [6] at 1450 °C were carried out with silicon contents ranging from 16.3 to 78 mass%. In figure 2.2 the result from this investigation is presented together with the density for pure liquid silicon from equation (2.3). Including this end point in the experimental results from Dumay and Cramb gives the following relation between the density of liquid ferrosilicon and the silicon content in the alloy

$$\rho(1450^{\circ}\text{C}) = 7,106 \exp(-0.0107 \times \text{mass \% Si}) \quad [\text{kg/m}^3] \quad (2.6)$$

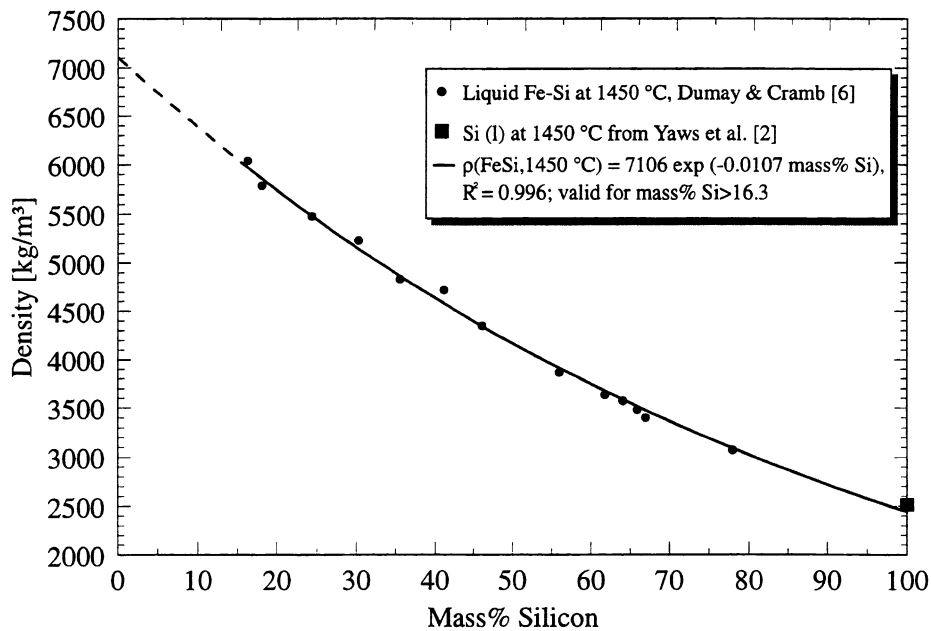


Figure 2.2: Density of liquid ferrosilicon at 1450 °C

Experimental data of the density of liquid ferrosilicon alloys at temperatures above 1450 °C were presented along with data by Dumay and Cramb [6]. The temperature dependency is expected to be negative. Olsson [7] investigated the change in density as a function of temperature in the range 1550 to 1700 °C for liquid iron containing small amounts of silicon (0 to 4.75 mass%), but the results are not conclusive concerning the relation between the slope, $d\rho/dT$, and the silicon

content in the alloy, other than that it is negative as for pure iron and pure silicon (eqn 2.1).

2.3.2 Heat capacity and enthalpy

Due to lack of proper heat capacity and enthalpy data for ferrosilicon alloys, it was found necessary to estimate these properties as a function of the temperature. The estimate was made using tabulated data on specific heat capacities for the pure elements, heats of transitions and melting and the heat of mixing for iron and silicon in their liquid state.

To obtain the enthalpy increment of ferrosilicon alloys, we need to have a proper estimate of the heat of melting for the compound FeSi_2 . The calculation of this value was carried out by employing a procedure described by H. Tveit [8] and is shown in figure 2.3.

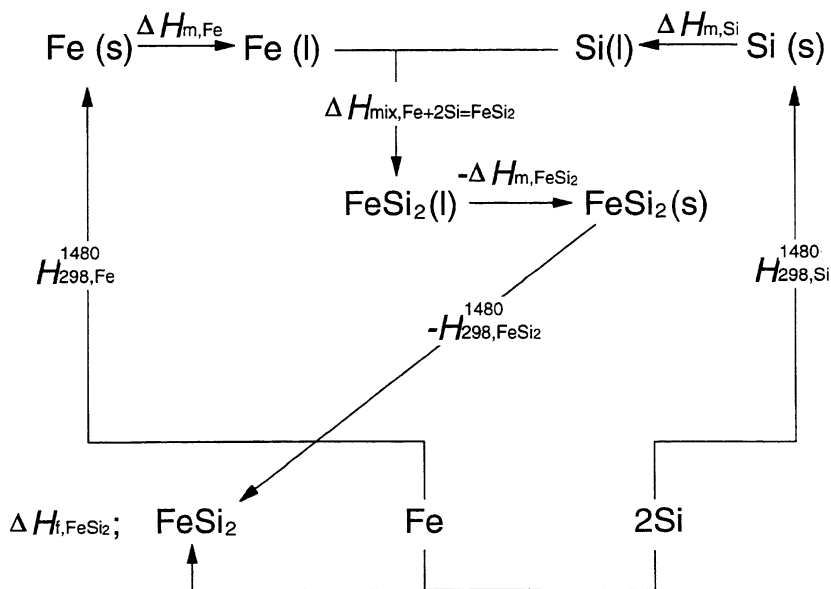


Figure 2.3: Model describing the procedure for determination of the heat of melting for FeSi_2 [8].

Mathematically this model can be expressed by the following equation

$$\Delta H_{f, FeSi_2} + H_{298, FeSi_2}^{1480} + \Delta H_{m, FeSi_2} =$$

$$H_{298, 2Si}^{1480} + \Delta H_{m, 2Si} + H_{298, Fe}^{1480} + \Delta H_{m, Fe} + \Delta H_{mix, Fe + 2Si = FeSi_2}$$
(2.7)

Employing the data in table 2.1, the enthalpy of melting of the compound FeSi₂ is calculated to be $\Delta H_m(FeSi_2) = 1010$ kJ/kg or 113 kJ/mol.

TABLE 2.1: Data for the Calculation of the Enthalpy of Melting for FeSi₂

	Value [kJ/kg]	Ref.
Heat of formation FeSi ₂ : $\Delta H_f(FeSi_2)$	-725	[9]
Heating FeSi ₂ : $H_{1480} - H_{273}$	859	[9]
Heating and melting 2Si: $(H_{1480} - H_{273} + \Delta H_m(Si))*2$	1433	[10]
Heating and melting Fe: $\Delta H_{1480} - \Delta H_{298} + \Delta H_m(Fe)$	524	[10]
Heat of mixing: Fe(l) + 2Si(l) = FeSi ₂ (l)	-813 ^{*)}	[11]

^{*)} Applies at 1600 °C, but is assumed to be valid also at 1207 °C

Calculations of heat capacity and enthalpy

Table 2.2 gives references for the data used for the calculation of the heat capacity and enthalpy for different ferrosilicon alloys.

TABLE 2.2: References

Data	References
c_p Si(s), Si(l), Fe(l)	[10]
c_p FeSi ₂ (s)	[9]
ΔH_m (FeSi ₂)	this work
ΔH_m (Si)	[10]
ΔH_{mix} Fe, Si	[11]

The procedure for the calculations is as follows

- ▶ Si(s) and FeSi₂(s) is heated from zero to 1207 °C.
- ▶ FeSi₂ is melted at 1207 °C
- ▶ Fe(l), Si(l), Si(s) is heated and Si is melted in 1 K temperature increments
- ▶ melted silicon is mixed with the melt giving a heat of mixing²
- ▶ the amount of solid silicon to be heated and melted at each ΔT is calculated from equation (2.8) and the lever rule is employed.

$$[\% \text{Si}] = 4.72770112 \times 10^{-8} T^4 - 2.41401818 \times 10^{-4} T^3 + 0.462392405 T^2 - 393.654709 T + 125707.356 \quad (2.8)$$

Calculated results showing the increase in enthalpy as a function of the temperature for the different ferrosilicon alloys are shown graphically in fig. 2.4.

² The heat of mixing is small. Highest for FeSi75 where it accounts for 0.1% of the total enthalpy.

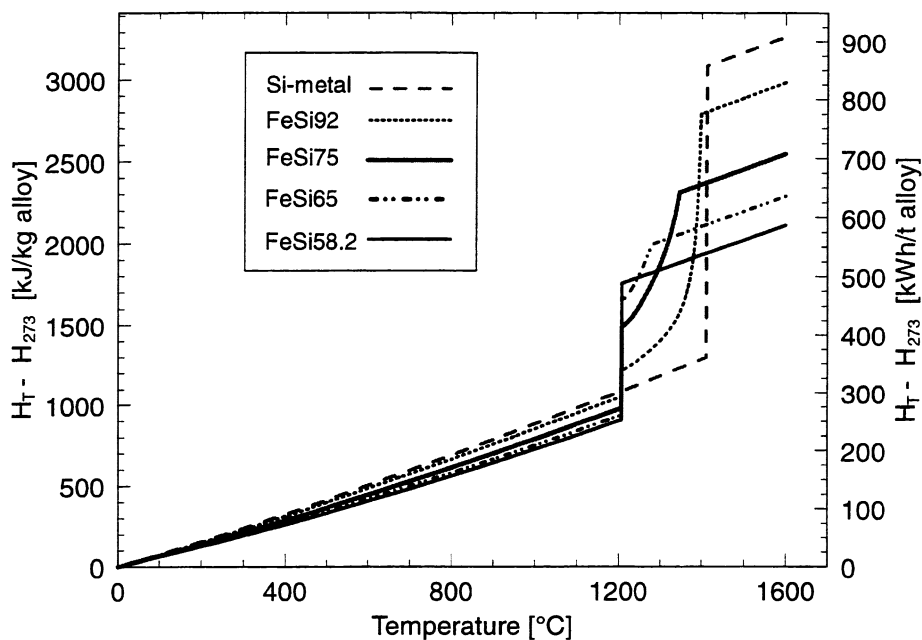


Figure 2.4: Enthalpy in Fe-Si alloys in the temperature range 0 - 1600 °C

Specific heat capacity, c_p , and heat of melting, ΔH_m , for these alloys are tabulated in table 2.3.

TABLE 2.3: Specific heat capacity and heat of melting for four different Fe-Si alloys and Si-metal

	FeSi58.2	FeSi65	FeSi75	FeSi92	Si-metal
$c_p(\text{sol})$ [J/kg K]	752	776	812	873	920
ΔH_m [kJ/kg]	857	1037	1322	1729	1798
$c_p(\text{liq})$ [J/kg K]	908	918	932	957	968

2.3.3 Surface and interfacial tension

Surface tension of Silicon

Smithells [12] gives 865 mN/m for the surface tension at the melting point and the following relation for the temperature dependency

$$\sigma = 865 - 0.13(T - T_m) \quad [\text{mN/m}] \quad (2.9)$$

S. C. Hardy [13] employed the sessile drop technique and found the surface tension of liquid silicon at 1450 °C to be 874 mJ/m². The temperature dependence of the surface tension was determined within the temperature range 1410 to 1600 °C to be

$$\sigma = 885 - 0.28(T - T_m) \quad [\text{mN/m}] \quad (2.10)$$

with an error in the gradient of 0.004 mN/(mK). The measurements were made on liquid silicon placed on a BN-cup and in flowing argon atmosphere. Hardy [13] found that the surface tension was lowered when the material was contaminated with oxygen. He also found that lowering of the surface tension by adsorption of a surface active component is often accompanied by a reduction of the temperature dependence and claims that this may be the reason for the scatter in results from the different investigators.

Surface Tension of Ferrosilicon

Utigard [14] has developed a model predicting the surface tension of iron based systems by employing equations describing the average surface chemical potential for the alloy, μ_{ave} and the molar surface area, Γ_{ave} . Fig. 2.5 shows the results obtained by Utigard [14] for the Fe-Si-system at 1600 °C where he has compared the model with experimental results from other investigators. The results obtained by the model are in good agreement with the experimental data. The result of S. C.

Hardy [13] for pure silicon is included. Partly, the discrepancy for Si may indicate that the curve in figure 2.5 should flatten more towards 100% silicon. Also, the content of impurities in Hardy's work may be less than for the alloys in Fig. 2.5. Thus, equation 2.10 gives a higher value for σ .

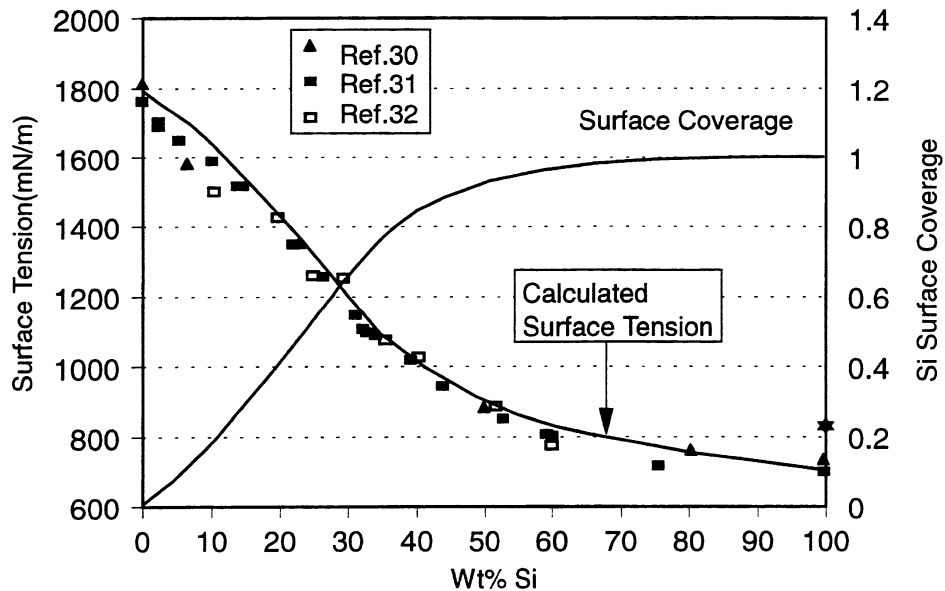


Figure 2.5: Experimental and calculated surface tension and surface coverage of Fe-Si [14]. The references 30-31 in the frame from [14]. The value obtained for Si from eqn (2.10) is added.

Interfacial tension between slag and ferrosilicon

The only work on metal/slag interfacial tensions found, was by Dumay and Cramb [6]. The experiments were carried out at 1450 °C employing the X-ray sessile drop technique, and involved alloys containing from 16.3 to 78 mass% Si. The experiments involved two different slags (slag 2 only for 65 mass% Si), whose compositions are given in table 2.4.

TABLE 2.4: Slag composition in the experiments performed by Dumay and Cramb [6]

Slag	Mass% CaO	Mass% SiO ₂	Mass% Al ₂ O ₃
1	46	36	18
2	42	42	16

The results of slag/metal interfacial measurements obtained by Dumay and Cramb are shown in figure 2.6

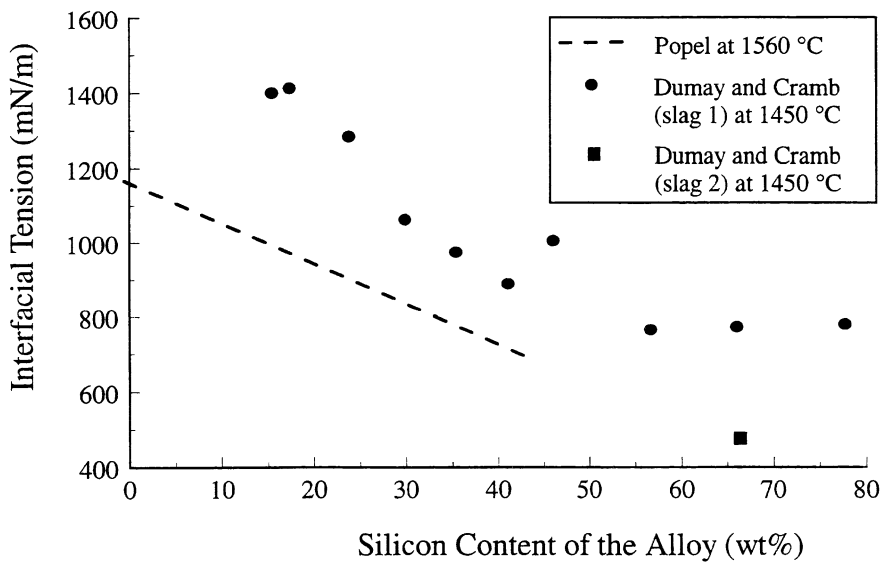


Figure 2.6: Interfacial tension measurements of Fe-Si alloys at 1450 °C [6]

2.3.4 Viscosity

Silicon

Yaws et al [2] give 0.88×10^{-3} Ns/m² for the dynamic viscosity of Si at the melting point which is somewhat lower than the figure, $\mu_m = 0.94 \times 10^{-3}$ Ns/m², found in Smithells [12]. Kocherov et al. [15] have experimentally given 3.16×10^{-7} m²/s for the kinematic viscosity at the melting point which corresponds to, $\mu_m = 0.8 \times 10^{-3}$ Ns/m². All these figures are somewhat low compare with the calculated value, $\mu_m = 2.49 \times 10^{-3}$ Ns/m², employing a theory cited by T. A. Engh [16]. Engh [16] has also compared the calculated values with experimental values and found good agreement for most of the metals. However, silicon is a metalloid and probably shows the same range of deviation from the theory as Ge and Sb.

Yaws et al. [2] have also predicted the viscosity versus the temperature in the range 1685 to 3151K:

$$\mu = \exp\left(-13.327 + \frac{8,345}{T} + 0.18163 \ln(T)\right) \quad [\text{Ns/m}^2] \quad (2.11)$$

This relation is presented graphically in figure 2.7 together with the results of Kocherov et al. [15], who have carried out experimental measurements on the kinematic viscosity of pure silicon and Fe-Si alloys.

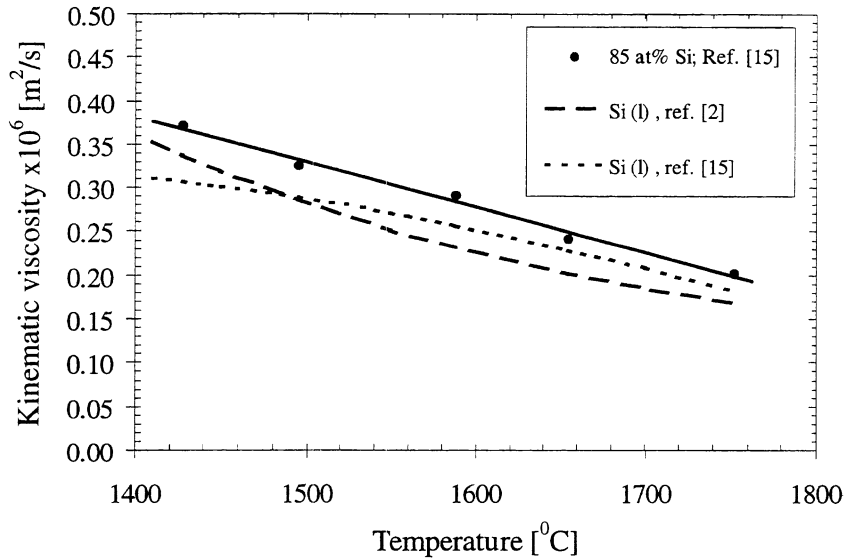


Figure 2.7: Kinematic Viscosity of silicon and Fe-Si with 85 at% Si (74 mass%)

Ferrosilicon

Experimental measurements of the viscosity for different ferrosilicon alloys have also been given by Kocherov et al. [15]. The results obtained for Fe-Si alloy with 85 at% Si (equals 74 mass% Si) are shown in figure 2.7 together with the kinematic viscosity for silicon from both Kocherov et al. [15] and Yaws et al. [2].

2.3.5 Electrical and thermal conductivity

Silicon

According to Iida and Guthrie [5] the electrical resistivity for silicon at the melting point is $\sim 2400 \mu\Omega\text{cm}$ in solid state and $\sim 81 \mu\Omega\text{cm}$ in liquid state. The electrical resistivity increases linearly with increasing temperature for most liquid metals [5] and for liquid silicon it is given by this equation for the temperature range from T_m to 1820 K [5]:

$$\rho_e(\text{Si}) = -113 + 0.113 \times T \quad [\mu\Omega\text{cm}] \quad (2.12)$$

A simple relationship exists between electrical and thermal conductivities of solid metals at high temperatures and is called the Wiedemann-Franz-Lorenz law, given by equation (2.13)

$$\frac{\lambda\rho_e}{T} = L \quad [\text{W}\Omega\text{K}^{-2}] \quad (2.13)$$

where

λ : Thermal conductivity

ρ_e : Electrical resistivity

L : Lorenz number (2.45×10^{-8})

T : Temperature (K)

Investigations indicate no significant changes in the Lorenz number from solid to liquid metals [5]. Employing eqn (2.13) gives a thermal conductivity of 52 W/mK for molten silicon at the melting point.

Ferrosilicon

H. Tveit [17] predicts the thermal conductivity for FeSi75 (75 mass% Si) up to 1400 °C based on extrapolations from experimental data. The results are shown in figure 2.8.

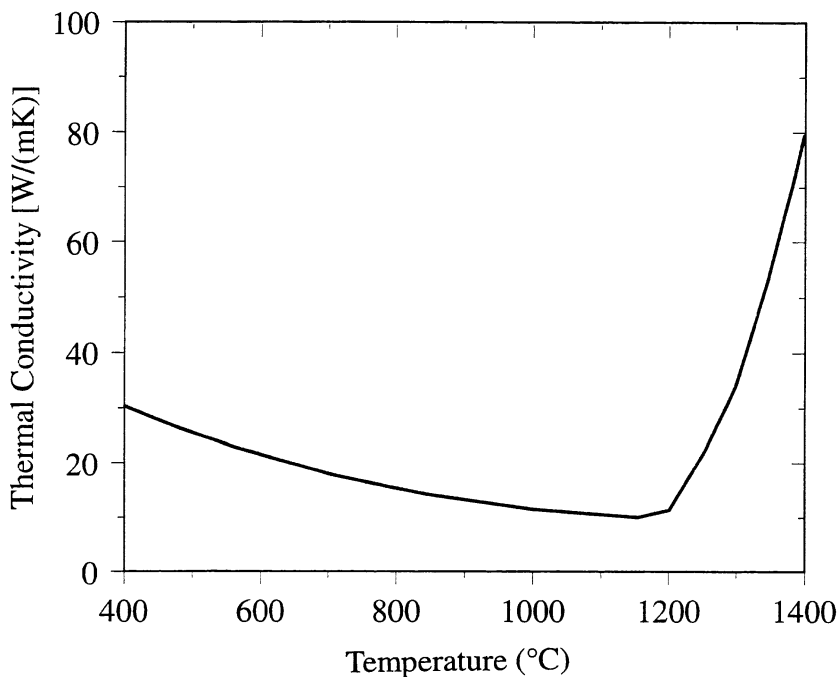


Figure 2.8: Thermal conductivity for FeSi75 (75 mass% Si) extrapolated from 900 °C to 1200 °C. Estimated values from 1200 °C [17].

2.4 Thermal and physical data and wettability of silicon carbide

As will be seen in chapter 3 and 4, silicon carbide plays an important role when discussing removal of carbon from (ferro)silicon. It was therefore necessary to collect physical and thermal data of silicon carbide.

2.4.1 Density

The density of silicon carbide has been measured by several workers. D. P. Birnie III and W. D. Kingery [18] have reported densities from 3.2073 to 3.2095 g/cm³

for silicon carbide crystals at 26.4 °C. The density of β -SiC is calculated from the lattice parameter to be 3.213 g/cm³ at 24 °C [19]. Other investigators give figures in the same range. The density of silicon carbide at higher temperatures can be estimated from the thermal expansion coefficient of SiC. Because of its high interatomic strength, SiC has a small thermal expansion and it is only 4.3×10⁻⁶ cm/°C for SiC- compacts [20]. E. L. Kern et al [21] report the density at 20 °C to be 3.166 g/cm³ and the thermal expansion to vary from 3.8×10⁻⁶ cm/°C at 200 °C to 5.5×10⁻⁶ cm/°C in the range 1400 -1800 °C for β -SiC. Krikorian [22] has given the thermal expansion as percent expansion for α -SiC between 25 and 2000 °C [22]. This gives an average thermal expansion of 5.94×10⁻⁶ cm/°C. The density at temperature T will be

$$\rho_T = \rho_{25^\circ\text{C}} \frac{V_{25^\circ\text{C}}}{V_T} \quad (2.14)$$

where V_T , for a cubic α -SiC with side length of 1 cm, is

$$V_T = (1 \text{ cm} + 5.94 \times 10^{-6} \text{ cm}/^\circ\text{C} \times (T - 25^\circ\text{C}))^3 \quad (2.15)$$

This gives a reduction in density of α -SiC from 3.21 g/cm³ at room temperature to 3.13 g/cm³ at 1450 °C.

In figure 2.9 the density as function of the temperature is given for α -SiC by a linearization of eqn (2.14) where the density at 25 °C is taken to be 3.21 g/cm³ [18,19] and for β -SiC employing the data from Kern et al. [21]. As seen from the figure below the difference between these two curves is only 31 kg/m³ or 1% at 1450 °C.

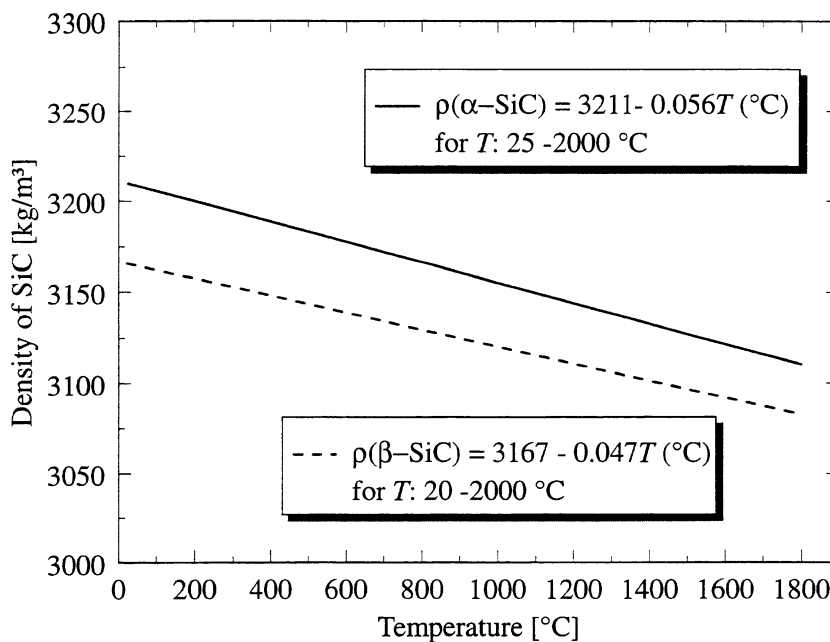


Figure 2.9: Calculated density for α -SiC(s) between 25 -2000 °C based on the expansion coefficient for α -SiC given by Krikorian [22] and for β -SiC based on the data given by Kern et al. [21].

2.4.2 Specific heat capacity

Gmelin [19] gives the following equation for the heat capacity for α -SiC above 273.15 K

$$c_p = 13.250 - 2035T^{-1} + 288 \times 10^5 T^{-2} \times e^{-5680/T} \quad [\text{cal/mol K}] \quad (2.16)$$

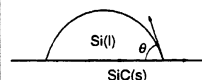
This gives a heat capacity of 670.4 J/(K kg) at 25 °C. Gmelin [19] has tabulated the heat capacity for β -SiC at temperatures below 300 K. The value presented at 298.15 K is 26.84 J/(K mol) or 669.4 J/(K kg) which is almost identical to the value of α -SiC at the same temperature.

of liquid metals on silicon carbide.

Naidich [24] has investigated the wettability of SiC by liquid silicon and found the contact angle to be $\theta = 36^\circ$. Nogi et al. [25] found that silicon spread immediately on SiC, but gives a review of the contact angle of Si (l) on SiC given by other investigators in the same paper [25], see table 2.5. Nikolopoulos et al. measured the contact angle of molten Si in contact with mono- and polycrystalline α -SiC and β -SiC by the sessile drop technique. The contact angle, θ , was about 38° for both types of α -SiC, whereas θ was measured to be 41.5° for β -SiC.

TABLE 2.5: Contact angle of Si(l) on SiC from [24,25]

	θ	Temp. [K]	ref.
Ju. V. Naidich	36°	1753	[24]
Ju. V. Naidich	42°	1703	[25]
B.S. Allen	35°	1723	[25]
A. J. Bevolo et al.	33°	1723	[25]
V. R. Yupko and G. G. Gnesin	45°	1723	[25]
K. Nogi and K. Ogino	0°	1773	[25]
Nikolopoulos et al. / α -SiC	38°	1683/1770	[26]
Nikolopoulos et al. / β -SiC	41.5°	1740	[26]



S. Kalogeropoulou et al. [27] measured the wettability of α -SiC by Fe-Si employing the sessile drop technique. Two Fe-Si alloys with 33.33 and 66.67 at% Si were examined in addition to pure iron. The contact angle was measured upon heating of the sample, and was measured to about 35° for both alloys at their respective melting points.

Wettability by slags

Wetting behaviour of silicate glasses on SiC was investigated by Yurkov and Polyak [28]. They investigated different types of oxides and found good or almost perfect wetting, with contact angles $\theta < 30^\circ$, at 1400°C for oxides containing 12-25 mass% Al_2O_3 , 5-17 mass% CaO and 25 -70 mass% SiO_2 . For oxides containing a high amount of B_2O_3 (15-30 mass%) and silica (70-78 mass%) the wettability was reported to be poor. There was no CaO in these oxides, whereas the amount of alumina was from 0-2 mass%.

References for chapter 2.3 and 2.4

1. Yaws, C.L., Dickens, L.L., Lutwack, R. and Hsu, G., "Semiconductor silicon: Physical and Thermodynamic Properties", *Solid State Technology* (1981), January, pp.87-92.
2. Yaws, C.L., Li, Ku-Yen, Hopper, J.R., Fang, C.S., Hansen, K.C., "Process Feasibility Study in Support of Silicon Material Task 1", *Final Report to Jet Propulsion Laboratory, California institute of Technology under NASA Contract NAS7100 for the U.S. Dept. of Energy, Division for Solar Energy* (February 6, 1981).
3. Rackett, H. G., "Equation of State for Saturate Liquids", *Journal of Chemical and Engineering Data*, **17** (1972) pp. 236-241
4. Spencer, C. F. and Danner, R. P., "Improved Equation for Prediction of Saturated Liquid Density", *Journal of Chemical and Engineering Data*, **15** (1970) pp. 514-517
5. Iida, T. and Guthrie, R.I.L., "*The Physical Properties of Liquid Metals*", Clarendon Press - Oxford, (1988).
6. Dumay, C., Cramb, A.W., "Communications: Density and Interfacial Tension of Liquid Fe-Si Alloys", *Metall. and Mater. Trans.B*, **26B** (1995) pp.173-176.
7. Olsson, A., "The Influence of C, Si and Mo on the Density of Liquid Iron", *Scand. J. Metallurgy* **10** (1981) pp.263-271.
8. Tveit, H., Unpublished work.
9. HSC Chemistry Database: Barin, I., "*Thermochemical Data for Pure Substances*", VCH Verlags Gesellschaft, Weinheim, (1989).
10. HSC Chemistry Database: Knacke, O., Kubaschewski, O., Hesselmann, K., "*Thermochemical Properties for Inorganic Substances*", Springer-Verlag Berlin, Heidelberg, (1991).
11. Kubaschewski, O., Alcock, C. B., Spencer, P. J., "*Materials Thermochemistry*", 6th ed., Pergamon Press, (1993).
12. Smithells, C. J. and Brandes, E. A. *Smithells Metals Reference Book 6th. edition* Butterworth, London (1983)
13. Hardy, S. C. "The Surface Tensions of Liquid Silicon", *Journal of Crystal Growth* **69** (1984) pp. 456-460
14. Utigard, T., "Surface and Interfacial Tensions of Iron Based Systems", *ISIJ*

- International*, **34** (1994), No.12, pp. 951-959.
15. Kocherov, P.V., Baum, B.A., Gel'd, P.V., "The Kinematic Viscosity of Liquid Alloys of the Iron-Silicon System", *Trudy Ural'Skogo Politekhn. Inst.*, **144** (1965), pp.139-141.
 16. Engh, T.A., *Principles of metal refining*. Oxford University Press (1992), pp. 92-100
 17. Tveit, H., "Størkning av 75 % Ferrosilium, Forløp, Struktur og Styrke", *Dr.ing. avh. 1988:53, Metallurg. Inst. NTH, Trondheim* (1988).
 18. Birnie III, D. P. and Kingery, W. D., "The limit of non-stoichiometry in silicon carbide", *Journal of Materials Science*, **25** (1990) pp. 2827 - 2834.
 19. Gmelin Handbook of Inorganic Chemistry, Suppl. vol. B2, 8th ed., Springer-Verlag, Berlin (1984) pp. 63-131
 20. Sōmiya, S and Inomata, Y., *Silicon Carbide Ceramics-1, Fundamental and Solid Reaction*, Elsevier Applied Science (1991)
 21. Kern, E. L., Hamill, D. W., Deem, H. W. and Sheets, H. D. "Thermal Properties of β -Silicon Carbide From 20 to 2000 °C", *Materials Research Bull.*, **4** (1969) pp. S 25 - S 32
 22. Krikorian, O. H., "Thermal Expansion Of High Temperature Materials", *Contract No. W-7405-eng-48, University of California, Lawrence Radiation Lab.*, Sept. 6, 1960. 7p.
 23. Stefanescu, D. M., Dhindaw, B. K., Kacar, S. A and Moitra, A., "Behaviour of Ceramic Particles at the Solid-Liquid Metal Interface in metal Matrix Composites", *Metallurgical Transaction A* **19A** (1988) pp. 2847-2855
 24. Naidich, Ju. V. "The Wettability of Solids by Liquid Metals", *Progress in surface and membrane science* **14** (1981) pp. 428 438,
 25. Nogi, K. and Ogino, K. "Wettability of Silicon Carbide by Liquid Metals" *Proc. Int. Symp. on Advanced Structural Materials* (1988) / edited by D. S. Wilkinson.
 26. Nikolopoulos, P., Agathopoulos, S., Angelepoulos, G. N., Naoumidis, A. and Grübmeier, H., "Wettability and interfacial energies in SiC-liquid metal systems", *Journal of Materials Science* **27** (1992) pp. 139-145
 27. Kalogeropoulou, S., Baud, L., and Eustathopoulos, N., "Relationship Between Wettability and Reactivity in Fe/SiC System", *Acta Metall. Mater.* **43** (3) (1995) pp. 907-912
 28. Yurkov, A. L. and Polyak, B. I., "Contact Phenomena and Interactions in the

System SiC-SiO₂-R_xO_y in Condensed Matter”, *Journal of Materials Science* **30** (1995) pp. 4469-4478

3. Sampling of Ferrosilicon for C-Analyses

Sampling of liquid silicon and ferrosilicon is mainly performed for analyses of the alloy with respect on the contents of the elements Al, P, Ca, Ti, and Ca besides Si. The common practice in the industry is to sample from the tapping stream or pouring stream employing a graphite scoop sampler. The sampled melt is then poured into a mould of graphite or copper to solidify. The solidified sample is then ground to powder. From this homogeneous powder a tablet is pressed suitable for X-ray spectrometry. Here it was found that this sampling technique is not suitable for the detection of the carbon content in the liquid metal. Therefore, an alternate sampling method had to be introduced.

3.1 Stream sampling

As mentioned above, sampling of the metal stream employing a graphite scoop sampler is the normal practice. To obtain samples without any contamination of carbon an oxidic sampler was developed. First we made a scoop sampler of chamotte quality, named TK40. The sampler was filled by the tapping stream and the collected metal poured into a copper mould for rapid solidification. Since there was a possibility for a reaction between the silica in the refractory and the carbon in the alloy, a scoop of high alumina (B85) was also tested. These two samplers, which are described in figure 3.1, gave the same result regarding the carbon content. Since the TK40 sampler is more easy and is much cheaper to manufacture, this one was chosen as the stream sampler in the following work.

For further control of this sampling method, stream samples was taken employing the MINCO Immersion Sampler. This sampler is described in detail in the following subchapter.

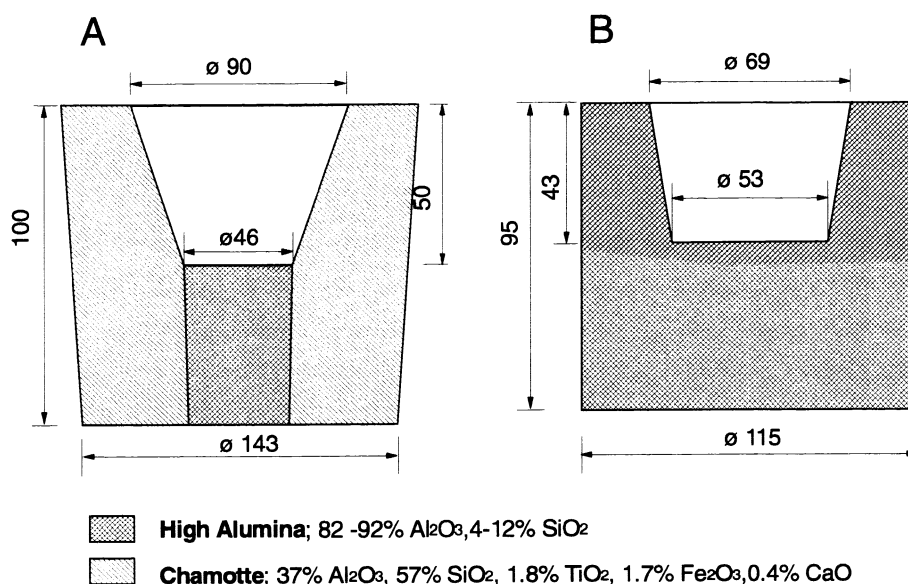


Figure 3.1: Oxidic scoop sampler for liquid ferrosilicon. A: Type TK40 made of mainly chamotte. B: Type B85 made of high alumina. All numbers are in mm

The MINCO Immersion sampler was held in the metal stream with the tedge (runner gate) upwards so the metal could flow freely into the mould. First consuming a number of samplers, we finally succeeded in drawing good and representative samples. To avoid any influence of changes in the metal composition, the samples were taken simultaneously with the oxidic scoop sampler. Samples were taken both from metal with a high carbon content, i.e. taken from the furnace tapping stream, and metal with an expected low carbon content, i.e. from the pouring stream during casting of refined ferrosilicon. The following analyses showed that the samples taken employing the immersion sampler consistently gave ~75% higher C content compared with the oxidic scoop sampler. Figure 3.2 shows the relation between these two sampling methods where

$$[\%C]_{\text{MINCO}} = 1.756 \times [\%C]_{\text{oxidic scoop}} \quad (3.1)$$

with $R^2 = 0.945$. It is proposed that the difference in analysis is due to transfer of

SiC particles from the melt to the walls of the scoop, a mechanism to be thoroughly discussed in chapter 4 and 5.

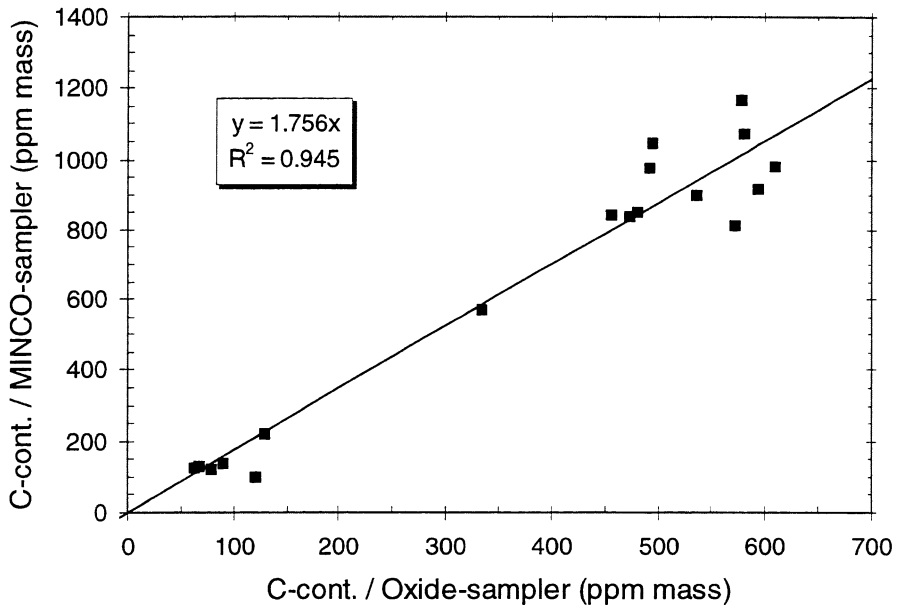


Figure 3.2: Relation between stream samples taken employing the MINCO immersion sampler and an oxidic scoop sampler.

Eight out of the eighteen samples in figure 3.2 were analysed with respect to Si, Al, Fe, Ti and P and it is seen from table 3.1 that the oxidic scoop sampler gives 53% less Ca in the metal compared with the Minco sampler. For the other elements the differences between these two sampling methods are small.

TABLE 3.1: Difference in content of Si, Al, Ca, Fe, Ti and P in FeSi75 sampled with oxidic scoop (TK40) and Minco immersion sampler.

Element, <i>i</i>	The average relation $\frac{[\%i]_{\text{MINCO}}}{[\%i]_{\text{TK40}}}$ for 8 samples	Standard Deviation
Si	1.005	0.009
Al	1.107	0.109
Ca	1.530	0.617
Fe	0.974	0.028
Ti	0.987	0.035
P	0.950	0.065

3.2 Sampling in the ladle during metal treatment - Immersion sampling

In steel and ironmaking it is common practice to employ immersion samplers to draw out representative samples of the liquid steel or hot metal bath for quick chemical analysis of the melt. Several commercial samplers are available on the market (Electro-Nite, Rescon, BSC, MINCO, etc.). In principle they are based on the same sampling technique, which is utilizing the ferrostatic pressure to fill the sampler. This type of sampler normally gives one disc or coin or a lollipop (a pet child has many names) of size typically Ø 25-35 mm and with a thickness from 3 to 25 mm. This lollipop or coin is used mainly for X-ray spectrometry. In addition to the coin-sample the sampler is designed to give one or more spherical pin samples with length from 30 to 50 mm and typically Ø 5 mm. The pin sample is employed for combustion analysis, for example analysing the C content. After several types of these samplers were evaluated, the MINCO immersion lance

sampler of the 40,000 series was found to be best suited for sampling of liquid ferrosilicon. Figure 3.3 shows in principle how the lance immersion sampler is used. This sampler has a side mounted tedge to avoid fluid metal to run out, which according to the supplier [1], was especially designed for sampling of hot metal and stainless steel.

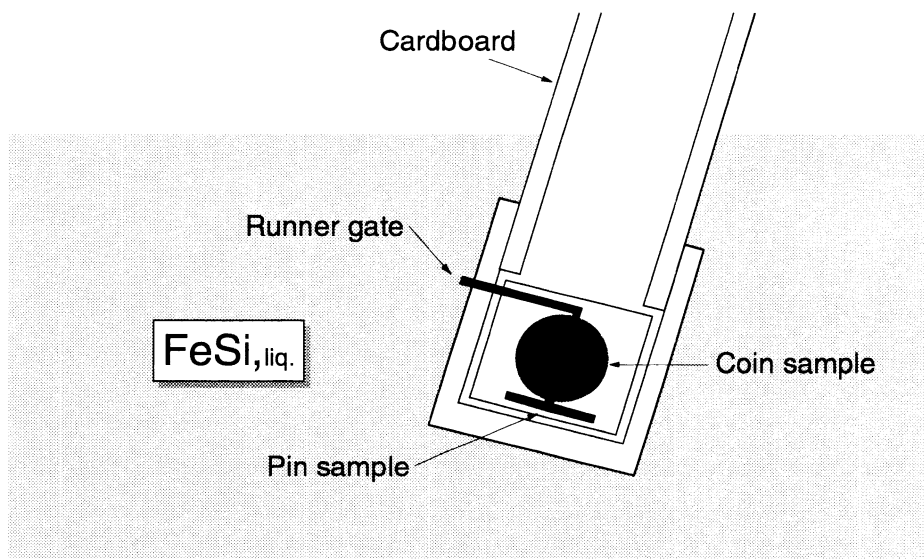


Figure 3.3: Principle drawing of the MINCO immersion lance sampler [2]

The sampler consists of two 3 mm thick steel plates mounted to a refractory mould as shown in figure 3.4. The lollipop or coin has a diameter of 35 mm and a thickness of 11.5 mm giving a 35-gram sample of FeSi75. The pin sample is about 50 mm long and 4.5 mm thick which gives a sample of 2 to 3 grams of FeSi75.

Different from in steelmaking, the pin sample taken of FeSi75 was not used directly for combustion analysis for analysing the carbon, but was ground to powder to get a homogeneous sample. Also for X-ray spectrometry the sample had to be ground to powder before it is pressed to a tablet and analysed.

$$\sigma_{C\text{-cont.}}^2 = \sigma_{\text{sampling}}^2 + \sigma_{\text{preparation}}^2 + \sigma_{\text{analysing}}^2 \quad (3.2)$$

From the manual for the carbon analyser, LECO CS 125, the accuracy of the carbon analysed is given as ± 2 ppm or $\pm 0.5\%$ whichever is greater when the carbon content is less than 0.1%. For carbon content $> 0.1\%$ the accuracy is ± 10 ppm or $\pm 0.5\%$ whichever is greater [3]. Since all samples in this work is analysed to be in the range 70 to 1000 ppm, the analysing accuracy, $\sigma_{\text{analysing}}$, is between 2 and 5 ppm. The sigma value for sample preparation, $\sigma_{\text{preparation}}$, is not known and is therefore merged with the sigma value for the sampling, σ_{sampling} , into one common sigma value, $\sigma_{\text{sampling + preparation}}$.

As mentioned in the introduction to this chapter, sampling of liquid (ferro)silicon with respect to carbon analyses is not common. Therefore, it was necessary to develop new methods as described above. The reliability of the sampling method employed had also to be examined. From one ladle of standard ferrosilicon we took four consecutive immersion samples with the MINCO sampler. Later three ladles with bottom stirring (compressed air) were examined, the first one by six consecutive immersion samples and the next by three samples. The results of these sampling including the mean value, \bar{X} , the standard deviation, σ and the coefficient of variation $V = \sigma/\bar{X}$ is presented in table 3.2.

TABLE 3.2: Standard deviation for MINCO Immersion sampling in FeSi75 (The sample No is equal to the Heat No stroke Furnace No at Elkem Thamshavn)

Sample No	2918-2	3121-1	3203-1	3205-1	Mean
Mean C-content, \bar{X}	594	217	307	265	
σ	60.85	17.9	36.96	25.32	
$V = \sigma/\bar{X}$	0.102	0.082	0.121	0.096	0.100

The above table shows that the sigma value for the carbon content in samples taken with the MINCO Immersion Sampler in ferrosilicon with 75 mass% Si in average is roughly 10% of the mean carbon content, i.e. $\sigma_{\text{C-cont.}} = \bar{X} \times 0.1013$. Since we know the sigma for analysing with LECO CS125, sigma for sampling and preparation can be calculated. Employing equation (3.2) gives

$$\sigma_{\text{sampling + preparation}}^2 = (\bar{X} \times 0.100)^2 - (\bar{X} \times 0.005)^2 \approx (\bar{X} \times 0.100)^2 \quad (3.3)$$

or

$$\sigma_{\text{sampling + preparation}} \approx \bar{X} \times 0.100 \quad (3.4)$$

This sigma value may be partly due to variation in the immersion depth. Therefore samples in three different depths in the stirred ladle were taken. Figure 3.6 shows the analysed carbon content in these samples drawn from 7, 34 and 74 cm under metal bath level.

Figure 3.6 indicates there is no difference in carbon content at different levels in the bath. However, one measurement of 420 ppm is far above the ppm range between 200 and 350 ppm. One explanation may be the presence of slag containing a high amount of SiC particles.

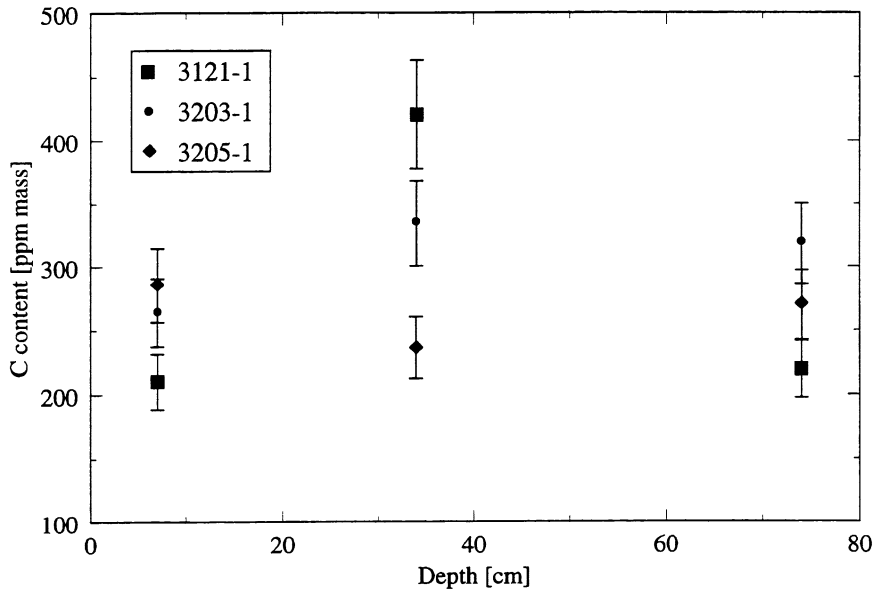


Figure 3.6: Variation in carbon content in samples drawn from different depth in the metal bath.

3.4 Inclusion filter sampling

Metallographic investigation of cast samples can be excessively time and labour consuming, especially when the concentration of inclusions is low. A filter sampler allows direct sampling of relatively large volumes of liquid metal. This method has been used in the aluminium industry since the late seventies [4], but - has to our knowledge - never been adapted to ferroalloys. Since ferrosilicon (75 mass% Si) typically has a tapping temperature between 1500 - 1700 °C compared with 700 °C for aluminium, it was necessary to develop sampling equipment that would withstand temperatures up to 1700 °C. The sampler is described in figure 3.7 and consists of a filter unit (a filter holder with a graphite filter) attached to a canister where the filtered metal is collected.

The initial trials with the sampler in ferrosilicon were described in a paper presented at 7th International Ferroalloy Conference, Trondheim, June 1995 [5]. Here the method will be discussed further and some additional results from filter sampling of ferrosilicon are presented. As mentioned in [5] ferrosilicon from production runs at Elkem Thamshavn were sampled. One of the challenges was to heat the sampler sufficiently in order to avoid freezing of metal in the narrow channel going from underneath the filter and to the canister.

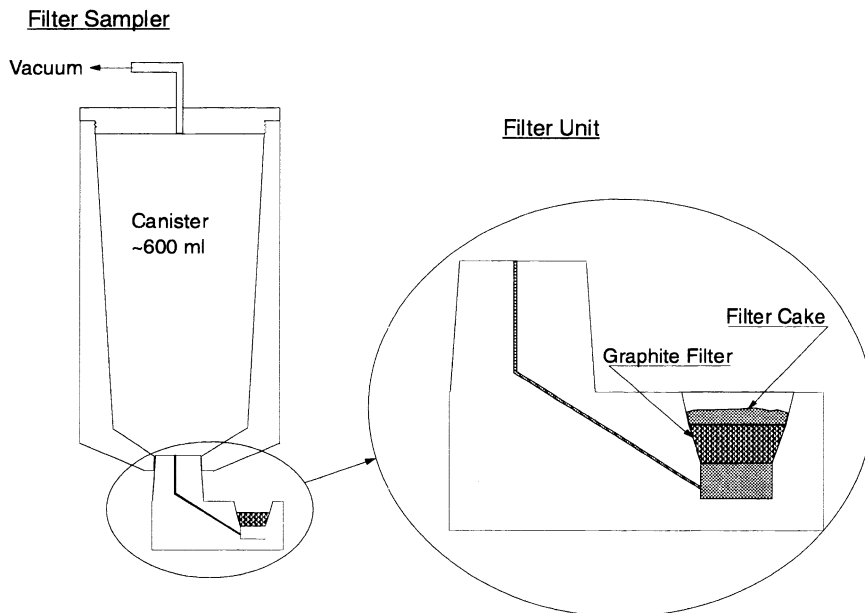


Figure 3.1: The Graphite Filter Sampler

This problem was solved by heating the sampler in the melt itself. To avoid contact between melt and filter before it was heated, nitrogen was blown down through the canister, through the channel and up the filter. After approximately 30 seconds the filter sampler was red-hot and the valve was opened to the vacuum system, and the nitrogen flow was shut off. After 2 - 3 minutes with suction the canister was filled and the sampler lifted out of the melt. The sampler unit was then cooled with compressed nitrogen immediately after it was drawn out of the metal bath.

Figure 3.8 shows the experimental layout of the first stage of filter sampling of

standard ferrosilicon from furnace number 2 at Elkem Thamshavn.

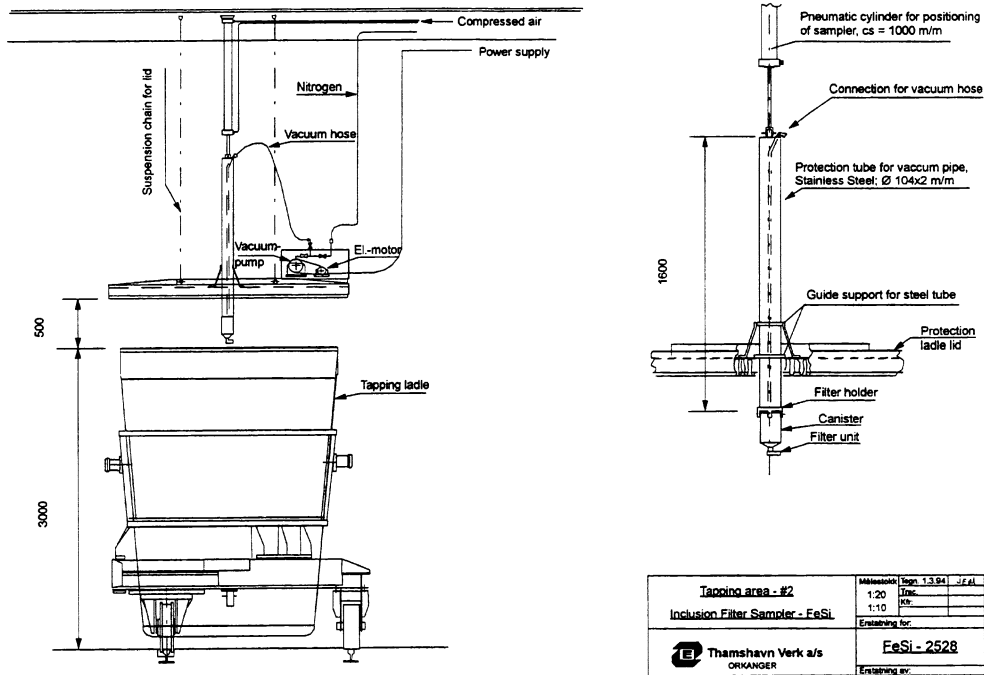


Figure 3.8: Experimental layout for vacuum filter sampling of ferrosilicon at Elkem Thamshavn

The experimental equipment shown in figure 3.8 was stationary and could only be employed for metal from furnace number 2. When we later wanted to extend the filter sampling to include refined ferrosilicon, the equipment was made mobile. Thus the equipment was accessible also for other plants.

One of the problems when taking filter samples is to keep the collected metal inside the canister and to avoid any backflow that could result in loss of particles at the inlet of the filter. This was solved by retaining the suction. However, to avoid sucking metal from the filter cake into the canister, the underpressure had to be tuned to a level equal to the pressure from the metal bath in the canister. It was impossible to determine exactly how much metal there was in the canister. It was therefore difficult to set the correct underpressure until the metal had been cooled sufficiently.

3.4.1 Automatic image analysis

Metallographical examination of sampling filters based on light microscopy and image analyses has been applied successfully on aluminium sampling filters [6,7] and on magnesium sampling filters [8]. The same equipment and procedures have here been adapted on sampling filters for ferrosilicon. Frisvold [6] and Bakke [8] have described the method in detail. The sampling filter is sliced in half along the melt flow direction. Measurements are made in rows at different depths through the sampling filter, each row containing a number of fields, as illustrated by figure 3.9.

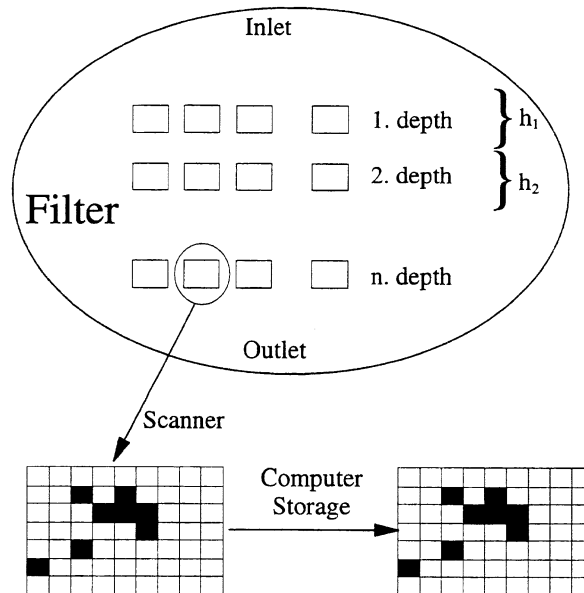


Figure 3.9: Vertical scan through sampling filter. The image is transferred to the computer memory.

The digital image of the inclusions in the computer memory is further processed by an image analysis program where inclusion sizes are determined by inscribing hexagons.

The discrete absolute size distribution per unit area and depth $n_A(d_i, z_j)$ and the average melt fraction ε_j at depth z_j ($1 \leq j \leq J$) are given. Each $n_A(d_i, z_j)$ is assumed to be valid over a vertical distance h_j defined as the half distance between depth z_{j-1} and z_j plus the half distance between the depths z_j and z_{j+1} , see figure 3.9. A start and end position has to be determined for the depths z_1 and z_j . h_1 can be defined as twice the half distance between z_1 and z_2 , while the end position is defined as twice the half distance between z_{j-1} and z_j . The total number of particles per melt area for class d_i in the entire filter is then

$$N_A(d_i) = \sum_{j=1}^J n_A(d_i, z_j) h_j \varepsilon_j \quad (3.5)$$

Although inclusions may have practically any shape, it is assumed that they are spherical. When observing a poly-disperse system from an intersecting plane, there is a finite probability that the observed sphere sections, apparently belonging to a size class i , may be sections of any spheres of size i up to size I . Therefore we have to take into account that some of the observed sections can come from larger spheres. In accordance with Saltykov's theory [8,9], the size distribution per unit volume is

$$N_V(d_i) = \frac{1}{\Delta} \left\{ \alpha_{i,i} N_A(d_i) - \sum_{k=i+1}^I \alpha_{i,k} N_A(d_k) \right\} \quad (3.6)$$

where Δ is the width of the size classes and $\alpha_{i,i}$ are the weights due to Saltykov. Saltykov's table of weights is given in Appendix B.

The concentration of particles on volume basis per unit melt is

$$c_V = \frac{A_f \rho_{\text{melt}}}{m_{\text{melt}}} \frac{\pi}{6} \sum_i d_i^3 N_V(d_i) \rho_p \quad (3.7)$$

when the cross sectional filter area A_f is taken to be the same at all depths. The total volume of melt gone through the filter is $V_{\text{melt}} = m_{\text{melt}} / \rho_{\text{melt}}$. The concentration of particles on mass basis is

$$c_{\text{melt}} = c_v \times \frac{\rho_p}{\rho_{\text{melt}}} \quad (3.8)$$

For SiC-particles in ferrosilicon with 75 mass% Si we have $\rho_p \approx \rho_{\text{melt}}$, cf. chapter 2.4, giving $c_v \approx c_{\text{melt}}$.

Note that equation (3.7) is correct only if all the inclusions are captured.

3.4.2 Filter sampling of ferrosilicon from production runs.

As mentioned above, results of the measurement of the number size distribution of ferrosilicon with 75 mass% Si, $N_v(d_i)$, were for the first time presented at Infacon 7 [5], see figure 3.10. This investigation was followed up by filter sampling of another three heats of standard ferrosilicon. In figure 3.11 the number size distributions for these three heats are given and it is seen that the results from [5] are repeated with almost the same size distribution. The points in parenthesis have higher statistical uncertainty.

In table 3.3 the mean diameter and the mean inclusion concentration for each heat are given. The values in column 6, named "Equiv. C-content", is the amount of carbon filtered as inclusions when assuming that all inclusions are spherical and consist of SiC. Column 7 gives the carbon content in the filtered metal, whereas the carbon in the metal bath is presented in the last column.

It is seen that there is a variation in the amount of particles trapped on and in the filter. The amount of inclusions found is also lower than what would be expected from the carbon content found in this type of ferrosilicon.

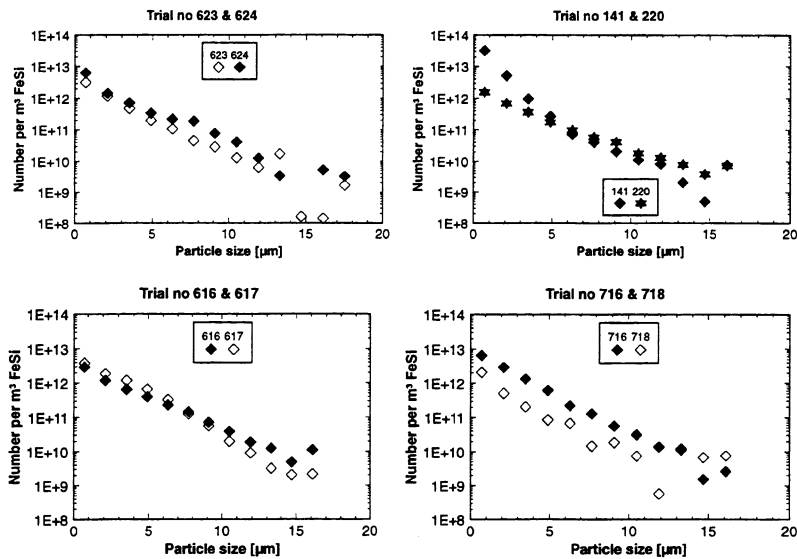


Figure 3.10: Inclusion number size distribution in FeSi75 from production run at Elkem Thamshavn; Filled points indicate heats with no stirring. Empty points are with bottom stirring [5].

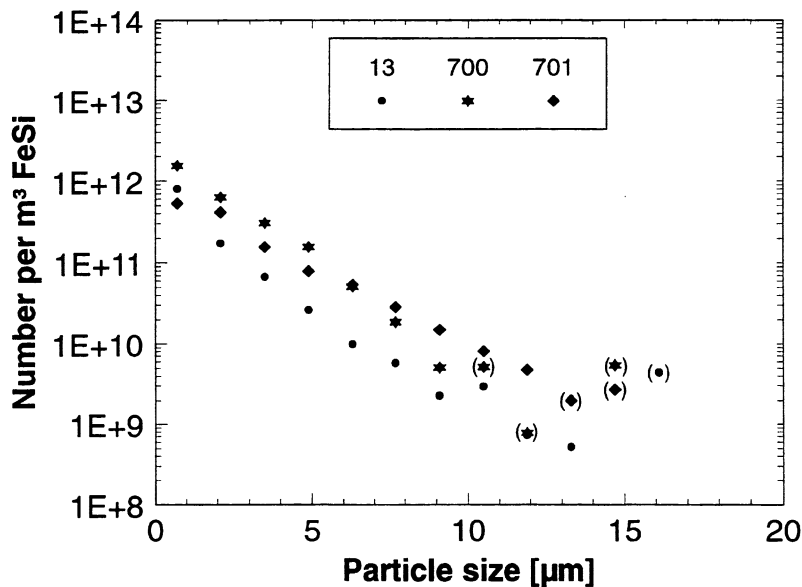


Figure 3.11: Inclusion number size distribution in FeSi75 of three different heats from production run at Elkem Thamshavn. Numbers in parenthesis have higher statistical uncertainty.

TABLE 3.3: Inclusion concentration on volume basis and mean particle diameter in standard FeSi75 measured from filter sampling. The equivalent C content (column 7) is calculated assuming that all particles are SiC. An error in the calculation program has given a correction for the heats presented in [5]. Numbers that have been corrected are marked with *).

1	2	3	4	5	6	7	8
Heat no	Amount of metal sampled, m_{melt} [g]	Mean inclusion diameter [μm]	Inclusion conc. on vol. basis [ppm]	Melt bath temp. [$^{\circ}\text{C}$]	Equiv. C-content ¹⁾ [ppm]	C in filtered metal	C in metal bath, Minco
623-2	494	3.4	103*		31	137	442
624-2	389	3.5*	205*		61		
141-2	384	1.9	127*		38		
220-2	782	4.2*	118*		35		
616-2	1524	4.2	153*		45	82	
617-2	1139	3.6	135*		40	130	
716-2	1498	3.1*	136*		41	210	
718-2	1055	2.8	24*		7	170	299
13-2	1052	3.2	19	1450	6		
700-2	154	3.2	45	1509	14	122	349
701-2	1905	4.1	46	1519	14	87	482
Mean		3.4	101		30	134	393

¹⁾ Assuming that all inclusions are SiC

The sum of column 6 and column 7 should be equal to the carbon content in the metal bath (column 8). However, as can be seen from table 3.3 the value in column 8 is larger. This indicates that some of the SiC particles collected in the cake are lost during the sampling and the following preparation. As mentioned previously one of the problems was to set the correct underpressure to avoid metal to flow back from the canister that could result in loss of particles at the inlet of the filter.

The melt bath temperature was in the range 1450 - 1550 °C during the filter sampling, which corresponds to a carbon solubility from 60 to 124 ppm in FeSi75 with 1 mass% Al, cf. eqn (8) in chapter 2.2. The amount of carbon found in the metal collected in the canister, the values in column 7, varied from 80 to 210 ppm and are somewhat higher than the solubility level. The explanation could be that some small SiC particles are sucked through the filter. Also, contamination from the graphite canister cannot be excluded in spite of being rapidly cooled with nitrogen from a gas cylinder.

In chapter 1 it was shown that low aluminium (refined) FeSi75 has a lower content of carbon than standard grade ferrosilicon. It was therefore of interest to see if this could be reflected in the number of SiC particles in the melt. Six heats of refined FeSi75 were sampled with the filter sampler described above. Sampling of refined ferrosilicon was more difficult for two reasons. There were more problems with flow of metal back from the canister when the underpressure was too low. Too much suction resulted in emptying the metal layer above the filter. Another problem with the low aluminium ferrosilicon was that some slag left after deslagging could be sucked into the filter and clog it. Of the 6 samples taken only three could be analysed. In table 3.4, the concentration of particles on volume basis, c_v , and the mean particle diameter is given along with the equivalent C-content in the melt (see definition in connection with table 3.3) and the carbon content in the filtered metal for these three heats. The solubility of carbon in FeSi75 with 0.1 mass% Al is 40 ppm at the 1411 °C, whereas the solubility at 1490 °C is 75 ppm. The values in column 7 in table 3.4 should reflect the solubility figures for the actual melt. For heat no 923-1 and heat no 216-1 the measured value of carbon is close to the solubility value, whereas there is a great discrepancy for heat no 666-1.

The number size distributions for these three heats with refined ferrosilicon are given in figure 3.12.

TABLE 3.4: Inclusion concentration on volume basis and mean particle diameter in refined ferrosilicon (low Al FeSi75) measured from filter sampling. The equivalent C content (column 7) is calculated assuming that all particles are SiC.

1	2	3	4	5	6	7	8
Heat no	Amount of metal sampled, m_{melt} [g]	Mean inclusion diameter [μm]	Inclusion conc. on vol. basis [ppm]	Melt bath temp. [$^{\circ}\text{C}$]	Equiv. C-content ¹⁾ [ppm]	C in filtered metal	C in metal bath, Minco
666-1	629	3.1	9	<1460	3	180	150
923-1	877	3.1	7	<1490	2	71	78
216-1	1301	2.6	19	1411	6	67	258
Mean		2.9	11		4	106	198

¹⁾ Assuming that all inclusions are SiC

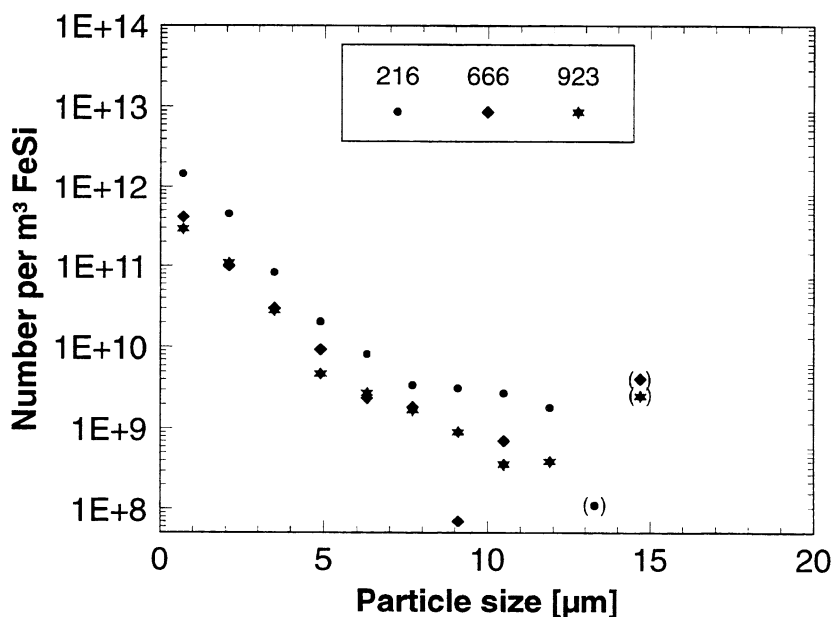


Figure 3.12: Inclusion number size distribution in low Al FeSi75 in three different heats from production runs at Elkem Thamshavn. Number in parenthesis have higher statistical uncertainty.

The numbers in table 3.4 are on the whole lower than the corresponding figures for standard ferrosilicon. The average particle diameter is reduced from 3.4 to 2.9 μm and the inclusions concentration for refined is on average reduced by a factor of ten. This difference is further demonstrated in figure 3.13 where the number size distribution for one typical heat of refined and one typical heat of standard ferrosilicon is compared.

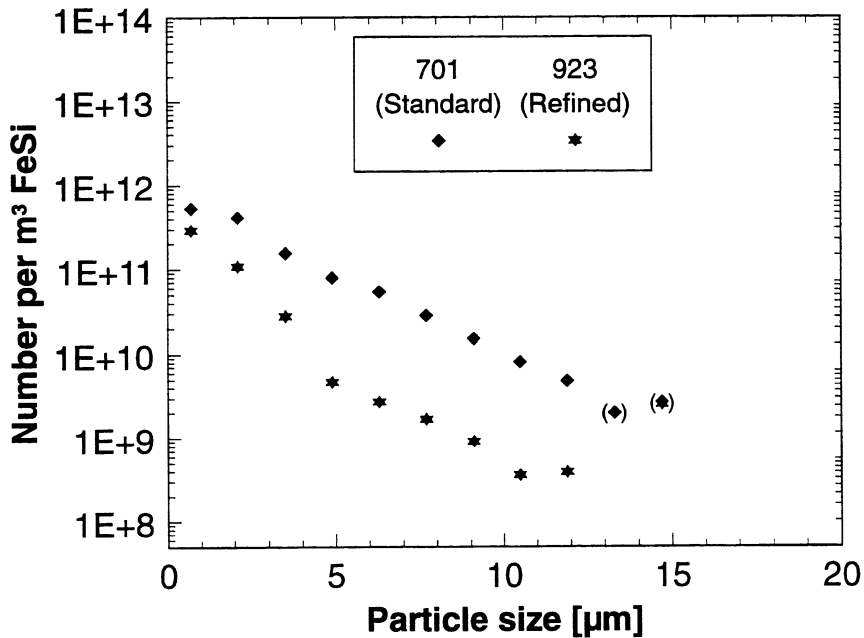


Figure 3.13: Comparison of the number size distribution in low Al FeSi75 (heat no 923) and Standard FeSi75 (heat no 701). Number in parenthesis have higher statistical uncertainty.

References

1. Dodds, M., Minco Sampling Techniques (UK) Ltd., Private Communication
2. Product Pamphlet from Midwest Instrument Company, Inc./Minco Sampling Techniques (UK) Ltd.
3. Instruction Manual for LECO CS125 Combustion Analyzer, LECO Corp.
4. Bates, D.A. and Hutter, L.C., "An evaluation of aluminum filtering systems using a vacuum-filtration sampling device.", *Light Metals* (1981) pp. 707-721
5. Klevan, O. S. and Engh, T. A., "Dissolved Impurities and Inclusions in FeSi and Si, Development of a Filter Sampler", *Proceedings from INFACON 7*, Trondheim (1995) p. 43
6. Frisvold, F., "Filtration of aluminium - theory, mechanisms, and experiments.", *Dr.ing thesis*, (1990), pp.90-95, NTH, Trondheim
7. Bathen, E., "Investigation of inclusions in aluminium melts by image analysis." *Proceedings of the Int. Seminar on Refining and Alloying of Liquid Aluminium and Ferro-Alloys*, (1985), NTH, Trondheim, Norway, pp. 175-191
8. Bakke, P. "Measurement and removal of inclusions and hydrogen in Magnesium", *Dr.ing thesis*, NTH (1992) p. 103
9. R. T. DeHoff and F. N. Rhines *Quantitative Microscopy*, McGraw-Hill, New York (1968)

4. Removal of C from Silicon and Ferrosilicon

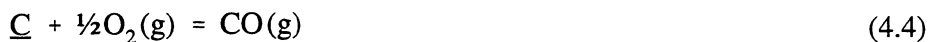
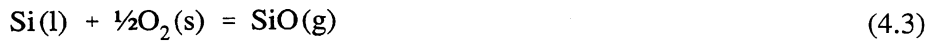
Carbon is present in liquid silicon and ferrosilicon as silicon-carbide and dissolved carbon. The amount of carbides depends on furnace operation and the temperature of tapped metal. The amount of dissolved carbon in the metal is also dependant on the temperature in addition to the chemical composition. In pure silicon and pure FeSi75 the solubility in equilibrium with SiC is given by the following expressions [1,2]

$$\log[\%C]_{\text{Si(l)}} = 3.53 - \frac{9,736}{T} \quad [\text{mass}\%] \quad (4.1)$$

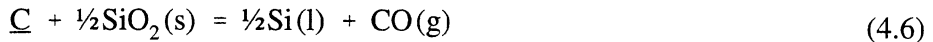
$$\log[\%C]_{\text{FeSi75(l)}} = 3.5 - \frac{10,003}{T} \quad [\text{mass}\%] \quad (4.2)$$

4.1 Decarburization of silicon and ferrosilicon melts

When oxygen containing gas is injected into liquid silicon, first SiO(g) should be formed and then solid silica [3]. The silica can then react further with dissolved carbon. When C is less than given by eqns. (4.1) and (4.2), the following reactions occur:



These three competitive reactions give the overall reaction that can be written as



with

$$\ln K_{4.6} = \ln \frac{a_{\text{Si}}^{1/2} p_{\text{CO}}}{a_{\text{C}} a_{\text{SiO}_2}^{1/2}} = - \frac{35,069}{T} + 18.32 \quad (4.7)$$

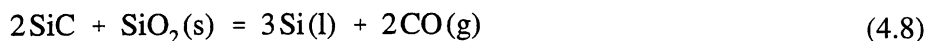
where a_{Si} is the activity of silicon in the metal bath (for a melt of pure silicon it is unity and for ferrosilicon with 75 mass% Si it is 0.82), p_{CO} is the partial pressure of CO in the gas phase, a_{C} is the activity of carbon in the metal bath, and a_{SiO_2} is the silica activity. The latter is also unity in a melt of silicon or ferrosilicon with no other impurities than carbon that react with oxygen. Thermochemical data is taken from [1,4]

From eqn (4.7) it is seen that decarburization according to reaction (4.6) is favoured by low silicon activity and a high carbon activity in the metal, a high silica activity in the slag, and a low partial pressure of CO in the gas phase. It is also seen from the expression in eqn (4.7) that the oxidation of carbon is enhanced by a high temperature.

The relation $p_{\text{CO}}/a_{\text{C}}$ is 0.67 at 1600 °C and unity at 1645 °C for the case of pure silicon metal. With 25 mass% iron and 75 mass% silicon in the melt the same relation is 0.74 at 1600 °C and unity at 1635 °C.

Carbon monoxide has to diffuse into the bubbles and then be transported by these bubbles to the surface of the metal bath. If the silica formed is a solid and dense layer around the bubbles, the diffusion through this silica layer can be a slow process. This assumption and its effect on the decarburization rate will be discussed later in this chapter.

At total carbon contents above the levels given by eqns. (4.1) and (4.2) a solid - solid reaction between silicon-carbide and silica could be possible:



$$\ln K_{4.8} = \ln \frac{a_{\text{Si}}^3 \times p_{\text{CO}}^2}{a_{\text{SiC}}^2 \times a_{\text{SiO}_2}} = - \frac{110,939}{T} + 50.67 \quad (4.9)$$

With pure silicon the activities in eqn. (4.9) are all unity giving a partial pressure of carbon monoxide below 0.10 atm up to 1725 °C. This means there would be a very limited reduction of SiC by SiO₂. Kinetically such a solid-solid reaction should proceed very slowly.

4.1.1 The rate of decarburization

Consider the change in gas composition as bubbles ascend through the melt. Figure 4.1 shows a horizontal section of the refining ladle. It is assumed that CO within a bubble is completely mixed. As mentioned SiO should be formed initially. This period is disregarded in the following.

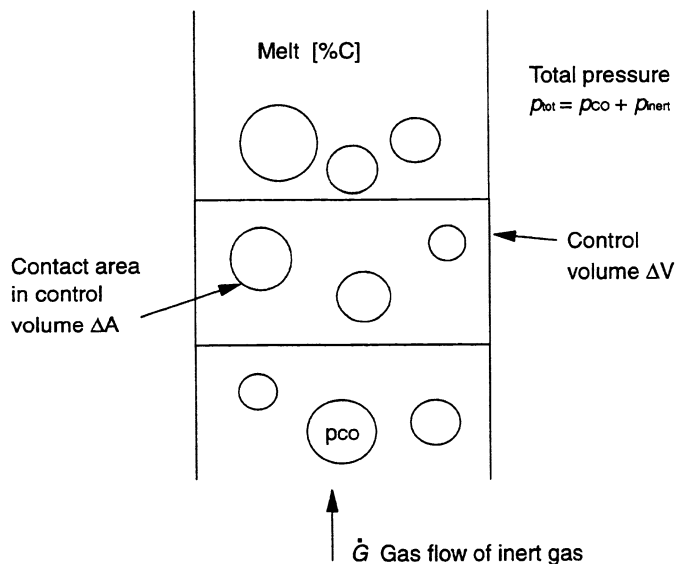


Figure 4.1: Gas purging control volume

A mass balance for the control volume in figure 4.1 is then:

Moles of CO transferred to the bubbles per second in the control volume $\Delta V =$
Increase of flow of CO carried by the bubbles through the control volume ΔV

or

$$\frac{\Delta A_b k_C \rho_{\text{melt}}}{100 M_C} ([\% C] - [\% C]_e) = \dot{G}_{\text{inert}} \Delta \left(\frac{p_{\text{CO}}}{p_{\text{inert}}} \right) \quad (4.10)$$

The partial pressure of inert gas is $p_{\text{inert}} = p_{\text{tot}} - p_{\text{SiO}} - p_{\text{CO}}$. The partial pressure of SiO(g), p_{SiO} , may be calculated from the equilibrium given by eqn. (4.5). It is about 0.1 bar at 1600 °C in pure silicon and may be simplest taken into account by reducing the p_{tot} . For decarburization by gas purging in an open ladle, the effect of SiO formation should primarily be the loss of silicon and oxygen. When purging at low pressures, the use of an average total pressure is erroneous. In this case SiO formation cannot be treated simply by subtracting p_{SiO} from a constant value of p_{tot} .

The partial pressure of CO is given by eqn. (4.4) and the hypothetical concentration of carbon is

$$[\% C]_e = \frac{a_{\text{Si}}^{1/2} p_{\text{CO}}}{a_{\text{SiO}_2}^{1/2} f_C K_{4.5}} = B \times p_{\text{CO}} \quad (4.11)$$

Combination of (4.10) and (4.11) gives

$$\frac{k_C \rho_{\text{melt}} dA_b}{100 M_C \dot{G}_{\text{inert}}} = \frac{1}{[\% C] - B \times p_{\text{CO}}} \times d \left(\frac{p_{\text{CO}}}{p_{\text{tot}} - p_{\text{CO}}} \right) \quad (4.12)$$

Assuming that the total pressure, $p_{\text{tot}} = 1/2(2p_{\text{atm}} + \rho_{\text{melt}} gH)$, is constant through the

ladle gives

$$\frac{k_C \rho_{\text{melt}} dA_b}{100 M_C \dot{G}_{\text{inert}}} = \frac{dp_{\text{CO}} \times (p_{\text{tot}} - p_{\text{CO}}) + p_{\text{CO}} \times dp_{\text{CO}}}{([\%C] - B \times p_{\text{CO}}) \times (p_{\text{tot}} - p_{\text{CO}})^2} \quad (4.13)$$

and then

$$\int_0^{A_b} \frac{k_C \rho_{\text{melt}}}{100 M_C \dot{G}_{\text{inert}}} dA_b = \int_0^{p_{\text{CO}}^0} \frac{p_{\text{tot}} dp_{\text{CO}}}{([\%C] - B \times p_{\text{CO}}) \times (p_{\text{tot}} - p_{\text{CO}})^2} \quad (4.14)$$

integrating from zero to A_b on the left side and from zero to the outlet pressure of carbon monoxide, p_{CO}^0 , on the right side gives

$$\frac{k_C \rho_{\text{melt}} A_b}{100 M_C \dot{G}_{\text{inert}}} = \frac{p_{\text{tot}}}{[\%C] - B p_{\text{tot}}} \times \left\{ \frac{p_{\text{CO}}^0}{p_{\text{tot}} (p_{\text{tot}} - p_{\text{CO}}^0)} - \frac{B}{[\%C] - B p_{\text{tot}}} \ln \frac{p_{\text{tot}} ([\%C] - B p_{\text{CO}}^0)}{[\%C] (p_{\text{tot}} - p_{\text{CO}}^0)} \right\} \quad (4.15)$$

introducing a dimensionless contact area, $\phi_A' = \phi_A B p_{\text{tot}}$, where

$$\phi_A = \frac{A_b k_C \rho_{\text{melt}}}{100 M_C \dot{G}_{\text{inert}}} \quad (4.16)$$

and the dimensionless variable z

$$z = \frac{B p_{\text{tot}}}{[\%C] - B p_{\text{tot}}} \quad (4.17)$$

Eqn (4.15) can now be written as

$$\phi_A' = z \times \left\{ \frac{p_{CO}^0}{p_{tot} - p_{CO}^0} - z \ln \frac{p_{tot}([\%C] - B p_{CO}^0)}{[\%C](p_{tot} - p_{CO}^0)} \right\} \quad (4.18)$$

The dimensionless area, ϕ_A' , increases with increasing contact area i.e. with small bubbles, and it increases with decreasing gas flow. ϕ_A' will also increase with increasing B or decreasing equilibrium constant.

Eqn (4.18) can be written as

$$\frac{\phi_A'}{z} = \frac{p}{1-p} - z \ln \frac{1 - p B p_{tot} / [\%C]}{1-p} \quad (4.19)$$

where $p = p_{CO}^0 / p_{tot}$.

A mass balance for the reactor gives:

reduction of carbon content per unit time = flow of carbon-monoxide out of the reactor.

$$\dot{G}_{CO} = - \frac{V \rho_{melt}}{M_C 100} \frac{d[\%C]}{dt} = \dot{G}_{inert} \frac{p_{CO}^0}{p_{tot} - p_{CO}^0} \quad (4.20)$$

this equation can then be written as

$$- \frac{V \rho_{melt}}{M_C 100 \dot{G}_{inert}} \frac{d[\%C]}{dt} = -A \frac{d[\%C]}{dt} = \frac{p}{1-p} \quad (4.21)$$

where $A = \frac{V \rho_{melt}}{M_C 100 \dot{G}_{inert}}$.

From this one obtains

$$p = -\frac{A \times \left(\frac{d[\%C]}{dt} \right)}{1 - A \times \left(\frac{d[\%C]}{dt} \right)} \quad \text{or} \quad 1 - p = \frac{1}{1 - A \times \left(\frac{d[\%C]}{dt} \right)} \quad (4.22)$$

the expressions for $p/(1-p)$, p and for $1-p$ are now inserted in eqn (4.19) giving

$$\frac{\phi_A'}{z} = -A \frac{d[\%C]}{dt} - z \ln \left\{ 1 - A \frac{d[\%C]}{dt} \left(1 - \frac{B p_{\text{tot}}}{[\%C]} \right) \right\} \quad (4.23)$$

By reintroducing z from eqn. (4.17) we get

$$\begin{aligned} \frac{\phi_A'}{B p_{\text{tot}}} ([\%C] - B p_{\text{tot}}) = \\ -A \frac{d[\%C]}{dt} - \frac{B p_{\text{tot}}}{([\%C] - B p_{\text{tot}})} \ln \left\{ 1 - A \frac{d[\%C]}{dt} \left(1 - \frac{B p_{\text{tot}}}{[\%C]} \right) \right\} \end{aligned} \quad (4.24)$$

since $\phi_A' / B p_{\text{tot}} = \phi_A$ we get

$$\begin{aligned} \phi_A ([\%C] - B p_{\text{tot}}) = \\ -A \frac{d[\%C]}{dt} - \frac{B p_{\text{tot}}}{([\%C] - B p_{\text{tot}})} \ln \left\{ 1 - A \frac{d[\%C]}{dt} \left(1 - \frac{B p_{\text{tot}}}{[\%C]} \right) \right\} \end{aligned} \quad (4.25)$$

or taking the anti-logarithm:

$$\begin{aligned} \frac{A([\%C] - B p_{\text{tot}}) \frac{d[\%C]}{dt}}{[\%C]} - 1 \\ + \exp \left\{ -\frac{A([\%C] - B p_{\text{tot}}) \frac{d[\%C]}{dt}}{B p_{\text{tot}}} - \frac{\phi_A}{B p_{\text{tot}}} ([\%C] - B p_{\text{tot}}) \right\} = 0 \end{aligned} \quad (4.26)$$

Equation (4.25) and (4.26) are difficult (if possible) to solve analytically and have therefore to be solved by employing a numerical method.

Two special cases, which can be solved analytically, are 1) when the gas reaches equilibrium with the carbon in the surrounding melt and 2) when we are far away from equilibrium.

1. Equilibrium between the CO-gas and the carbon in the liquid silicon means

$$p_{\text{CO}}^0 = \frac{[\%C]}{B} \quad (4.27)$$

equation (4.20) can then be written

$$-\frac{V\rho_{\text{melt}}}{M_C 100} \frac{d[\%C]}{dt} = \dot{G}_{\text{inert}} \times \frac{1}{\frac{Bp_{\text{tot}}}{[\%C]} - 1} \quad (4.28)$$

or

$$\int_{[\%C]_{\text{in}}}^{[\%C]} \left(\frac{Bp_{\text{tot}}}{[\%C]} - 1 \right) d[\%C] = - \int_0^t \dot{G}_{\text{inert}} \frac{M_C 100}{V\rho_{\text{melt}}} dt \quad (4.29)$$

integrated from $t = 0$ to time t gives then

$$(Bp_{\text{tot}}) \times \ln \frac{[\%C]}{[\%C]_{\text{in}}} - [\%C] + [\%C]_{\text{in}} = -1.49 \times 10^{-2} \frac{\dot{Q}_{\text{inert}}}{V\rho_{\text{melt}}} t \quad (4.30)$$

where the gas flow, \dot{Q}_{inert} , is given in Nm^3/h , the volume of the melt, V , in m^3 and the density of the silicon or ferrosilicon has the unit kg/m^3 . This gives the maximum possible decarburization rate.

2. In the case where the contact area, A_b , is small so that we are far away from equilibrium, we may set

$$[\%C]_e = Bp_{CO} = 0 \quad (4.31)$$

equation (4.14) can then be simplified and written

$$\int_0^{A_b} \frac{k_C \rho_{\text{melt}}}{100 M_C \dot{G}_{\text{inert}}} dA_b = \int_0^{P_{CO}^\circ} \frac{P_{\text{tot}} dp_{CO}}{([\%C]) \times (p_{\text{tot}} - p_{CO})^2} \quad (4.32)$$

Integrating from zero to A_b on the left side and from zero to the outlet pressure of carbon monoxide, p_{CO}° , on the right side gives

$$\frac{k_C \rho_{\text{melt}} A_b}{100 M_C \dot{G}_{\text{inert}}} = \frac{P_{CO}^\circ}{([\%C]) \times (p_{\text{tot}} - p_{CO}^\circ)} \quad (4.33)$$

combined with the mass balance in eqn (4.20) this gives

$$\frac{k_C \rho_{\text{melt}} A_b}{100 M_C} \times [\%C] = - \frac{V \rho_{\text{melt}}}{M_C 100} \frac{d[\%C]}{dt} \quad (4.34)$$

which can be reduced to the following familiar expression

$$\frac{d[\%C]}{[\%C]} = - \frac{k_C A_b}{V} dt \quad (4.35)$$

or

$$\frac{[\%C]}{[\%C]_{\text{in}}} = \exp\left(-\frac{k_C A_b}{V} \times t\right) \quad (4.36)$$

This decreasing exponential solution may look attractive. However due to the low values of the contact area, it drops very slowly.

The two extreme cases treated can be solved analytically, and may now be used to control the numerical model describing equation (4.26)

4.1.2 Numerical solution of the decarburization rate

As mentioned above, equation (4.26) has to be solved by numerical calculation and here we have employed the software package Powersim™[5] to simulate the decarburization rate. The discretization of eqn. (4.26) and the simulation setup in Powersim is described in Appendix C. The model requires the following variables: the melt temperature, the melt volume, the height of the metal bath above the injection point, type of alloy (Si-metal or ferrosilicon), the flow rate of inert gas, the bubble size and the mass transfer coefficient. The contact area or total bubble area, A_b , is given as

$$A_b = \frac{\dot{Q}}{3600} \times \frac{(T+273.15)}{T} \times \frac{6}{d_b} \times \tau_b \quad (4.37)$$

where the residence time for the bubbles, $\tau_b = H/u_b$. H is the vertical distance from the gas inlet to the bath surface which is equal to the height of the metal bath in most cases. The expansion of bubbles due to a decreasing pressure is not taken into account. At atmospheric pressure and in ladles that are not too deep, one may use an average total pressure. The velocity of the bubbles, u_b , is a function of the bubble size, d_b and the physical properties of the liquid. The relation between bubble size and bubble velocity in liquid silicon and FeSi75 is given in Appendix D.

Use of the model is here exemplified by decarburization of liquid silicon metal. In 1993 P. Bakke carried out five experiments at Elkem Research Centre in Kristiansand where liquid silicon was decarburized [6]. In these experiments

silicon metal was decarburized with a gas mixture of air and argon. The mass of melt was approximate 7 kg, and the total amount of gas injected was 10 NI/min. Gas mixture varied from 100% air to 50/50 air and argon. The gas was introduced through a Cu-tube with inner diameter, d_i , of 2 mm.

The five experiments in [6], in the following designated *Run 1 - Run 5*, varied in initial carbon content. Possibly due to poor mixing, the carbon content in the melt increased somewhat initially. The simulation is chosen to start at the time with the highest carbon content. One of the unknown parameters in the model is the bubble size. In the simulations the bubble diameter employed is calculated from formulas found in the literature presented in table 4.1. Calculated size of bubbles for a typical experiment performed by P. Bakke [6] is also given in table 4.1. Here we have not distinguished between inner and an outer diameter and this is one reason that the formula of Okumura et al., eqn (3) in the table, give a lower bubble diameter compared with equation (1). The gas flow rate is $\dot{Q}_g = 1.5 \times 10^{-4} \text{ Nm}^3/\text{s}$ and the density gas is, $\rho_g = 1.42 \text{ kg/m}^3$ (50/50 mixture of Ar and air). The physical properties of the melt at 1600 °C are taken from chapter 2.3. The bubbles are assumed to reach the bath temperature and expand with a factor equal to $\left(\frac{T_{\text{melt}}}{273\text{K}}\right)^{1/3}$. Some authors [7] state that the gas is most likely heated at the nozzle orifice and therefore expands before entering the metal bath, but as seen from the equations in table 4.1, we get almost the same result for the bubble size when the gas flow rate is high ($> 3 \times 10^{-5} \text{ Nm}^3/\text{s}$).

TABLE 4.1: Formula for equivalent gas bubble diameter. Gas bubble diameter in liquid silicon at 1600 °C where the gas is 50/50 mixture of Ar and air.

Author(s)	Ref.	Formula	d_b in Si(l) [mm]
F. Oeters / J. K. Brimacombe et al./ M. Sano and K. Mori	[7]/ [8]/ [9]	$d_b = \left\{ \frac{3\sigma d_i}{\rho g} + \left[\frac{9\sigma^2 d_i^2}{\rho^2 g^2} + K \frac{\dot{Q}_g^2 d_i}{g} \right]^{1/2} \right\}^{1/3} \quad (1)$	36
T. A. Engh and M. Nilmani	[10]	$d_b = \left\{ \frac{3\dot{Q}_g r_o^{0.5}}{\pi g^{0.5} (\rho_g/\rho)^{1/4}} \right\}^{1/3} \quad (2)$	40
K. Okumura, M. Ban, M. Hirasawa, M. Sano and K. Mori	[11]	$d_b = \left\{ \frac{6\sigma d_{no}^2}{\rho g} + 0.0242 \left(\dot{Q}_g^2 d_{no} \right)^{0.867} \right\}^{1/6} \quad (3)$	33

$2r_o = d_i = 2 \times 10^{-3}$ m. Physical properties of the melt is from chapter 2.3.

Figure 4.2 - figure 4.6 shows the results for *Run 1 - Run 5* from [6] with the corresponding Powersim simulations. The simulation marked, *Simulation 1,2,3,4,5* is with mass transfer coefficient $k_c = 1 \times 10^{-4}$ m/s, which is typical for mass transfer to bubbles [12]. For the simulation designated with a *b* a mass transfer coefficient of $k_c = 5 \times 10^{-6}$ m/s is used. The bubble diameter is calculated from equation (1) in table 4.1. All other variables employed in the model, such as gas flow, amount of metal and temperature are the same as in the experiments and presented in table 4.2.

The simulations with $k_c = 5 \times 10^{-6}$ m/s agree with the experimental results except for *Run 1*. This run was the first run with a new crucible lining and this may probably affect the decarburization mechanism.

TABLE 4.2: Experimental input data from [6] for the Powersim simulations in figure 4.2-4.6. \dot{Q}_{inert} is $\dot{Q}_{\text{Ar}} + \dot{Q}_{\text{Nitrogen from air}}$. It is assumed that all oxygen in the air reacts with silicon to silica.

Run no	V_{melt} [dm ³]	Height [m]	Temp. [°C]	[%C] _{in} [ppm]	Ar/air	\dot{Q}_{inert} [Nm ³ /h]
1	2.68	0.152	1603	173	50/50	0.537
2	2.78	0.157	1581	198	75/25	0.569
3	2.73	0.154	1589	191	75/25	0.569
4	2.28	0.129	1598	189	0/100	0.474
5	3.35	0.190	1588	146	50/50	0.537

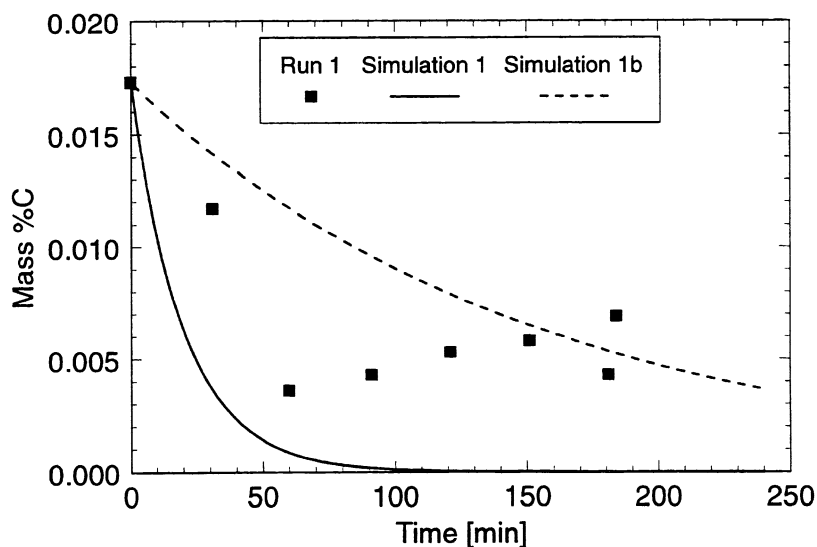


Figure 4.2: Decarburization of Si at 1600 °C. Run 1 is result from [6], Simulation 1 is result of simulation employing the Powersim decarburization model with $k_c=1 \times 10^{-4}$. \dot{Q}_{inert} and V_{melt} is equal to flow rate and melt volume in the trial designated Run 1. Simulation 1b is same as Simulation 1 but with $k_c = 5 \times 10^{-6}$ m/s.

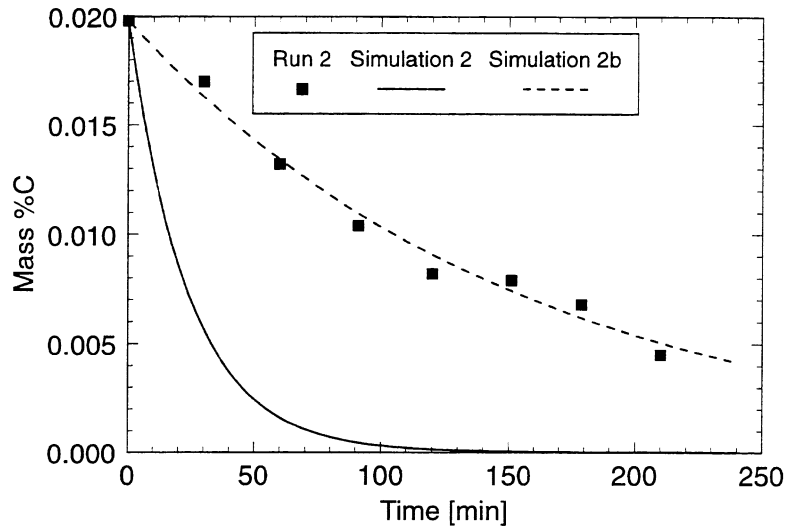


Figure 4.3: Decarburization of Si at 1600 °C. Run 2 is result from [6], Simulation 2 is with $k_C = 1 \times 10^{-4}$. \dot{Q}_{inert} and V_{melt} is equal to flow rate and melt volume in the trial designated Run 2. Simulation 2b is same as Simulation 2 but with $k_C = 5 \times 10^{-6}$.

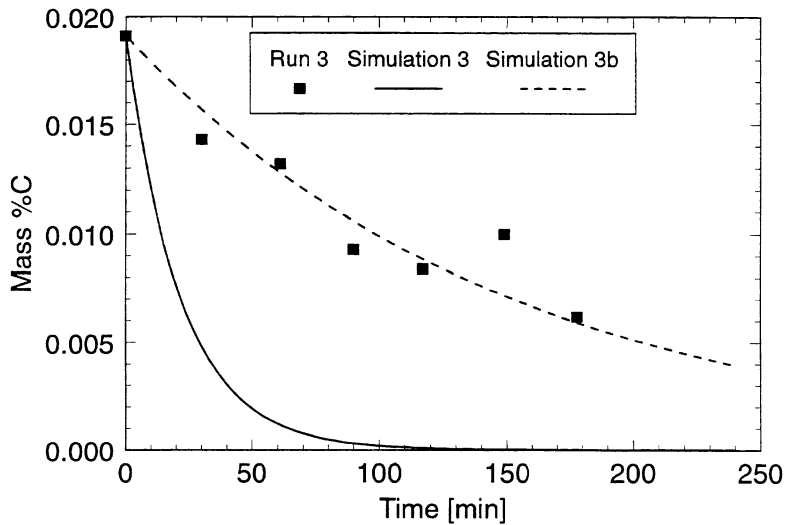


Figure 4.4: Decarburization of Si at 1600 °C. Run 3 is result from [6], Simulation 3 is with $k_C = 1 \times 10^{-4}$. \dot{Q}_{inert} and V_{melt} is equal to flow rate and melt volume in the trial designated Run 3. Simulation 3b is same as Simulation 3 but with $k_C = 5 \times 10^{-6}$.

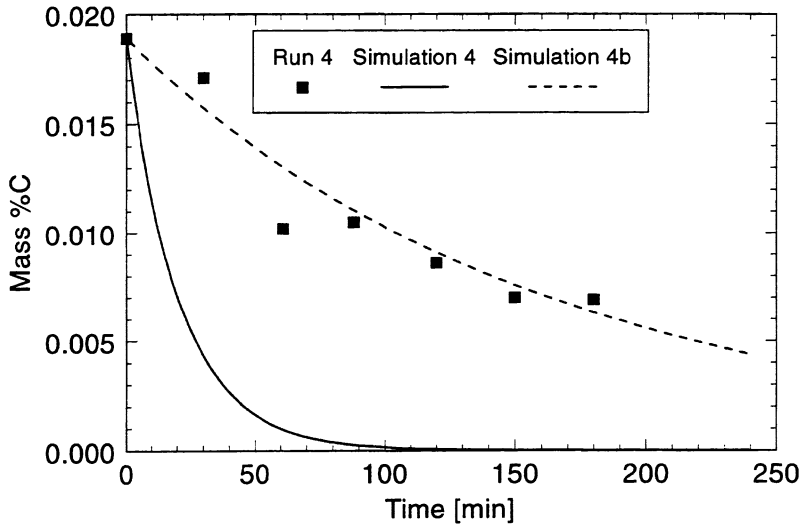


Figure 4.5: Decarburization of Si at 1600 °C. Run 4 is result from [6], Simulation 4 is with $k_C = 1 \times 10^{-4}$. \dot{Q}_{inert} and V_{melt} is equal to flow rate and melt volume in the trial designated Run 4. Simulation 4b is same as Simulation 4 but with $k_C = 5 \times 10^{-6}$

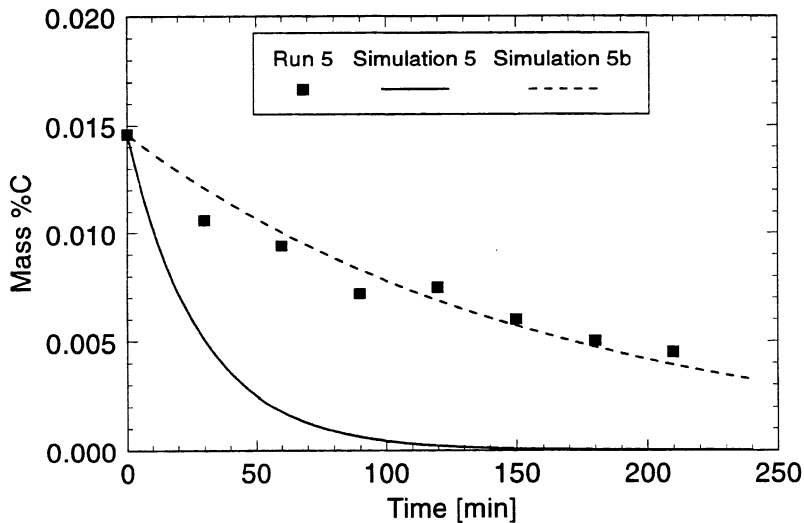


Figure 4.6: Decarburization of Si at 1600 °C. Run 5 is result from [6], Simulation 5 is with $k_C = 1 \times 10^{-4}$. \dot{Q}_{inert} and V_{melt} is equal to flow rate and melt volume in the trial designated Run 5. Simulation 5b is same as Simulation 5 but with $k_C = 5 \times 10^{-6}$

The figures above indicate that there is a large resistance against removal of carbon from liquid silicon when blowing air and Ar into the melt, since the simulation model gives a mass transfer coefficient of 5×10^{-6} m/s. Bubbles tend to break up and coalesce [13] and bath circulation reduces the residence time, τ_b , [14]. These conditions are not taken into account. Thus, k_c is probably greater than 5×10^{-6} m/s. Nevertheless, the value of k_c should be considerably lower than the value of roughly $k_c = 1 \times 10^{-4}$ m/s corresponding to resistance in the melt boundary layer. This supports the assumption, mentioned in the introduction to this chapter, that a reaction between oxygen in the gas bubbles and the liquid silicon gives a silica layer around the bubbles, as illustrated in figure 4.7, that slows down the decarburization. This layer would be solid since silica has a melting point of 1723 °C [4]. It should be dense because the molar volume ratio between oxide and metal, $\frac{M_{\text{oxide}} \rho_{\text{metal}}}{M_{\text{metal}} \rho_{\text{oxide}}}$, is greater than one [15], about two for silicon and ferrosilicon.

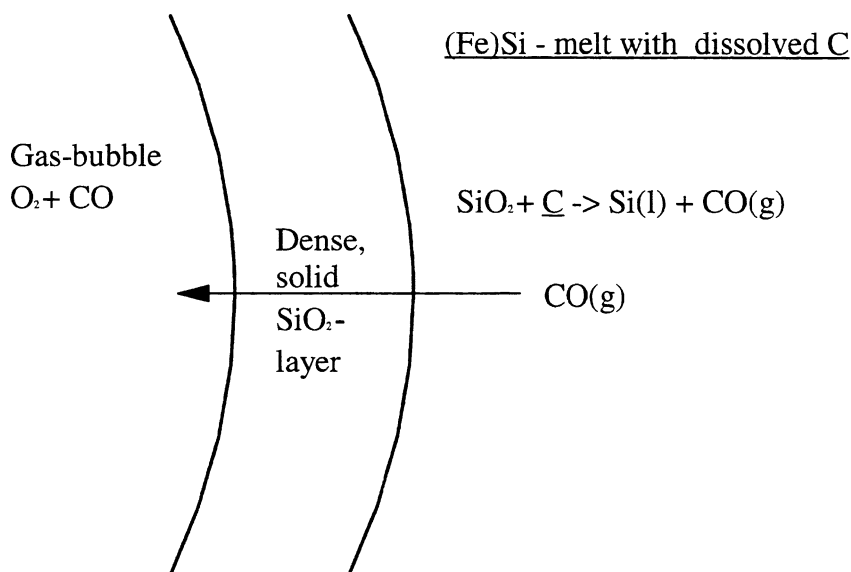


Figure 4.7: Formation of a silica-layer around a rising gas bubble when blowing oxygen into liquid (ferro)silicon. The dense silica layer may result in a small mass transfer coefficient; $k_c \ll 10^{-4}$.

Industrial case - decarburization of ferrosilicon with 75 mass%Si

The Powersim decarburization model presented above is here employed for an industrial case with a 1.6 m³ bottom stirred ladle. This corresponds to 5.1 mt of liquid FeSi75. The bath height is set to 1.4 m. The simulations are performed with an inert gas flow rate of 15 and 30 Nm³/h, and we assume that the injected gas gives spherical bubbles with an average diameter of 40 mm. Metal bath temperature is set to 1600 °C and the initial carbon level is 150 ppm, which is equal to the solubility of carbon in pure FeSi75 [2]. The result of the simulations with two different mass transfer coefficients, 1×10^{-4} m/s and 5×10^{-6} m/s, is presented in figure 4.8. From the figure below it is seen that the decarburization rate is very low. Reduction of the carbon level from 150 ppm to 100 ppm takes 4 hours with an inert gas flow rate of 15 Nm³/h. Increasing the gas flow improves the rate of decarburization, but even at 30 Nm³/h the removal of carbon is slow.

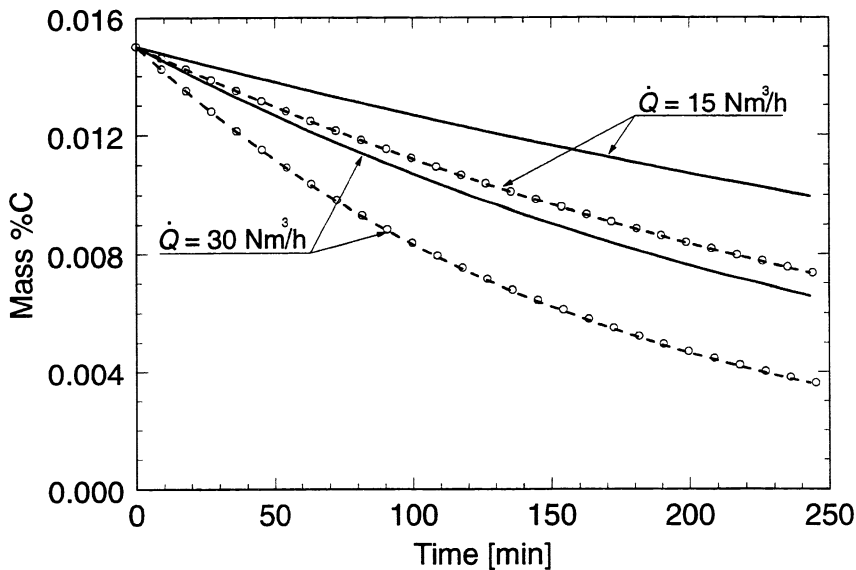


Figure 4.8: Decarburization of 1.6 m³ FeSi75 at 1600 °C. Mass transfer coefficient : ---- 1×10^{-4} m/s and — 5×10^{-6} m/s. Gas flow rate is 0.05 and 0.1 NI/(min kg) and average bubble size, d_b is set to 40 mm. Decarburization at equilibrium, see eqn. (4.30), between CO(g) and \underline{C} is also included and designated \circ .

A flow rate of 30 Nm^3 inert gas per hour, which is equal to $\sim 0.1 \text{ NI}$ per minute and kg melt, is on the high side in a practical industrial environment.

From figure 4.8 it is seen that decarburization at equilibrium between $\text{CO}(\text{g})$ and dissolved carbon in the melt is almost equal to the decarburization rate given by the model when the mass transfer coefficient is 10^{-4} m/s .

To demonstrate the influence of the temperature on the decarburization rate, figure 4.9 gives the result when the temperature in the bath is increased from 1600 to 1700 °C. The inert gas flow rate is $30 \text{ Nm}^3/\text{h}$ and $k_c = 5 \times 10^{-6} \text{ m/s}$. Initial carbon content is set to 270 ppm, which is equal to the solubility level in FeSi75 at 1700 °C and 150 ppm for the comparison with the simulation at 1600 °C.

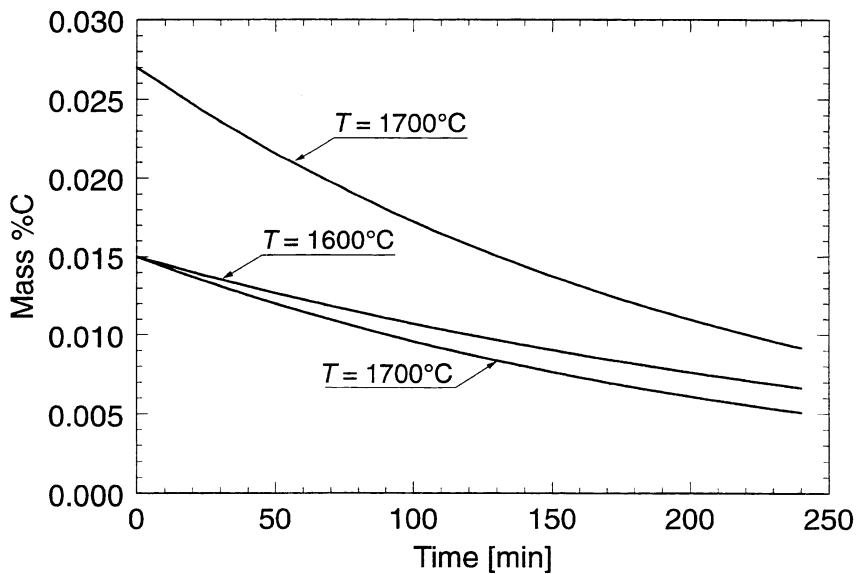


Figure 4.9: Decarburization of 1.6 m^3 FeSi75 at 1600 °C and 1700 °C. Mass transfer coefficient is $5 \times 10^{-6} \text{ m/s}$ and gas flow rate is $0.1 \text{ NI}/(\text{min kg})$. Average bubble size, d_b is set to 40 mm.

As seen from the figure above both the temperature and the carbon activity in the melt gives a higher rate of carbon removal.

4.2 Physical removal of SiC particles to slag and lining

4.2.1 Removal by settling

Inclusions or particles in metal melts can be lighter than the molten metal (which is the usual situation found in steelmaking) making them float up and be collected by slag or dross phase at the top of the melt. This seems to be the presumed mechanism for removal of SiC particles in ferrosilicon melts up to now [16]. However when looking at the density differences based on latest data available, it is found that it should take several hours for the particles to float up.

The terminal velocity for a particle with density ρ_p is given by the well-known Stoke's equation valid for spherical particles and Reynolds number $Re < 2$

$$u_r = \frac{2\Delta\rho g a^2}{9\rho\nu} \quad (4.38)$$

Figure 2.9 shows that the density of α -SiC is reduced from 3.21 g/cm³ at room temperature to 3.13 g/cm³ at 1450 °C. For SiC particles in ferrosilicon with 75 mass% Si $\Delta\rho/\rho = 0.017$. The kinematic viscosity for FeSi75 at this temperature is taken to be 0.35×10^{-6} m²/s, see figure 2.7. For particles of size $2a = 2 \times 10^{-5}$ m (20 μ m) the terminal velocity u_r is then 1.1×10^{-5} m/s. Due to the small difference in densities between silicon carbide and FeSi75 melt, it would take a spherical particle of SiC with diameter 20 μ m about 25 hours to float up 1 metre. Using a density of 3.1 g/cm³ for SiC, which is the data for β -SiC in figure 2.9, gives 16½ hours for a particle with diameter 20 μ m. (If the ferrosilicon melt is between 76 and 77 mass% Si, which is not unusual, the density difference between the melt and SiC-particles is close to zero). This means that flotation should not be an effective mechanism for removal of SiC particles in ferrosilicon with 75 mass% Si.

4.2.2 Turbulent removal to walls and top slag

It is expected that particles are removed to walls by turbulence. However, the

results indicate that the walls have a limited capacity to accept particles. Thus, turbulence would not be a limiting factor. The theoretical treatment of turbulent removal in the steady state case is given in Appendix E.

4.3 Experimental setup and results

During tapping the metal temperature drops to between 1500 and 1700 °C, precipitating dissolved carbon as solid SiC-inclusions. Removal of total carbon from silicon and ferrosilicon must then include both decarburization of dissolved carbon and removal of particles. Removal of dissolved carbon has been discussed in the previous section. In the following experiments, carried out on production run at Elkem Thamshavn, the mechanism of particle removal was studied.

4.3.1 Carbon removal by pouring from one ladle to another and bottom plug stirring.

Experimental setup

Figure 4.10 shows the experimental setup for centric bottom Ar-bubbling. Inert gas supplied from a gas cylinder battery was controlled and metered employing existing gas regulation system at Elkem Thamshavn. This Gas Mixing Cabinet has input for two types of gases and consist of flow meters, control valves and stop valves in addition to manometers. The flow meters are connected to an electronic counter giving both the actual flow rate in m³/h and accumulated amount of gas. The flow meter employed in the experiments, Fischer & Porter type D10A5453DA, was calibrated for air at 20 °C and 5 bar pressure. The control valve at the gas cylinder battery was therefore set to give 5 bar. Then the reading from the flow meter could be used directly only multiplied by the factor $\sqrt{\rho_{\text{air}}^*/\rho_{\text{Ar}}^*}$ ¹, taking the density difference of the gases into account.

The gas was injected into the metal employing a conventional Elkem bottom plug

¹ at 15 °C and 1 ata

with 6 Cu tubes, each with inner diameter 3 mm and outer diameter 3/16" (~ 4.76 mm). Except the first experiment (trial no 710-1) two of the tubes in the plug were plugged to reduce the total gas flow without lowering the gas velocity in the tubes.

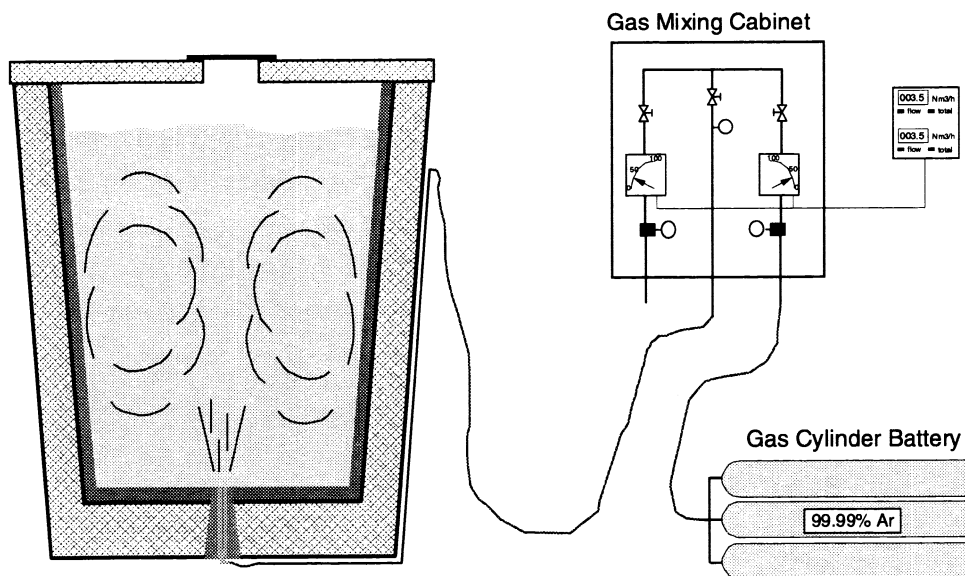


Figure 4.10: Experimental setup for centric bottom Ar-bubbling of FeSi75.

The stirring ladle was cleaned and sprayed with a 30-40 mm thick layer of refractory before each experiment. The refractory spray employed was UNICAST-H from Svenska Silikaverken AB, having an recommended operating temperature of 1550 °C [17]. The softening temperature or the thermal cone for this material was not known, but the producer and supplier, Svenska Silikaverken AB, carried out the necessary thermal cone tests. According to C. Wennnerhorn at Svenska Silikaverken AB [17], UNICAST-H has a grain-size less than 5 mm. The coarse fraction consists mainly of mullite, whereas the very fine material i.a consists of high temperature cement. Mullite has a melting temperature of around 1800 °C and the fine material has typically a melting temperature of 1440 °C. To make cones with satisfactory close packing, they had to screen out particles >0.4 mm; that meant around 50% of the mullite. The measured SK-value, according to [17], is lower than the real value due to the removal of half the mullite. They have

therefore adjusted the measured values for the thermal cone to SK28 corresponding to a temperature of 1635 °C. The chemical composition and thermal data of this castable refractory is given in table 4.3

TABLE 4.3: Chemical composition and refractoriness for UNICAST-H [17,18]

Al ₂ O ₃ + TiO ₂	63%
SiO ₂	31%
Fe ₂ O ₃	0.9%
Refractoriness	SK28 (1635 °C)

Procedure

Metal was tapped from the furnace into a standard tapping ladle. Samples were taken from the tapping stream every 20 minute. These samples were drawn employing the TK40 scoop sampler described in chapter 4.1. The filled-up ladle was then transported to a station for sampling and temperature measurement. An immersion metal sample was taken with the MINCO Immersion Sampler described in chapter 4.2. The temperature was measured with a Leeds&Northrup portable dipping thermocouple, type SYSC 429R (700 - 1700 °C).

The tapping ladle was then transferred by overhead crane and poured into the preheated stirring ladle. The gas flow was on during pouring to avoid clogging of the Cu-tubes in the bottom plug.

When the ladle was full, a refractory lid was mounted on the top to reduce heat loss by radiation and to give a small excess pressure of argon above the melt. This lid had a hole for sampling and temperature measurement. The hole was closed with an insulating plate between each sampling. Immediately after the lid was in place, a new immersion sample (MINCO) was taken and the temperature measured followed by filter sampling. The filter sample was taken as described in chapter 3.4. After filter sampling was completed, immersion samples were drawn every fifth minute during the gas purging. In connection with the sampling the melt

temperature was determined.

At the end of the gas purging, a new filter sample was taken before ending the experiment with a final immersion sample and temperature measurement. The metal was then cast into cast iron moulds. Samples were taken of the cast alloy.

The empty ladle was then put aside to be cooled. Samples were taken from the layer on the walls and from dross in the ladle, see figure 4.11.

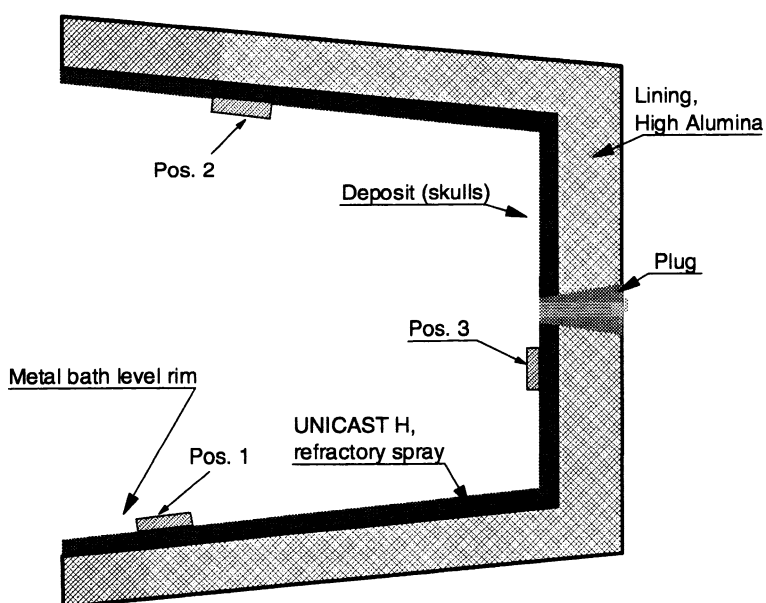


Figure 4.11: Positions for sampling of deposit on the ladle wall and bottom.

Results

Five experiments with argon bubbling with the centric bottom plug were carried out. The experiments lasted from 30 to 50 minutes effective purging time. The experiments have been given the same number designation as the actual tapping number at Elkem Thamshavn.

Figure 4.12 shows how the carbon content drops during the treatment for each

experiment. Here the time zero indicates the first sample after the metal has been poured into the stirring ladle. The pouring time varied from 1½ to 4 minutes. The sample on the negative end of the time scale is the immersion sample taken after tapping was completed and 3 to 5 minutes prior to start pouring.

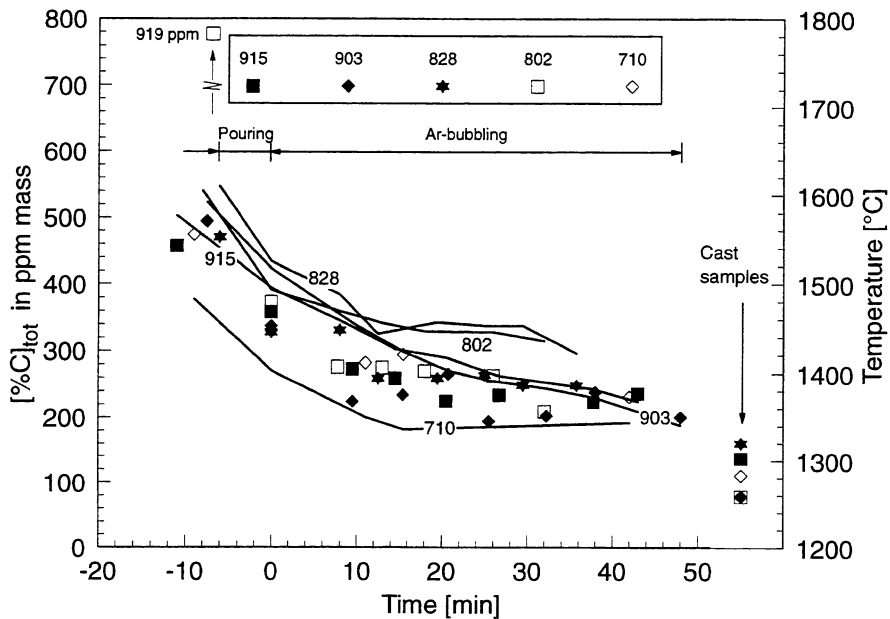


Figure 4.12: Change in carbon content and temperature in liquid ferrosilicon with 75 mass% Si from production run at Elkem Thamshavn during centric bottom Ar-stirring. The effect of pouring, from $t = -t$ to $t = 0$ on the time scale, on the carbon content is included in addition to the change from final liquid sample to the cast sample.

It is seen from the figure above that carbon drops around 150 ppm during pouring in all experiments. An exception is trial no 802-1, where the C-content measured in the tapping ladle before start pouring, most likely is incorrect since it was higher than the carbon content in the sample from the furnace tapping stream.

During Ar-bubbling, which is from time $t = 0$ to time t , the carbon content drops another 150 ppm, with most of the reduction within the first 10 minutes.

Then again there is a drop in the carbon content from the end of purging to the

sample taken of the cast metal.

From the figure above it is also noted that the temperature falls steeply during pouring and in the beginning of the Ar-blowing then more slowly.

Filter samples

As mentioned previously filter samples were drawn at the beginning of the stirring and at the end of the stirring. For heat 903-1 and 915-1 both samples were successful and only these four samples were analysed. The filter sampling, sample preparation and image analyses followed the same procedure as described in chapter 3.4. The first sample, designated F1, was taken after the stirring ladle was filled. For heat no 903-1, this filter sample was drawn between six and nine minutes after end pouring. The filter sample at the end of stirring is designated F2. Sample number 915-1F1 was drawn from seven and 10 minutes after the ladle was filled. In table 4.4 the mean diameter and the mean inclusion concentration for each filter sampling are given. The values in column six, named "Equiv. C-content", is the amount of carbon filtered as inclusions when assuming that all inclusions are spherical and consist of SiC. Column seven gives the carbon content in the filtered metal, whereas the carbon in the metal bath is presented in the last column. Figure 4.13 gives the size distribution for heat no 903-1 and 915-1 at the beginning of Ar-stirring and at the end of the stirring. Comparison with the result from the filter sampling of standard and refined ferrosilicon, see figure 3.11 and 3.12, shows that the alloy treated by pouring from one ladle to another followed with Ar-stirring has a number size distribution halfway between the refined and the standard quality. As seen from table 4.4 the mean inclusion diameter is 2.8 μm , which is almost the same as for refined, cf. table 3.4, and lower than for standard FeSi75, cf. table 3.3.

TABLE 4.4: Inclusion concentration on volume basis and mean particle diameter in Ar-stirred ferrosilicon measured from filter sampling. The equivalent C content is calculated amount of carbon in the melt assuming all particles consist of SiC.

Heat no	Amount of metal sampled m_{melt} [g]	Mean inclusion diam. [μm]	Inclusion conc. on vol. basis [ppm]	Melt bath temp. [$^{\circ}\text{C}$]	Equiv. C-content ¹⁾ [ppm]	C in filtered metal	C in metal bath, Minco
903-F1	1443	3.3	45	1487	13	137	281
903-F2	122	3.0	9	1357	3	148	219
915-F1	558	2.3	39	1474	12	137	315
915-F2	363	2.6	51	1375	16	214	230
Mean		2.8	36		11	159	

¹⁾ Assuming all inclusions is SiC

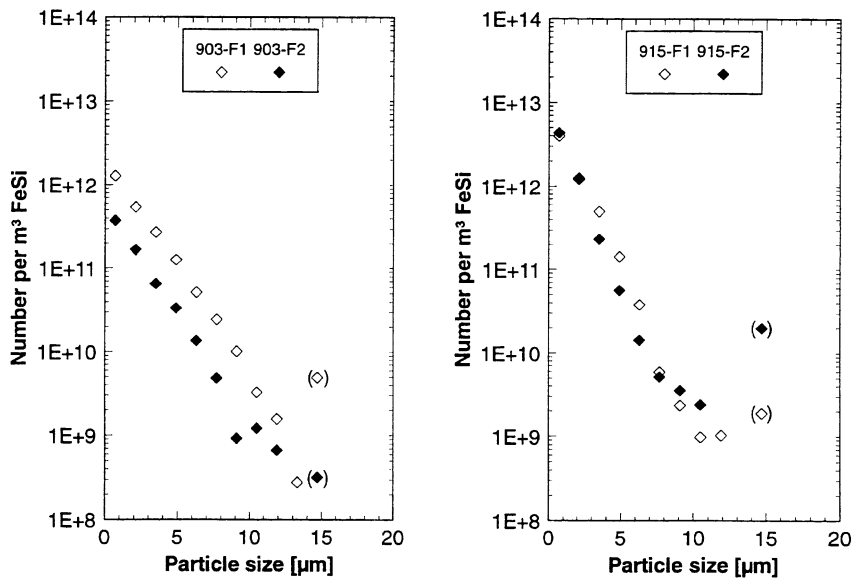


Figure 4.13: Inclusion number size distribution in Ar-stirred FeSi75. Sample F1 was taken between 5 and 10 minutes after start stirring, whereas sample F2 was drawn at the end of stirring. Numbers in parenthesis have higher statistical uncertainty.

Carbon in dross and skulls

The samples from ladle wall, cf. figure 4.11, and the dross were prepared and analysed. In table 4.5 the analysed carbon content in these samples is given together with the thickness of the deposit layer. The deposits on the wall or skulls, were more or less sintered to the refractory layer. To avoid possible influence on the carbon analysis, as much as possible of refractory was removed before the samples were analysed.

The numbers in table 4.5 show a wide scatter that is most likely due to problems with sample preparation. In any case, these analyses show that there is a high content of carbon in some of the samples taken from the wall. The layer in the bottom of the ladle was mainly pure metal, reflected in the low carbon content in some of these samples. The amount of carbon removed during pouring and bubbling should on average correspond to a carbon content of 1800 ppm in skulls and dross. The amount of these deposits is presented in table 4.5. However, as seen from this table the carbon content in the skulls and dross is lower than 1800 ppm.

TABLE 4.5: Carbon content in ppm in samples of ladle wall deposits and ladle dross. Thickness of deposits and dross is δ . Positions refer to fig. 4.11.

Trial no	Skulls on ladle wall				Bottom skulls		Dross	
	Pos. 1		Pos.2		Pos. 3			
	ppm C	δ [cm]	ppm C	δ [cm]	ppm C	δ [cm]	ppm C	δ [cm]
710-1	585	1.9	290	2.0	721	12.0	1165	4.2
802-1	3500	2.6	70	1.6	400	10.3	450	1.6
828-1	n.a. ^{*)}	0.7	470	0.6	80	1.3	60	1.4
903-1	1100	1.5	1400	1.5	50	10.0	670	2.9
915-1	90	2.0	564	3.0	313	6.0	40	3.5

^{*)} not analysed, the sample was too small

The evaluation of sampling techniques demonstrated that the oxide scoop sampler gives an underestimate of the carbon content in liquid ferrosilicon, cf. fig. 3.2 ch. 3.1. The scoop sampler may be regarded as a small ladle. The deposit on the scoop was examined for two of the heats (heat no 1342-1 and 1343-1) included in the investigation of sampling methods. As mentioned in chapter 3.1, the scoop samplers were used to draw samples from both the hot tapping stream and the colder teeming stream. In the following TaS refers to the scoop sampler employed for the Tapping Stream, whereas TeS is synonymous with the sampler for the Teeming Stream. The deposit layer in the TaS was to a great extent sintered to the refractory, whereas the skulls in the TeS slipped easily from refractory wall leaving a thin metallic film.

Samples of the wall of the scoop including the thin metallic film and part of the refractory were taken out for analyses. The samples from the TeS consisted of 90-95% refractory and 5-10% alloy, while the specimens taken from the TaS consisted of around 50/50 refractory and metal.

In table 4.6 the result of the carbon analyses is given, and it is seen that the samples taken of the deposit from the TaS have carbon contents from 0.3 to 1.8 mass%. Along with the carbon analyses of the deposits, the analyses of the corresponding metal are given.

TABLE 4.6: Carbon content (here given in percent) in sample of deposit on the wall of the scoop sampler, $[\%C]_{\text{layer}}$, along with corresponding carbon content in liquid metal. TaS = Tapping Stream scoop sampler and TeS = Teeming Stream scoop sampler. For comparison the alloy composition is included.

	1342-1				1343-1			
	TaS1	TaS2	TeS1	TeS2	TaS1	TaS2	TeS1	TeS2
$[\%C]_{\text{layer}}$	n.a. ^{*)}	1.53	0.0120	0.0080	1.79	0.31	0.0140	0.0070
$[\%C]_{\text{metal}}$ ^{**)}	0.0860	0.0970	0.0270	0.0170	0.1200	0.0920	0.0100	0.0100

^{*)} not analysed; sample destroyed under preparation. ^{**)} Taken with the MINCO sampler.

The numbers in the table demonstrate that there is an accumulation of carbon in the layer to the wall. Even the deposit layers from TeS, which consist of 90 - 95% refractory material, the content of C is from 70 to 140 ppm. The carbon content in the refractory material was analysed to be 35 ppm. Thus, a simple mass balance gives between 0.04 and 0.18 mass% C in the metallic part of the layer from the scoop sampler employed for the teeming stream.

As seen from table 4.5 and 4.6 there seem to be an accumulation of carbon in the layer towards the wall in both the oxidic scoop sampler and the stirring ladles. This has been verified by metallographical investigation of the interface between the metallic and the oxidic part of this layer.

Samples of the deposit in the scoop sampler and ladle-skulls from the purging experiments were prepared for metallographical examination. The metallographic examination and analyses were carried out at the JEOL 8900 Microprobe Analyser (EPMA) at Institute of Metallurgy, NTNU. Figure 4.14 shows a micrograph of the metal-oxide transition area of the wall deposit from the TaS-scoop used as sampler for heat no 1579-1.

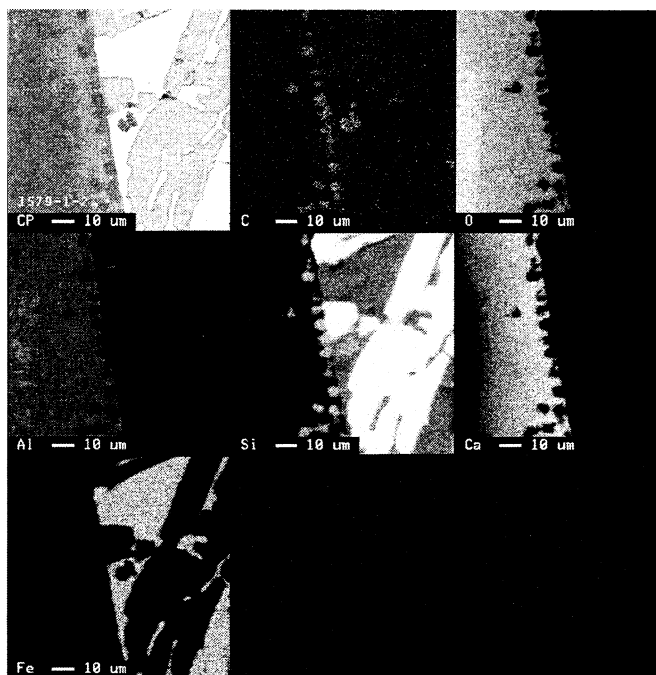


Figure 4.14: X-ray micrograph of deposit at the wall of the TK40 scoop sampler. Sample taken from tapping stream, heat no 1579-1. The scoop wall is to the left and the metal is to the right. The image at the top and to the left is the backscatter image (BEI) while the other is X-ray mapping of C, O, Al, Si, Ca and Fe.

The X-ray mapping images in figure 4.14 shows that carbon is present together with silicon as small particles. Quantitative X-ray analysis shows that these particles are SiC since they contain approximately 50 at% Si and 50 at% C, see table 4.7. It is further seen that these SiC-particles have partly penetrated into the oxidic wall, demonstrated as holes in the X-ray images of O, Ca and Al.

Figure 4.15 gives the X-ray mapping for another sample from the same scoop but with higher magnification. The size of the SiC-particles is 2-8 μm and again it is seen that they have penetrated the surface of the refractory wall inside the scoop. There seem to be roughly three layers of carbide particles on and into the refractory and that the penetration depth is 10-15 μm .

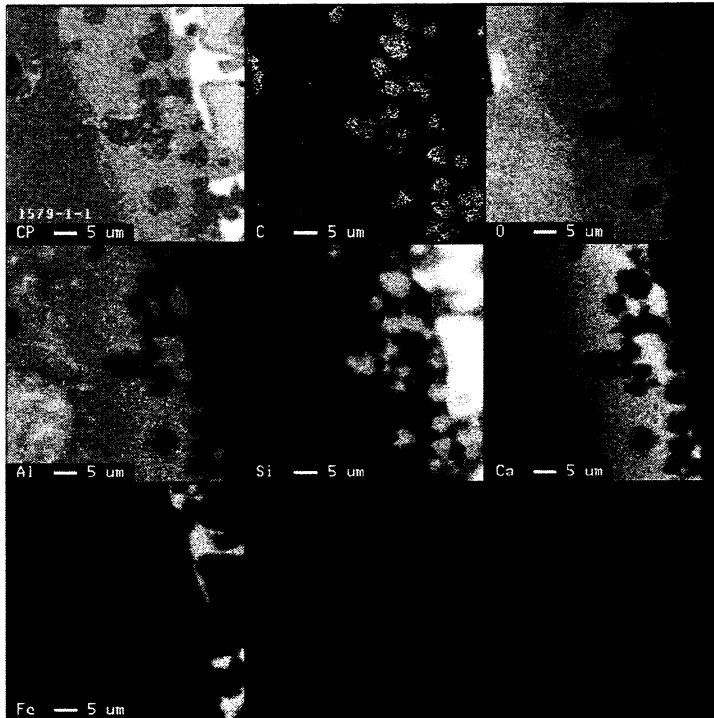


Figure 4.15: X-ray micrograph of deposit at the wall of the TK40 scoop sampler. Sample taken from tapping stream, heat no 1579-1.

The two next figures, fig. 4.16 and 4.17, give new examples of X-ray micrographs from another two heats. The samples are also taken from the transition area between skulls and refractory, and again it is demonstrated how the SiC-particles have penetrated into the oxide surface. In figure 4.17 carbide particles are found as deep as 50 microns into the oxidic mass.

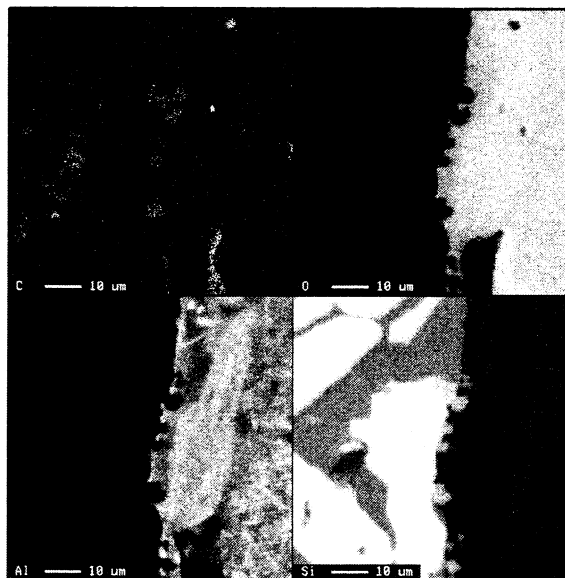


Figure 4.16: X-ray micrograph of deposit at the wall of the TK40 scoop sampler. Heat no 1342-1. The scoop wall is to the right.

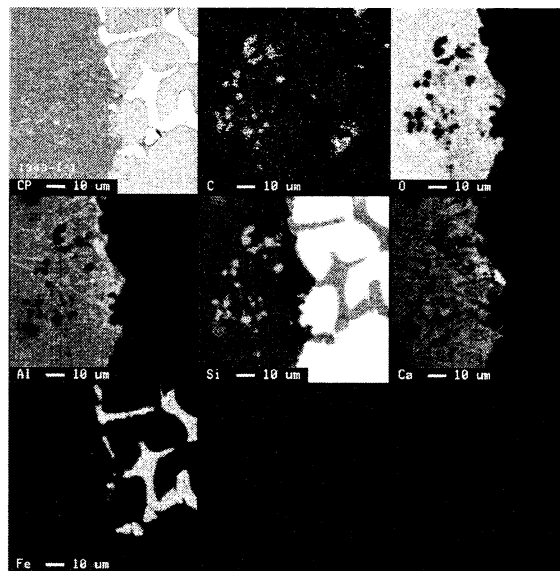


Figure 4.17: X-ray micrograph of deposit at the wall of the TK40 scoop sampler. Heat no 1343-1. The scoop wall is to the left.

As mentioned previously, the samples taken from the ladle wall were cleaned to remove as much as possible of refractory. The sample of the deposit on the sidewall (pos. 1, fig. 4.11) from trial number 828-1 was difficult to clean properly, and was therefore put aside. Thus this was the only sample left from the sampling of ladle skulls in the trials with bottom argon stirring. Figure 4.18 shows X-ray mapping of this sample.

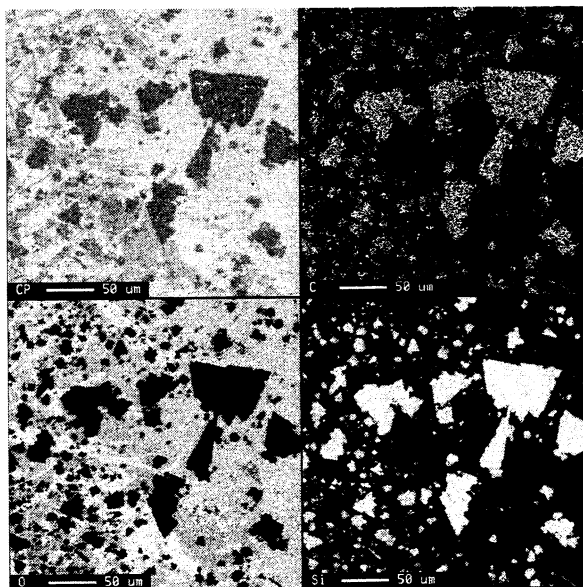


Figure 4.18: X-ray micrograph of deposit at the ladle wall after Ar stirring. Heat no 828-1 sample from position 1, cf. figure 4.11.

The X-ray mapping of the deposit on the ladle wall shows the same pattern as the deposit from the scoop sampler; carbon is present as silicon carbide particles in the oxidic material on the wall. This oxidic material is rich in aluminium, oxygen and calcium in addition to silicon, and may stem from the refractory (UNICAST-H) sprayed on the ladle wall and slag.

As pointed out previously the particles were analysed to be silicon carbide particles. In table 4.7 the result of the quantitative X-ray analyses of five random particles in sample 828-1 are given. The average content of C and Si in the particles was 28.79 mass% and 65.86 mass% respectively, which is equal to 48.8

and 49.8 at%. This gives a Si/C-ratio of 1.02 that shows that the particles are silicon carbide. From table 4.7 it is seen that the analyser registered some aluminium and calcium in the particles. This is most likely due to interference from the Al-, Ca- and O-rich surroundings, cf. fig. 4.18.

TABLE 4.7: Quantitative X-ray analyses in mass% of particles in Sample 828-1.

	Si	C	Al	Ca	Total
1	65.509	29.480	1.154	1.113	97.256
2	65.684	29.494	1.139	1.104	97.421
3	66.211	29.063	0.868	0.821	96.963
4	66.608	27.849	0.876	0.914	96.247
5	65.290	28.064	1.362	1.488	96.204
Minimum	65.290	27.849	0.868	0.821	96.204
Maximum	66.608	29.494	1.362	1.488	97.421
Average	65.860	28.790	1.080	1.088	96.818

Some particles in sample 1342-1 were also analysed and found to have a content of 48 at% Si and 52 at% C, which is in the same range as the analyses in table 4.6.

4.3.2 Carbon removal by gas stirring with refractory lance.

Experimental setup

In addition to the experiments with the bottom plug, trials employing a lance to inject the gas were carried out. The experimental setup for these experiments is shown in figure 4.19. The lance employed, delivered by Hinckley (Scandinavia) OY AB, Finland, had three Cu tubes as gas outlet with inner and outer diameter 3

and 20 mm respectively. The gas outlet was placed 200 mm above the end of the lance.

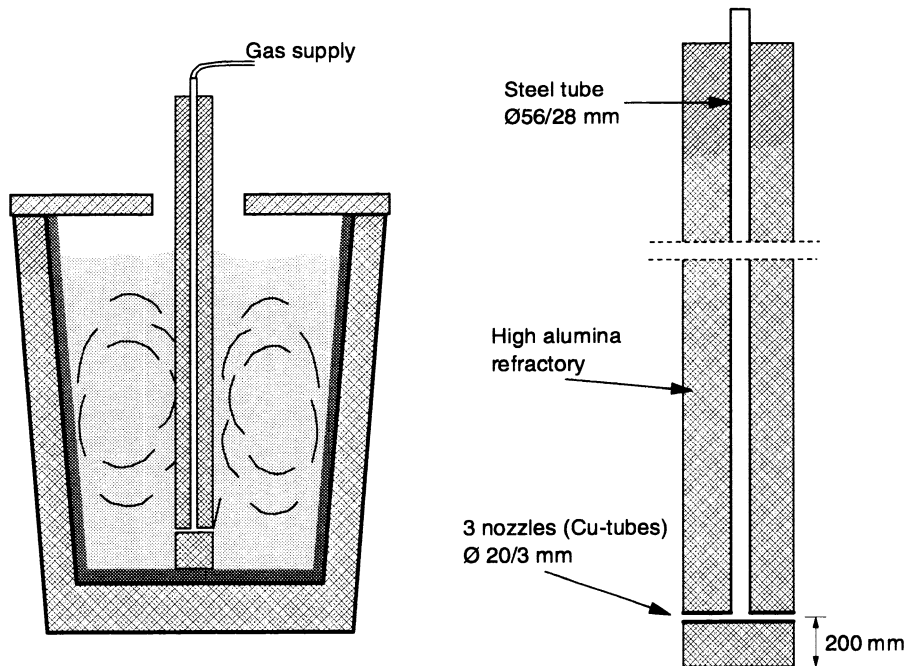


Figure 4.19: Experimental setup for centric ladle stirring with lance and principal drawing of refractory lance. The gas supply system was the same as for centric plug stirring experiments, cf. fig. 4.10.

Procedure and results

The lance was supported on the bottom of the ladle, giving a height of the gas plume equal to the bath height minus 0.2 m. In these lance experiments there was no pouring from one ladle to another before the gas purging. Also for some of these trials reactive gas (air and oxygen) was injected into the metal. The purging time was also shorter (7-15 minutes) for these trials compared with the experiments with bottom stirring.

In figure 4.20 the change in C-content for the experiments with the lance is presented. The C analyses on the negative end of the time scale are from the

immersion sample taken after the tapping was completed and the ladle transported into position and before immersing the lance. Time zero indicates the first sample after the lance is in position. This sample was taken from 1 to 5 minutes after the lance was in position.

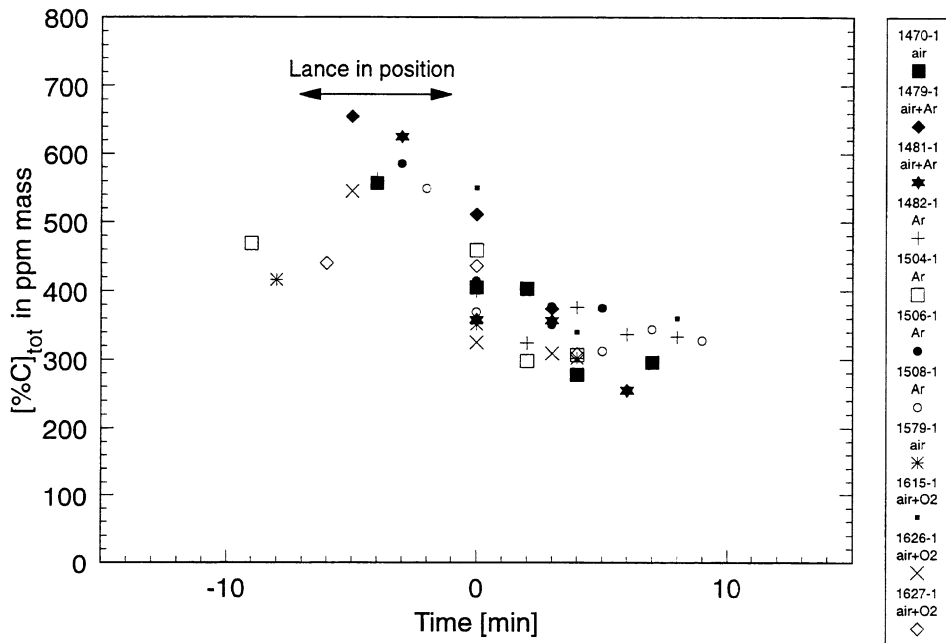


Figure 4.20: Change in carbon content in liquid ferrosilicon with 75 mass% Si from production run at Elkem Thamshavn during lance stirring. Type of gas injected is given in the frame along with the designation symbols.

Also, in these experiments there is an immediate drop in carbon of around 150 ppm. However, the variation was greater than in the experiments with the plug.

The influence of oxygen in purging gas is demonstrated in table 4.8. Oxygen in the gas seems to enhance the removal of carbon as would be expected. Even if the trial with the extremely high start value of carbon (trial no 1615-1) is excluded, an increase in the carbon removal is observed. However, there is also a difference in melt temperature between these two categories of trials. The trials with oxygen added to the gas have a higher start temperature and a lower temperature drop. This is due to the exothermic heats of oxidation for Si, Al and Ca. This oxidation will

give some slag probably contributing to the removal of silicon carbide.

TABLE 4.8: Change in total carbon, $\Delta C_{\text{tot}} = [\%C]$ (before start of purging) - $[\%C]$ (at end of purging). Melt temperature before and at end of purging is also included.

Trial no	[%C] bef.	[%C] end	ΔC_{tot}	Gas-mixture	% O ₂ in gas	Temperature [°C]	
						before	end
1470-1	557	296	262	air	21	1576	1485
1479-1	655	374	281	air + Ar	10	1596	1512
1481-1	625	255	370	air + Ar	10	1367	1336
1482-1	563	333	230	Ar		1441	1369
1504-1	469	307	162	Ar		1485	1377
1506-1	585	375	211	Ar		1499	1401
1508-1	549	344	205	Ar		1513	1388
1579-1	416	302	115	air	21	1552	1484
1615-1	850	360	490	O ₂ + air	43	1548	1518
1626-1	545	309	236	O ₂ + air	46	1513	1436
1627-1	440	308	132	O ₂ + air	47	1566	?
Mean	584	315	269	O ₂ + inert		1531	1462
Mean	541	340	202	Ar		1485	1384
Mean excl. 1615-1	540	307	233	O ₂ + inert		1528	1451

4.3.3 Comparison between the results from stirring with plug and lance.

Figure 4.21, where the results for both the experiments with plug and lance are put

together, shows that the carbon removal with the lance seems to follow the same pattern as with the plug and that both methods give an immediate drop in C content in the alloy of around 150 ppm. Adding oxygen to the gas appears to have only a small effect on the carbon removal as discussed above.

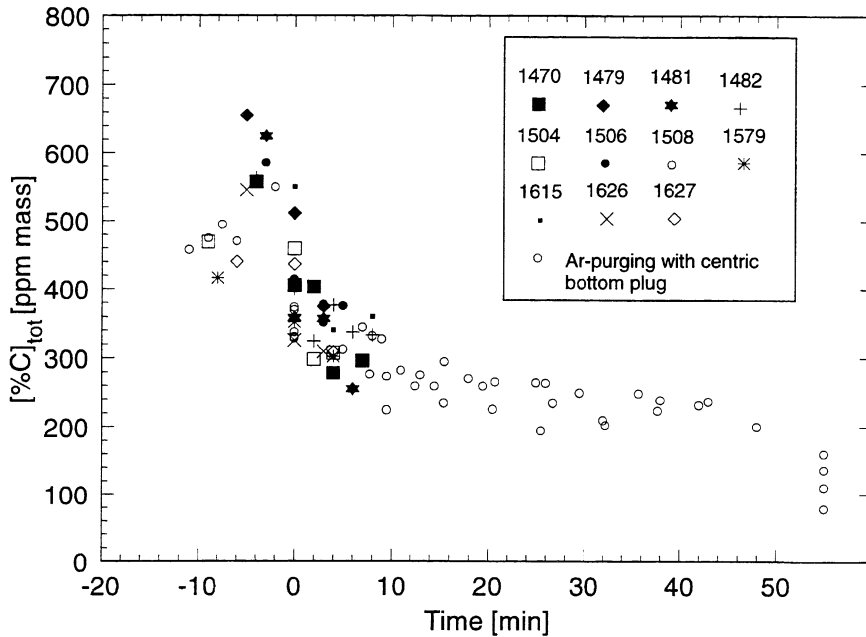


Figure 4.21: Change in C-content in liquid ferrosilicon with 75 mass% Si during lance-stirring and centric bottom plug stirring. The trials with plug are given the same designation symbol, for detail see figure 4.12.

As pointed out previously in section 4.3, after the initial period of about 10 minutes there is only a small reduction of the total carbon. This indicates that flotation or removal to walls is limited. This will be discussed in the next chapter.

4.4 Change in carbon during casting, solidification and crushing and screening

The metal is cast into iron moulds by emptying the ladle over a lip at the top. A layer of small sized ferrosilicon from the crushing and screening plant protects the

moulds against wear from the teeming stream. The solidified alloy is stored and then crushed and screened into appropriate sizes. Ferrosilicon and silicon are brittle alloys that create fines during the crushing and screening operation.

Figure 4.12 shows that the carbon content in the cast samples is about 100 ppm lower than in the final sample drawn from the stirring ladle. This reduction in carbon content can be due to

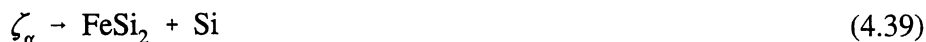
- i. oxidation of dissolved carbon and/or SiC particles during teeming
- ii. segregation of dissolved carbon
- iii. “pushing” of SiC particles by the solidification front
- iv. transfer of SiC particles to an oxidic phase (slag or refractory)

4.4.1 Oxidation of C and SiC during teeming

Oxidation of dissolved carbon and silicon carbide particles has been treated in the beginning of chapter 4.

4.4.2 Segregation

During solidification of Si-rich Fe-Si alloys (mass% Si > 58.2), primary silicon first precipitates as the temperature of the melt reaches the liquidus temperature. The proportion of precipitated silicon and melt will follow the lever rule. Solid silicon has approximately no solubility of iron. The remaining melt is then enriched in Fe as the temperature falls and at the eutectic temperature, 1207 °C, the melt has a silicon content of 58.2 mass%, see the Fe-Si phase diagram in Appendix F. At equilibrium this rest melt will solidify into an iron-silicon high temperature phase, ζ_{α} , and a secondary Si-phase. When the ferrosilicon alloy is cooled further, the following eutectoid reaction takes place at 937 °C [19]



According to H. Tveit [19], the abrasion resistance for ferrosilicon decreases with the amount of ζ_α - phase in the alloy. Thus, fines created during crushing and screening will be enriched in Fe and other alloying elements that accumulate in the molten zone during solidification.

Depending on the segregation coefficient, the concentration of solute elements will increase in the molten zone during solidification. The segregation coefficient for carbon in liquid ferro-silicon is not known, but in pure silicon the equilibrium segregation coefficient, $k_{eq.} = c_s/c_l$, is reported to be 0.058 [20] and 0.07 ± 0.01 [21]. The effective segregation coefficient can be as high as $k_{eff} = 0.7$ in rapid growth techniques [20]. For industrial casting methods it should be somewhere between 0.06 and 0.7. Thus, carbon is expected to segregate and may therefore be enriched in the fine fraction.

In chapter one, the three different products Gransil, Refined FeSi75 and Standard FeSi75 were examined regarding differences in carbon content, and as mentioned the fines from crushing and screening of Standard and Refined were not part of these products. Ferrosilicon fines are occasionally sold separately. Looking at the carbon content in the shipment of fines, see table 4.9, it is seen that fines from refined ferrosilicon are 86 ppm higher in C than lumpy refined, while the fines created from standard grade ferrosilicon are 152 ppm higher in carbon than lumpy.

TABLE 4.9: Comparison of carbon content in fines and lumpy for shipment from Elkem Thamshavn in the period 1. January 1994 - 30. September 1996.

	Refined FeSi75		Standard FeSi75	
	Fines, 0-3 /0-6 mm	Lumpy, +3 mm	Fines, 0-3 /0-6 mm	Lumpy, +3 mm
Mean C-content [ppm mass]	204	118	453	301
SD_x [ppm mass]	45.6	48.2	93.0	200.5
\bar{s}_x [ppm mass]	20.4	4.5	23.8	13.72
Number of samples	5	120	13	213

Since there are few samples (shipments) of fines, a more thorough examination of the carbon content in the fines versus the coarse fraction was required. During crushing and screening a 20 litre sample was drawn from both the 0-3 mm fraction and the + 10 mm fraction. These two samples were from the same castings. The sample from the 0-3 mm fraction was screened on a 1 mm screen with square holes, and the two samples retained were then split into two samples. The sample from the coarse fraction was also split into two parallels. All six samples were then analysed employing the LECO C-analyser described in chapter 3. This procedure was repeated for three different production days.

The result of the carbon analyses in the three fractions (-1mm, 1-3 mm, +10 mm) is presented in the following 3 figures.

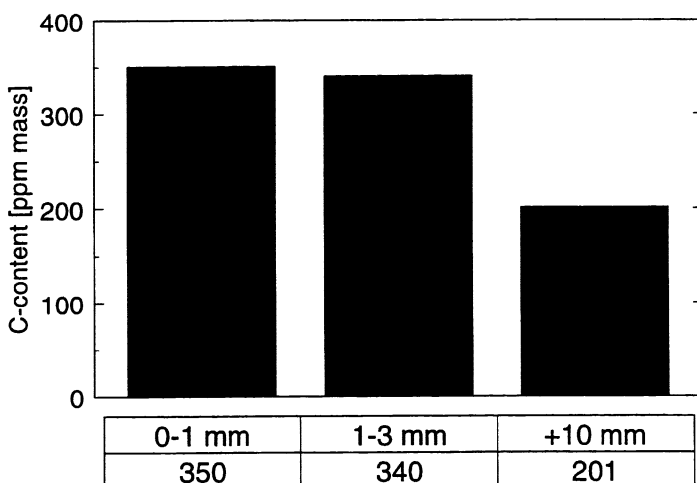


Figure 4.22: Carbon content in samples of the fines, 0-1 and 1-3 mm, and the coarse fraction, +10 mm, of Standard FeSi75 during crushing and screening. The fines fractions is screened out from of 0- 3 mm.

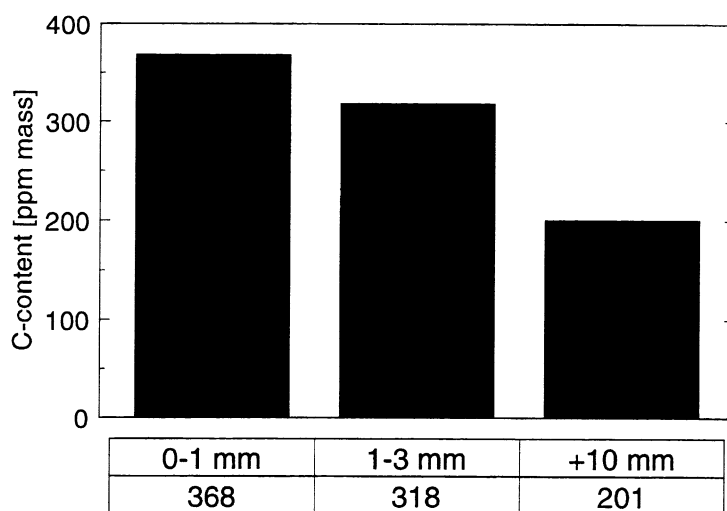


Figure 4.23: Carbon content in samples of the fines, 0-1 and 1-3 mm, and the coarse fraction, +10 mm, of Standard FeSi75 during crushing and screening. The fines fractions is screened out from of 0-3 mm.

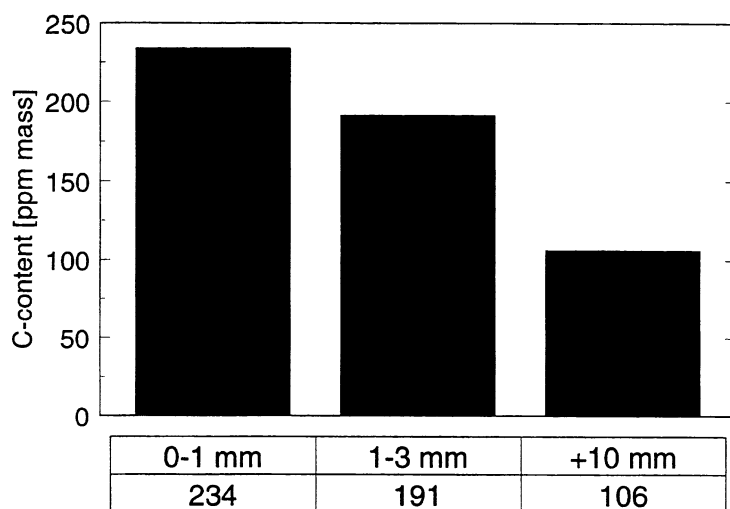


Figure 4.24: Carbon content in samples of the fines, 0-1 and 1-3 mm, and the coarse fraction, +10 mm, of Refined FeSi75 during crushing and screening. The fines fractions is screened out from of 0-3 mm

Figures 4.22 - 4.24 demonstrate that carbon is concentrated in the fine fraction from the crushing and screening operation. In standard ferrosilicon the carbon content is roughly 150 ppm higher in the fines than in the coarse fraction. The amount of fines created during crushing and screening depends strongly on the casting method [19]. FeSi75 cast in iron chill mould give typically 8-15 % less than 3 mm. Also type of crushing equipment employed may have an influence on the final size distribution of the alloy. As seen from the above figures, there may also be an increase in carbon in the finest fraction (0-1 mm) from the crushing and screening. The percentage distributions between 0.1 mm and 1-3 mm in these samples were 66 to 34. The differences in carbon content between the fines and the lumpy in this detailed study corresponds well with the numbers given concerning shipments in table 4.9.

Along with carbon the other elements were also analysed in these three fractions. The result is given in Appendix G. It is seen that silicon is lowest in the 0-1 mm fraction, whereas iron is much higher in this fraction. This agrees with the discussion in the first part of this section. It is also seen that there is a higher concentration of the elements aluminium, calcium and titanium in the finest fractions, which agrees well with the work of H. Tveit [19]. As seen from the table in Appendix G, phosphorous is the only element that increases in concentration in the coarse fraction. Also H. Tveit found that the concentration of P was in inverse ratio to the amount of FeSi₂-phase [19]. A reasonable explanation could be that P - as one exception - has a solid solubility in silicon at the eutectic point of 2.6 mass% [1,22].

4.4.3 Pushing of SiC particles by the solidification front

Besides segregation, another possible mechanism is that precipitated SiC will pile up ahead of the solid/liquid interface, "pushing", and when the last liquid solidifies these particles will either be trapped in the FeSi₂-phase or freeze in at the grain boundaries. The break up of the alloy during crushing may then release the SiC-particles that thus end up in the fine fraction. The pushing and engulfing mechanisms are treated further in the discussion chapter.

4.4.4 Transfer of SiC particles to an oxidic phase

As pointed out in chapter 4.3.1, section *Carbon to dross and skulls*, silica rich oxides (slags) seems to wet silicon carbide well. In ferrosilicon production some slag is formed during tapping, ladle treatment and casting. Slags formed in the ferrosilicon process will float up due the differences in density between the liquid alloy and the slag. Investigation of the wettability of silicate glasses on the surface of SiC [23] showed that glasses containing 50-70 mass% SiO₂, 10-25 mass% Al₂O₃ and 5-17 mass% CaO demonstrated almost complete (perfect) wetting at 1350-1450 °C, whereas glasses with a small amount of alumina and no lime demonstrated high contact angles, see chapter 2.4.4.

Any slag formed in the ferrosilicon process will be rich in silica. The amount of lime and alumina in the slag will depend on the chemical composition of the liquid alloy. Investigation of the surface layer of granulated FeSi75 [24] showed that this oxidic layer had a composition close what should be expected of a slag in equilibrium with the actual alloy composition as given by Tuset et al. [25]. This mean that the slag formed probably will contain 10-30 mass% Al₂O₃, 10-30 mass% CaO and 40 60 mass% SiO₂ and with some minor content of magnesia. This type of slag should wet SiC carbide particles almost completely according to [23].

Cast metal was sampled in such a way so the specimen was continuous from top to the bottom of the casting. The sample was split vertically into two pieces. One of these samples was cut horizontally in three employing a grub saw with a diamond saw blade. The top and bottom slices was made 5-10 mm thick, see figure 4.25. These three samples were then prepared and analysed with respect on carbon together with the other half of the original sample.

Dependant on the tapping weight, one ladle is cast into 5-7 iron moulds. From three different heats, seven samples were taken out from two different moulds and from two different positions in the mould, see figure 4.26

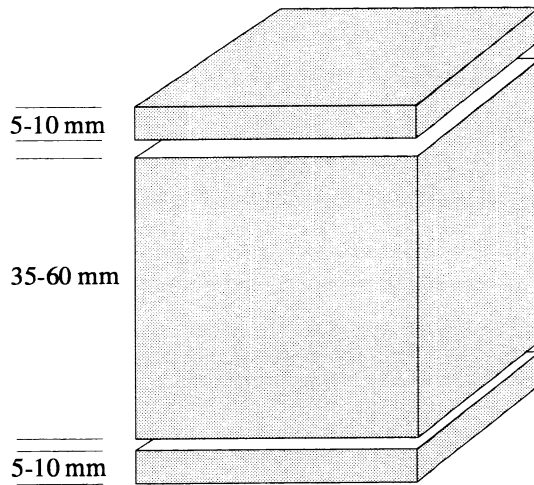


Figure 4.1: Schematic illustration of how the sample from the castings was cut into slices from the top and bottom.

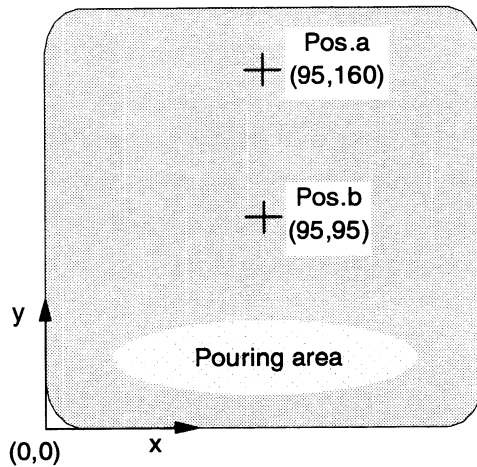


Figure 4.2: Position of sampling of cast samples. The inner dimensions of the mould is 195 cm x195 cm

From casting number 3203 a total of 4 samples was drawn. Samples were taken from both position *a* and position *b*, see figure 4.26, from mould number one and from mould number five. From heat number 3205, one sample at position *b* was taken from mould number five and six. In addition an introductory sample was drawn from heat number 3121, mould number 4, position *b*.

In figure 4.27 - 4.28 the carbon analyses of the top, the middle and the bottom of the casting are given for the 7 moulds investigated. The line across the bars represents the carbon content in the parallel sample of that position and mould. This samples should give the same level of carbon and represent the mean C content in the alloy. Except for samples in 3203-1b, all the samples from this casting gives almost the same carbon content, respectively 91, 103 and 113 ppm C.

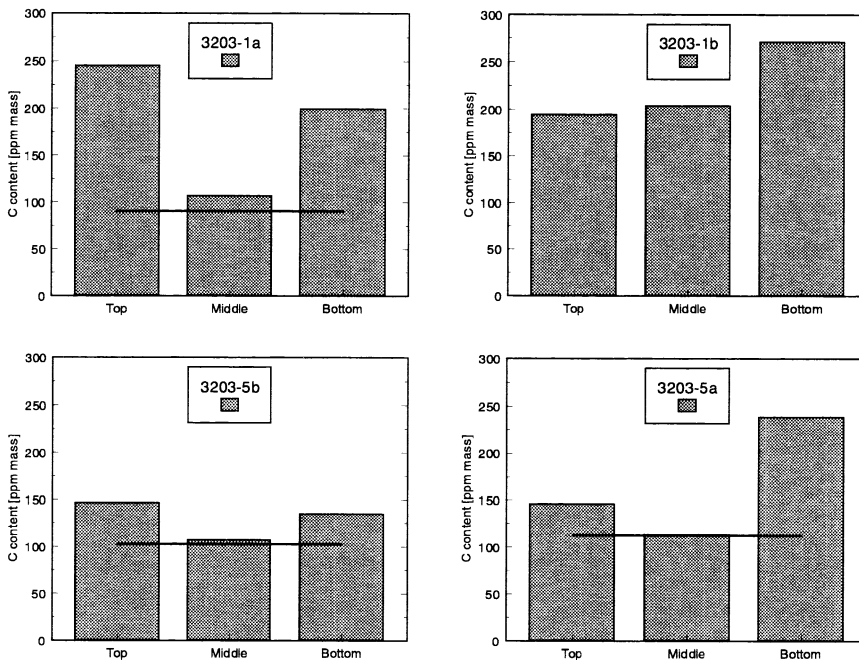


Figure 4.27: Carbon content in cast samples taken from the topmost, from the middle and the bottom part of mould 1 and 5 out of the of heat number 3203. The line across represents the carbon content in the whole parallel sample. For sample 3203-1b the analyses of the parallel sample showed 601 ppm and must have been contaminated during preparation.

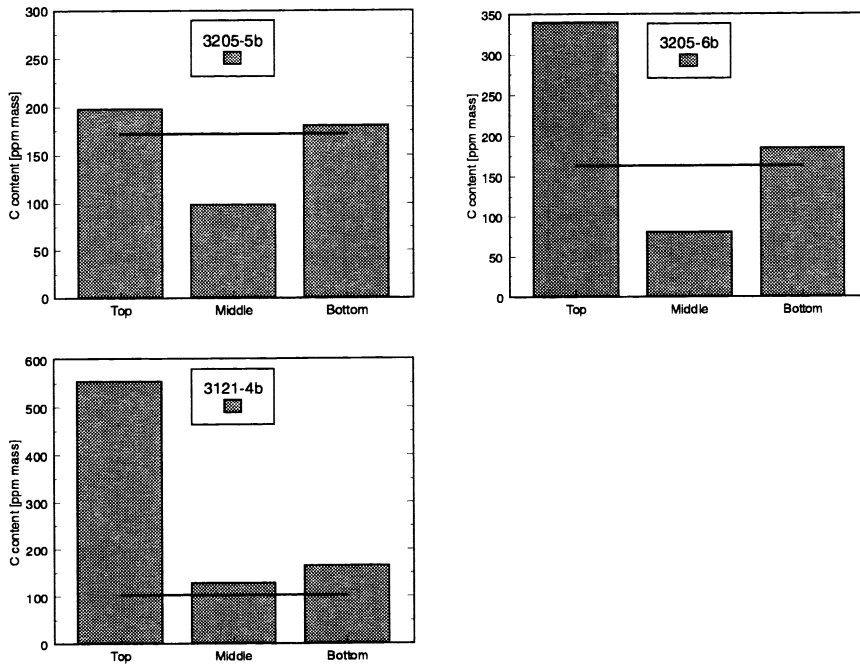


Figure 4.28: Carbon content in cast samples taken from the topmost, from the middle and the bottom part of mould 5 and 6 and from mould 4 from heat number 3205 and 3121. The line across represents the carbon content in the whole sample.

As seen from figs. 4.27 and 4.28 there are up to 5 times higher amounts of carbon in the top layer compared with the average content. These results seem to be in contradiction with the segregation theory, since the alloy is cooled from both top and bottom, and the final carbon-rich melt should be found in the centre of the casting. However, as pointed out previously particles will be wetted by oxidic phases present. Since the density of actual slag compositions are lower than the melt [25], these SiC containing slags will be found at the top.

As mentioned previously, a layer of small sized alloy protects the chill mould against wear by the teeming stream. This layer may pick up particles transferred by the bath movement caused by the teeming stream.

References

1. Klevan, O. S. and Engh, T. A., "Dissolved Impurities and Inclusions in FeSi and Si, Development of a Filter Sampler", *INFACON 7, Proceedings of the 7th International Ferroalloys Congress*, FFF, Trondheim (1995), pp. 441 - 451.
2. Bakke, P. and Klevan, O. S., "Thermodynamics of Liquid Silicon Bases Alloys," *Process Technology Conference Proceedings*, Vol. 14, ISS (1995)
3. Schei, A., Personal Communication, June 1996
4. HSC Chemistry Database: Barin, I., "Thermochemical Data for Pure Substances", VCH Verlags Gesellschaft, Weinheim, (1989) and (1993)
5. Powersim 2.5 Simulation Software Package, Powersim AS, Norway, (1996)
6. Bakke, P., "Carbon Removal from Molten Silicon by Gas Purging", *Elkem Internal Memo*, (1993)
7. Oeters, F., *Metallurgie der Stahlherstellung*, Springer-Verlag Verlag Stahleisen (1989) pp. 223-229.
8. Brimacombe, J. K., Nakanishi, K., Anagbo, P. E. and Richards, G. G., "Process Dynamics: Gas-liquid", *Elliott Symposium Proceeding* (1990)
9. Sano, M. and Mori, K., "Bubble Formation From Single Nozzles in Liquid Metals", *Transactions of the Japan Institute of Metals* **17** (1976) pp. 344-352
10. Engh, T. A and Nilmani, M., "Bubbling at High Flow Rates in Inviscid and Viscous Liquids (Slags)", *Metallurgical Transaction B* **19B** (1988) pp. 83-94
11. Okumura, K., Ban, M., Hirasawa, M., Sano, M. and Mori, K., "Rate of SiO₂ Inclusion Removal from Molten Cu to Slag Under Gas Injection Stirring Condition", *ISIJ International* **35** (1995) pp. 832-837.
12. Engh, T. A., *Principles of metal refining*. Oxford University Press, 1992
12. Anderson, N. M. and Engh, T. A. "Factors Affecting Bubble Residence Times in Gas Purged Reactors and Their Influence on Mass Transfer", *SINTEF Report no STF34 A87087*, Sintef Division of Metallurgy (1987)
14. Iguchi, M., Nozawa, K., Tomida, H. and Morita, Z., "Bubble Characteristics in the Buoyancy Region of a Vertical Bubbling Jet", *ISIJ International* **32** (1992) pp. 747-754.
15. Pilling, N. B. and Bedworth, R. E., "The Oxidation of Metals at High

- Temperatures”, *Journal of the Institute of Metals* **29** (1923) pp. 529-591
16. Remnes, S. and Kiland, O., ”Holdetidens innvirkning på karboninnholdet i FeSi 75% ved øsetapping hos Salten Verk”, *Elkem Internal Report F 196/84* (1984)
 17. Wennerhorn, C., Svenska Silikaverken AB, Köping, Sweden, Personal Communication
 18. Product Data Sheet from Svenska Silikaverken AB, Köping, Sweden
 19. Tveit, H., ”Størkning av 75 % Ferrosilicium, Forløp, Struktur og Styrke”, *Dr.ing. avh. 1988:53, Metallurg. Inst. NTH, Trondheim* (1988).
 20. Barraclough, K. G., *Properties of Silicon*, INSPEC, London and New York (1988) , pp. 296-298.
 21. Nozaki, T., Yatsurugi, Y. and Akiyama, N., ”Concentration and Behavior of Carbon in Semiconductor Silicon”, *Journal of Electrochemical Society* **117** (1970) pp.1566-1568
 22. Olesienski, R.W., Kanani, N. and Abbaschian, G. J., ”The P-Si (Phosphorous-Silicon) System” *Bulletin of Alloy Phase Diagrams.*, (6) (1985), pp. 130-133
 23. Yurkov, A. L., and Polyak, B. I, ”Contact Phenomena and Interactions in the System SiC-SiO₂-R_xO_y in Condensed Matter”, *Journal of Materials Science* **30** (1995) pp. 4469-4478
 24. Klevan, O.S. ”Granulering av Lav Aluminium Ferrosilicium 75”, *Elkem Internal Report TV/F 001/96* (1996)
 25. Tuset, J. K., ”Principles of silicon refining”, *International seminar on refining and alloying of liquid aluminium and ferro-alloys*, August 26 - 28, (1985) pp. 50 - 69

5. Discussion

In this chapter the results presented in chapter 3 “Sampling of Ferrosilicon for C-Analyses” and chapter 4 “Removal of C from liquid silicon and ferrosilicon” will be discussed further. As will be seen in the following discussions the topic pushing or engulfment of particles will be essential in the interpretation of the results regarding both the sampling of (ferro)silicon and carbon removal. An introduction to this topic is therefore given initially.

The final value of total carbon seems to depend on a number of mechanisms. These are in the following discussed in separate sections. It has been not possible to steady these mechanisms experimentally in sufficient detail. Therefore, verification experiments are suggested after each section.

5.1 Particle pushing or particle engulfment

When a moving solidification front intercepts an insoluble particle, it can either push it or engulf it. There are three basic theoretical approaches to describe the particle behaviour at a solid-liquid interface, the kinetic, the thermal and the thermodynamic model [1]. The kinetic approach is based on the simple idea that as long as a finite layer of liquid exists between the particle and the solid, the particle will be pushed. A critical interface velocity, u_{cr} , above which particles are engulfed, was postulated [1] and several models have been proposed. Uhlman et al. [2] gave the following equation for the critical velocity

$$u_{cr} = \frac{(n+1)}{2} \left(\frac{\Delta H_m \rho_1 a_0 V_0 D}{k T r_p^2} \right) \quad (5.1)$$

where n is a constant roughly equal to 5.0, ΔH_m is the latent heat of fusion, a_0 is the lattice constant and $V_0 = a_0^3$. D and r_p denote the diffusion coefficient in the liquid and particle radius respectively, whereas $k = 1.38 \times 10^{-23}$ J/K (Boltzmann's constant)

and T is the melt temperature.

However, these models seem to give too low values for the critical interface velocity. Rohatgi [2] found that even though the interface velocities of dendritic interfaces were about three orders of magnitude higher than the calculated critical velocities according to eqn (5.1) the particles were rejected.

There is a growing interest in a thermal conductivity criterion to characterize particle behaviour in front of a melt interface. Zubko et al. [3] showed that when the thermal conductivity of the particle is less than the thermal conductivity of the melt; that is $\lambda_p < \lambda_l$, the particle could not be captured or engulfed, thus it was pushed. From figure 2.11 it seen that the thermal conductivity of β -SiC is between 14 and 34 W/(mK) at the melting point of silicon. Thus, silicon carbide particles in silicon should be pushed since the thermal conductivity of liquid silicon is 55 W/(mK). The thermal conductivity of FeSi75 is also found to be around 55 W/(mK) in the actual temperature range, cf fig. 2.8, and according to the criterion of Zubko SiC will not be entrapped by the growing solidification front.

Rohatgi [2] and Surappa and Rohatgi [4] found that the heat diffusivity¹ criterion described in equation (5.2) provides excellent agreement with observations on particle entrapment in nonmetallic and metallic systems.

$$\left[\frac{\lambda_p c_p \rho_p}{\lambda_l c_l \rho_l} \right]^{1/2} < 1 \quad \text{for particle pushing} \\ > 1 \quad \text{for particle engulfment} \quad (5.2)$$

According to [6] this relation is limited to low growth rates u ; $ur_p/\lambda_l \leq 1$ (in cgs units).

For the case of SiC particles in liquid silicon at 1412 °C the heat diffusivity of particles, $\lambda_p c_p \rho_p$, over the heat diffusivity of the melt, $\lambda_l c_l \rho_l$, is 0.88. Taking liquid FeSi75 at 1350 °C gives the value 0.76 for the relation heat diffusivity of particles over heat diffusivity of the melt, resulting in particle pushing.

¹ The product $\lambda c \rho$ is called the heat diffusivity [5], whereas $\lambda c \rho$ is the thermal diffusivity.

Stefanescu et al. [1] have taken the differences in thermal conductivity of particle and liquid into account in the following model for the critical growth velocity

$$u_{cr} = \frac{\Delta\sigma_0 d_0}{6(n-1)\mu r_p} \left(2 - \frac{\lambda_p}{\lambda_l} \right) \quad (5.3)$$

where $\Delta\sigma_0 = \sigma_{ps} - (\sigma_{pl} + \sigma_{sl})$ is the difference in surface tension, d_0 is the interatomic distance for the liquid, μ is the viscosity of the melt and r_p is the radius of the particles. Stefanescu et al. [7] have later modified this equation by including gravitational forces

$$u_{cr}' = \frac{1}{6\mu r_p} \left[\frac{\Delta\sigma_0 d_0}{2} \left(2 - \frac{\lambda_p}{\lambda_l} \right) \pm \frac{4}{3} r_p^3 g \Delta\rho \right] \quad (5.4)$$

In this case $\Delta\sigma_0 = \sigma_{ps} - \sigma_{pl}$. The last term in eqn (5.4), which is Stoke's equation, is here written with \pm to take into account solidification from both top and bottom.

To calculate $\Delta\sigma_0$, the surface tension between particle and liquid, σ_{pl} , between particle and solid, σ_{ps} , and between solid and liquid, σ_{sl} is needed. The surface tension between the SiC particle and liquid (ferro)silicon is calculated from Young's equation, $\sigma_{pv} - \sigma_{pl} = \cos\theta\sigma_{lv}$. Using the data presented in table 5.1 gives $\sigma_{pl} = 1.166$ N/m for the SiC-S system and 1.194 N/m for the SiC-FeSi system. Engh [8] has proposed the following relation for the surface tension between solid and liquid for silicon (see also [9])

$$\sigma_{sl} = \frac{0.26\Delta H_m}{N_A^{1/3} V_m^{2/3}} \quad (5.5)$$

This gives $\sigma_{sl} = 0.312$ N/m. The surface tension between particle and solid, σ_{ps} has not been found for the system SiC and Si, but according to Stefanescu et al. [7] an equation-of-state approach can be used to calculate the surface tension between particle, liquid and vapour:

$$\sigma_{pl} = \frac{(\sigma_{pv}^{1/2} - \sigma_{lv}^{1/2})^2}{1 - K(\sigma_{pv}\sigma_{lv})^{1/2}} \quad (5.6)$$

Since all the surface tensions in eqn. (5.6) is known, the constant can be calculated to be $K = 0.6659 \text{ m/N}$ for the system SiC-Si(l)-Si(s). Stefanescu et al. [7] then calculated σ_{ps} from eqn. (5.6) by replacing σ_{lv} with σ_{sv} . The surface tension between solid and vapour, σ_{sv} is given by the following relation [10]

$$\sigma_{sv} \approx 1.2 \sigma_{lv} \quad (5.7)$$

The surface tension between particle and solid is now calculated to be $\sigma_{ps} = 1.57 \text{ N/m}$. Jena et al. [11] have given the interface energy for α -SiC with a layer of Si and Al surfaces to be about 0.1 eV/\AA^2 which corresponds to 1.6 N/m . A surface tension between particle and solid of 1.6 N/m gives $\Delta\sigma_0 = 0.1 \text{ N/m}$.

TABLE 5.1: Some physical data for SiC, liquid silicon and ferrosilicon at elevated temperatures. References given in brackets.

	SiC (ch. 2.4)	Si (l)	FeSi75 (l)
Thermal conductivity, λ [Wm ⁻¹ K ⁻¹]	30.37 at 1350 °C 29.36 at 1410 °C (fig. 2.11)	55 [8]	55 at 1350 °C (fig.2.8)
Specific heat capacity, c [J kg ⁻¹ K ⁻¹]	1286 at 1350 °C 1293 at 1410 °C (fig. 2.10)	Table 2.3 968 932	
Contact angle, θ , in system SiC-(Fe)Si- vac./Ar		40 (table 2.5)	30 (ch. 2.4.4)
Surface tension, σ [N/m]	1.844 [1]	0.86 (eqn. 2.10)	0.75 (fig. 2.5)

The critical velocity, u_{cr} , from eqn. (5.3) for the system Si-SiC is presented in figure 5.3 along with the velocity for solidification of ferrosilicon in an iron mould and in the Minco sampler. The casting is taken to be 100 mm thick. According to [12] this gives a velocity between 50 and 100 $\mu\text{m/s}$. The velocity of the solidification front in the Minco sampler is expected to be between 1500 -1850 $\mu\text{m/s}$. This assumption is based on the fact that it takes between 3 and 5 seconds from the sampler is out of the metal bath and until we have knocked out the sample. The thickness of the sample is 11.5 mm, cf. ch. 3.2. It should be pointed out that the critical velocity in figure 5.1 is only valid for a planar solid/liquid front. However the figure gives an indication of whether or not SiC particles in a melt of ferrosilicon with 75 mass% Si will be pushed by the solidification front. Investigation of the sample from the Minco immersion sampler indicates that the particles are randomly distributed in the sample. Line scanning of the Minco sample in the EPMA did not show that the concentration of carbon was higher at any particular spot in the sample.

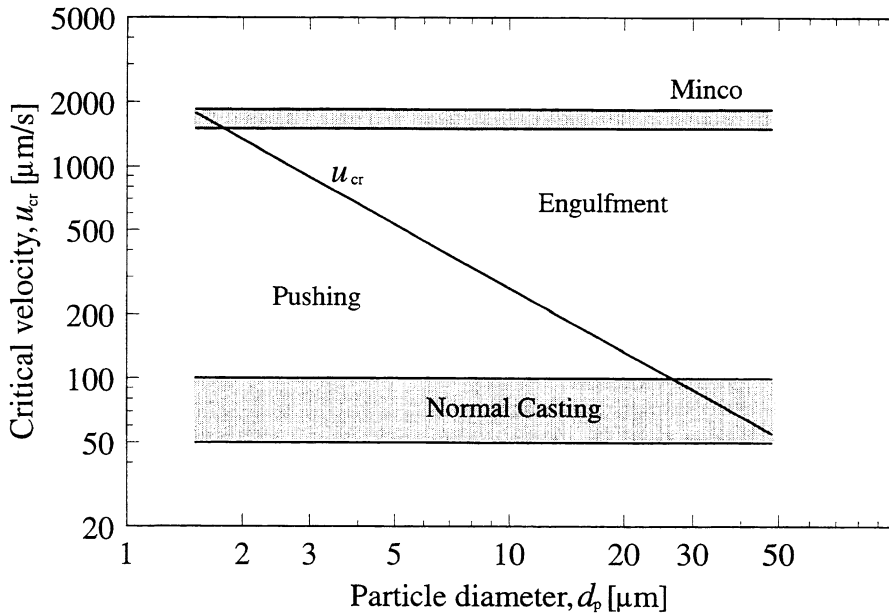


Figure 5.1: Calculated critical velocity of solidification by a planar interface from eqn. (5.3) where $\Delta\sigma_0 = 0.1$. The solidification velocities of FeSi75 cast in fines bed and in iron mould is taken from [12]. The casting is 100 mm thick. The velocity of the solidification front in the MINCO immersion sampler is assumed to be between 1500 and 1850 $\mu\text{m/s}$.

Future work

As pointed out here pushing and engulfment should play an important role in sampling, casting and refining of (Fe)Si. Due to discrepancies between the theories for the critical velocity, u_{cr} it would be valuable to specifically study the system SiC and Si or FeSi. Such experiments must include both low and high solidification velocities. Since it is necessary to have the size distribution of SiC particles in the melt, previous to solidification, the experiments have to be combined with filter sampling.

5.2 Sampling of liquid (ferro)silicon

When investigating the decarburization of liquid (ferro)silicon, reliable analyses for total carbon is required. Since carbon in liquid silicon-rich alloys is present as both dissolved carbon and silicon carbide particles, several considerations have to be taken when choosing sampling method or technique.

- i. the sampler must not separate or remove particles from the melt
- ii. solidification must proceed so rapidly that dissolved elements do not react with the sampler
- iii. the sampler must give a rapid solidification in order to reduce segregation of SiC- particles and dissolved carbon. The velocity of the solidification front, u , must be greater than the critical velocity for engulfment of silicon carbide particles in the liquid alloy, see figure 5.1.

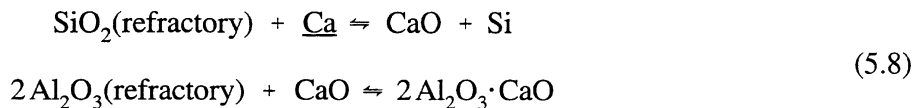
The type of samplers employed in normal operation was not considered in this project since they are made of graphite. It was therefore necessary to obtain or develop a suitable sampler.

The oxidic sampler tested was found to underestimate the carbon content in the alloy. Compared with the MINCO immersion sampler employed the difference is a factor $[\%C]_{\text{MINCO}}/[\%C]_{\text{oxidic scoop}} = 1.76$, see figure 3.2. This is most likely due to the transfer of silicon particles to the scoop wall by turbulence during filling. Theory

concerning turbulence removal to walls is cited in Appendix D.

Particles transferred to the wall of the scoop adhere or even penetrate into the wall as seen from figs. 4.14 - 4.17. The explanation is probably that a thin layer of the scoop wall softens and gives a thin liquid film of the system $\text{SiO}_2\text{-CaO-Al}_2\text{O}_3$. This type of oxide wets silicon carbide particles almost perfectly, cf. chapter 2.4.4 and [13].

Looking at the composition of the oxidic scoop sampler, the content of CaO is only 0.4 mass%, see figure 3.1. However, the X-ray mapping shown in figure 4.14-4.17 indicates that there has been an increase in the calcium content in the outer part of the refractory towards the metal. When dissolved Ca in the melt comes in contact with the chamotte in the scoop wall, the following reactions may occur:



This should result in an increase of the calcium content in the refractory since the standard Gibbs energy for the sum of these two reactions is $\Delta G^0 = +12,542 - 23.97 \times T$ and thus is negative above 525 K. The reactions in eqn (5.7) indicate that Ca-analyses in samples drawn with this type of scoop sampler underestimate Ca. This is also substantiated by the results given in table 3.1 where the Ca content in samples taken with the Minco Immersion sampler gives a 53% higher content than the TK40 scoop sampler.

To sum up the Minco immersion sampler is suitable for sampling of ferrosilicon since it seems to fulfill the requirements listed in the beginning of this section. The sampler gives a rapid solidification of the melt that minimizes the segregation of dissolved elements in the specimen. The Minco sampler seems also to give engulfment of silicon carbide particles present in the melt and thus gives the correct value for total carbon.

5.3 Filter sampling of ferrosilicon

It is seen from figure 5.1 that it is important to know the size distribution of SiC in (Fe)Si to understand their behaviour during casting and in order to characterize the final product. As pointed out in section 3.4.2 the amount of particles collected in the filter is low compared to what should be expected from the carbon content in the melt and in the filtered metal. Two exceptions are the heats 666-1 and 923-1, which both concern refined ferrosilicon. The problem may be that particles are lost from the inlet of the filter during sampling and preparation. As mentioned in section 3.4.2 a cake in front of the filter could be difficult to preserve due to flow of metal back from the canister. Some particles have probably passed through the filter since the concentration of inclusions inside the filter did not fall to zero towards the outlet. This was also experienced by Bakke et al. [14].

As pointed out by P. Bakke et al. [14], a filter has a depth filtration capacity and is only able to capture a certain number of particles of a given size distribution. Cake filtration starts when the depth filter capacity is exhausted. On this basis the size distributions presented in figs. 3.10-3.12 and fig. 4.13 are expected to be representative although some particles have been lost. This number size distribution of inclusions in FeSi75 is decreasing exponential as expected from the literature [8,15].

Combined with the measurement of the total carbon and data concerning the solubility of carbon should allow us to give a complete picture of the distribution of SiC particles.

Future work

The low values of total carbon obtained in filtered refined ferrosilicon, see section 3.4.2 and table 3.4, suggest that the metal be almost free of SiC particles and that the measured carbon content reflects the solubility level. Thus, development of improved filters (smaller pores than in the filter employed here) should make it possible to determine the solubility of carbon in equilibrium with SiC for various Si-rich alloys.

5.4 Removal of C from liquid Si and FeSi

5.4.1 Decarburization model

The mathematical model for decarburization of (Fe)Si presented in chapter 4 agrees well with experimental data, see figs. 4.2 - 4.6. The mass transfer coefficient for decarburization of silicon metal with oxygen and inert gas (Ar and/or N₂) is found to be $k_C = 5 \times 10^{-6}$ m/s. As discussed in section 4.1.2 k_C may be somewhat higher than 5×10^{-6} m/s, but considerably lower than the mass transfer coefficient for the melt boundary layer, roughly 10^{-4} m/s. The explanation given for this low mass transfer coefficient was formation of a dense silica layer on the bubbles resulting in a high resistance against diffusion of carbon monoxide into the bubbles, see fig. 4.7. One way to get around this problem could be to add oxygen as small silica particles, by for instance injection, instead of oxygen gas. In figure 5.2 this situation is described in a schematic way.

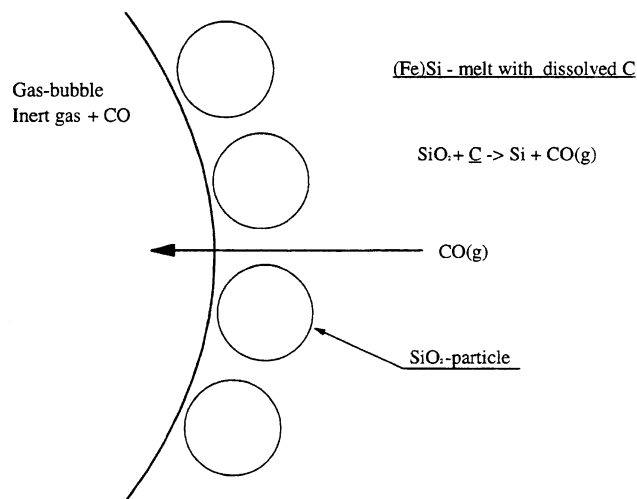


Figure 5.2: Schematic illustration of the effect of adding oxygen to liquid (ferro)silicon as silica with an inert carrier gas. Compared to a system where oxygen is added as a gaseous phase, see figure 4.7, the mass transfer coefficient, k_C , is expected to increase.

K. Sakaguchi and M. Maeda [16] performed some laboratory experiments with decarburization of silicon by adding silica at the top of the melt. Argon was injected on the surface of the melt and the system was kept under reduced pressure. Sakaguchi and Maeda [16] obtained a reduction in the carbon content on average from 180 ppm to below 20 ppm as shown in figure 5.3. The curves designated *Simulation* in figure 5.3 are obtained employing the decarburization model presented in chapter 4.1. The total pressure employed in the simulation, p_{tot} , varied from 1 to 0.1 bars and the contact area was set equal to the interface between metal and the top layer of silica. The amount of metal and surface area and specific gas flow of inert gas (NI/min, kg) is from Sakaguchi and Maeda [16] and from subsequent information from Maeda [17].

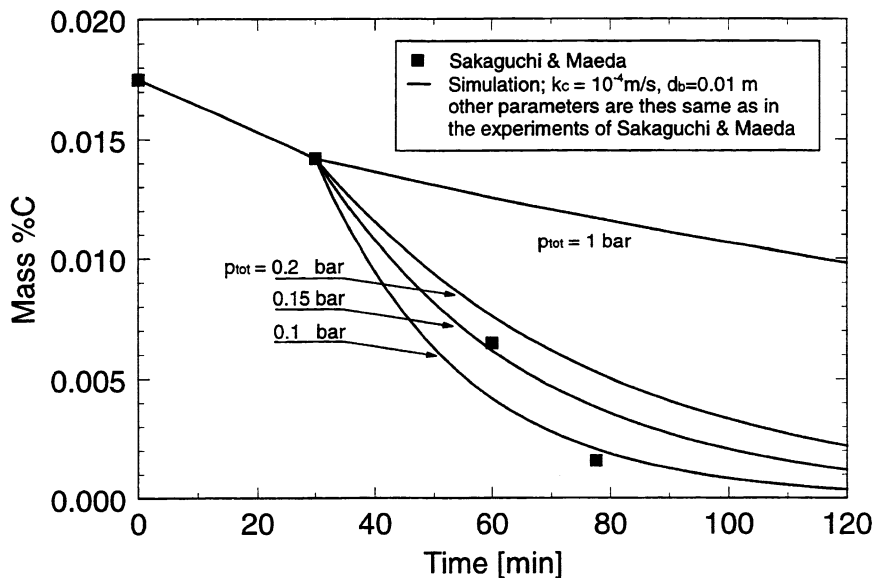


Figure 5.3: Decarburization with silica and argon at 1500 °C and simulation with the anticipated same parameters. ■ is experimental results from [16], Simulation is results from the Powersim decarburization model with $k_c = 10^{-4}$ and $d_b = 10$ mm. $V_{\text{melt}} = 83.1 \text{ cm}^3$, $A_t = 13.85 \text{ cm}^2$. \dot{Q}_{inert} is set to 0.25 NI/min.

The result from [16] presented in figure 5.3 indicates that addition of oxygen as silica and a reduction in total pressure may improve the decarburization rate.

Future work

The experiments performed by P. Bakke [18], which were presented in chapter 4 should be pursued further. Instead of adding silica at the top of the melt bath, silica particles could be injected at the bottom of the melt. Vacuum decarburization should also be investigated. The mathematical model presented in chapter 4.1 is not able to handle decarburization under vacuum. The use of mean pressure is no longer a valid approximation. Also there would probably be concentration gradients in the melt so that the assumption of complete mixing could not be employed. The decarburization model should therefore be developed further to describe this case. Experimental verification would be necessary.

5.4.2 Removal of particles to wall by stirring

From figure 4.21 it is seen that the rate of carbon removal by stirring is high during the first 5-10 minutes; then it slows dramatically. Investigations of the transition area between refractory and metal deposits show that silicon carbide particles have been transferred to the wall, see figs 4.14 - 4.18. The X-ray mapping in figure 4.18, which is taken from one of the experiments with pouring and subsequent Ar stirring, indicates that a viscous oxidic layer has been saturated with silicon carbide particles. Also the X-ray mapping pictures from the transition area in the oxidic scoop sampler indicate that the semi-molten area is filled with these particles. Thus it seems that the removal of carbon as SiC is limited by the capacity of this semi-molten layer to capture particles, and hence the removal rate will approach zero demonstrated in figs 4.12 and 4.21.

Future work

The mechanism of saturation of the semi-molten layer by silicon carbide particles should be pursued in new experiments. One possible practical method would be to insert a “sticky” inexpensive refractory material in the ladle during stirring with

inert gas. Then presumably an increased wall area will enhance removal of SiC particles.

5.4.3 Removal of carbon during casting, solidification and crushing and screening

The drop in carbon down to about 100 ppm in the cast sample may be due to the various mechanisms examined in chapter 4.4. Based on the discussion in section 5.4.1, oxidation of dissolved carbon during casting is expected to contribute only to a limited degree.

According to the investigation presented in subsection 4.4.2, the carbon content in ferrosilicon fines (-3 mm fraction) is on average 1.75 times higher than in the coarse fractions; +3 mm. This result may be due to segregation since the segregation coefficient for carbon in the melt, k_{eff} is lower than one, see chapter 4.4.2. Based on the discussion of the phenomena pushing and engulfment above, silicon carbide particles are most probably rejected by the solidification front during casting and solidification of FeSi75.

As pointed out in section 4.4.4 there is an increase in the carbon content in the topmost part of the cast alloy. The layer of the casting towards the chill mould also holds a higher carbon content than the whole sample. Typically, the carbon content these sections was 150 ppm higher. The removal of carbon to the top layer may be due to transport of slag to the top, whereas particles are expected to be transferred to the bottom layer of small sized ferrosilicon.

References

1. Stefanescu, D. M., Dhindaw, B. K., Kacar, S. A., and Moitra, A., "Behaviour of Ceramic Particles at the Solid-Liquid Metal Interface in metal Matrix Composites", *Metallurgical Transaction A* **19A** (1988) pp. 2847-2855
2. Rohatgi, P. K., "Interfacial phenomenon in cast metal-ceramic particle composites", *Interfaces in Metal-Matrix Composites, Symposium Proceedings* (1986) pp. 185-202
3. Zubko, A. M., Lobanov, V. G. and Nikonova, V. V., "Reaction of foreign particles with a crystallization front", *Soviet physics, Crystallography* **18** (1973) pp. 239-241
4. Surappa, M. K. and Rohatgi, P. K., "Heat diffusivity criterion for the entrapment of particles by moving solid-liquid interface", *Journal of Materials Science Letters* **16** (1981) pp. 562-564
5. Flemings, M. C., *Solidification Processing*. McGraw-Hill, 1974, pp. 9-10
6. Dahle, A. K., "Størkningssimulering av metall-matriks kompositter", *Diploma thesis*, NTH, Trondheim (1992)
7. Stefanescu, D. M., Moitra, A., Kacar, S. A. Dhindaw, B. K., "The Influence of Buoyant Forces and Volume Fraction of Particles on the Particle Pushing/Entrapment Transition during Directional Solidification of Al/SiC and Al/Graphite Composites", *Metallurgical Transaction A* **21A** (1990) pp. 231-239
8. Engh, T.A., *Principles of metal refining*. Oxford University Press, 1992
9. Nishi, Y., Igarashi, A., Kubo, Y., Ninomiya, N., and Mikagi, K., "Solid-Liquid Interfacial Energy of Pd-16 at% Si Glasses", *Materials Science and Engineering* **97** (1988) pp. 199-201
10. Murr, L. E., *Interfacial Phenomena in Metals and Alloys*. Addison-Wesley Publishing Company (1975), pp. 127
11. Jena, P., Shillady, D., and Arsenault, R. J., "Electronic and Structural Properties of Metal Matrix Composites", *Proc. Int. Conf. on Interfaces in Metal-Ceramics Composites*, TMS Annual Meeting, Anaheim, California, February 18-22, 1990.
12. Tveit, H., "Størkning av 75 % Ferrosilium, Forløp, Struktur og Styrke", *Dr.ing. avh. 1988:53, Metallurg. Inst. NTH, Trondheim* (1988) pp. 32- 40

13. Yurkov, A. L., and Polyak, B. I., "Contact Phenomena and Interactions in the System SiC-SiO₂-R_xO_y in Condensed Matter", *Journal of Materials Science* **30** (1995) pp. 4469-4478
14. Bakke, P., Nordmark, A., Bathen, E., and Engh, T. A. "Filtration of Magnesium by Ceramic Foam Filters", *Light Metals 1992, Ed.: E. R. Cutshall, TMS-AIME* (1992) pp. 923-935
15. Frisvold, F., "Filtration of Aluminium. Theory, Mechanisms, and Experiments", Dr.ing thesis, NTH (1990) pp. 155-156
16. Sakaguchi, K. and Maeda, M., "Decarburization of Silicon Melt for Solar Cells by Filtration and Oxidation", *Metallurgical Transaction B* **23B** (1992) pp. 423-427
17. Maeda, M., Personal Communication by E-mail (1996)
18. Bakke, P., "Carbon Removal from Molten Silicon by Gas Purging", *Elkem Internal Memo*, (1993)

6. Conclusions

A statistical examination of the carbon content in three different commercial qualities of FeSi75, Refined (low Al FeSi75), Gransil, and Standard lumpy, demonstrated that the refined quality is lowest in carbon. Granulation of ferrosilicon gives a product with a lower carbon content than the standard grade alloy. The variation in carbon content was almost the same for Gransil and refined and considerable lower than for standard FeSi75. Statistical tests of hypotheses showed a high confidence level for these conclusions.

Physical and thermodynamic data has been collected for liquid silicon and ferrosilicon. This is necessary in order to understand and model refining of these alloys. To simply ^{in the} treatment FeSi75 has been regarded as a Si-alloy.

Physical data, in addition to wetting data, for SiC was also collected and presented. It is found that the difference in density between SiC and liquid ferrosilicon with 74-78 mass% Si is so low that particles should not settle within times of practical interest.

The influence of sampling method on the measured values of the total carbon content in liquid ferrosilicon has been investigated. Quenching of the sample is essential to avoid segregation of dissolved carbon and pushing of SiC particles. The solidification velocity must exceed the critical velocity for engulfment of SiC particles. For instance the Minco type immersion sampler appears to fulfill these requirements. Oxidic scoop samplers seem to give too low values of total carbon due to removal of SiC particles from the melt.

Filter sampling of liquid ferrosilicon has been performed. The size distribution of particles obtained is assumed to be correct, and the mean particle diameter was found to be about 3 μm .

A decarburization model has been developed showing that removal of carbon by

oxidation of dissolved carbon is a slow process at atmospheric pressure. As far as can be seen the model agrees with experimental results. The low rate of carbon removal is probably due to formation of a dense silica layer on the bubble surface. Adding silica particles as the oxygen source may increase the rate of carbon removal. A further improvement is probably obtained by decarburization under vacuum, for instance by employing RH-type equipment.

The gas stirring experiments have shown that silicon carbide particles are removed by transfer to the ladle wall. The particles are found in a semi-molten and “sticky” transition area between metal and lining. The removal of particles seems to be limited by the capacity of this semi-molten layer to capture particles. When this transition area is saturated, the removal rate becomes small. This transfer mechanism is also taken to be the reason that the oxidic scoop sampler underestimates the carbon content in the melt.

The casting method of ferrosilicon has a strong influence on the final total carbon content in the commercial alloy. The predominant mechanisms in this case seem to be segregation of dissolved carbon and pushing of SiC particles. The removal of silicon carbide particles may also be enhanced by contact between a SiC-wetting oxidic phase (slag) and the molten FeSi.

Thus, shipped refined FeSi contains about 100 ppm total carbon, while the molten alloy contains roughly 200 ppm. The total carbon out of the FeSi-furnace is about 1000 ppm. This may be compared with 100 ppm level in shipped refined FeSi. It is hoped that further work in this area could allow a very substantial reduction of the content of carbon in (Fe)Si. Possibly low values of carbon could be attained on an industrial scale by injection of silica combined with the use of vacuum. Also the casting system could be designed to give low carbon in part of the product.

Appendix A: Statistics

Looking at the mean value and the standard deviation for the carbon content of the three products Gransil, Refined and Standard FeSi75 - see the tables below and figure 1.4-1.6 in chapter 1- it seems that Refined FeSi75 is lowest in carbon and that Standard FeSi75 has the highest carbon content. A two-sided 'Student' t -test¹ is used to see if there is a statistical significant difference in the C-content between these products.

TABLE A.1: Mean value of C content in samples of water-granulated FeSi75 (Gransil), Refined FeSi75 and Standard FeSi75 from Elkem Thamshavn in 1994

	Gransil®	Refined FeSi75	Standard FeSi75
Mean C-content [ppm mass]	196	112	266
SD_x [ppm mass]	75	71	121
\bar{s}_x [ppm mass]	6.2	14.8	19.1
Number of samples	144	23	40

¹ This was first deduced in 1908 by the chemist W. S. Gosset, who worked for the Guinness brewery in Dublin and wrote under the pseudonym "Student" [1]

TABLE A.2: Mean value of C content in samples of water-granulated FeSi75 (Gransil), Refined FeSi75 and Standard FeSi75 from Elkem Thamshavn in 1995

	Gransil®	Refined FeSi75	Standard FeSi75
Mean C-content [ppm mass]	233	114	283
SD_x [ppm mass]	96	37	167
\bar{s}_x [ppm mass]	7.5	4.5	21.4
Number of samples	162	68	61

TABLE A.3: Mean value of C content in samples of water-granulated FeSi75 (Gransil), Refined FeSi75 and Standard FeSi75 from Elkem Thamshavn for Q1-Q3, 1996

	Gransil®	Refined FeSi75	Standard FeSi75
Mean C-content [ppm mass]	201	135	323
SD_x [ppm mass]	53	49	236
\bar{s}_x [ppm mass]	4.5	9.8	22.3
Number of samples	140	25	112

To start with, the 1994 carbon content in Gransil and refined FeSi75 is compared. A null-hypothesis is that there is no difference, $H_0: \mu_1 = \mu_2$ or the alternative hypothesis there is $H_1: \mu_1 \neq \mu_2$. Here μ_1 and μ_2 are the average carbon contents in Gransil and refined FeSi75 respectively. The t -value for C content in the samples of Gransil and Refined is

$$t = \frac{\bar{X}_1 - \bar{X}_2}{SD_p \sqrt{\frac{1}{n_1} + \frac{1}{n_2}}} \quad (\text{A.1})$$

where \bar{X}_1 and \bar{X}_2 is the average content of carbon in the samples of Gransil and refined FeSi75, n_1 and n_2 is the number of samples. SD_p , is the pooled standard deviation for the two series defined as [2,3]

$$SD_p = \sqrt{\frac{(n_1 - 1) \times SD_1^2 + (n_2 - 1) \times SD_2^2}{n_1 + n_2 - 2}} \quad (\text{A.2})$$

Comparing the calculated t -value with tabulated values for the t distribution [4] tells us if we can reject the null-hypothesis. For Gransil and Refined FeSi75 for the 1994-data we get a t -value of 5.04 with $df = 165$ degrees of freedom, which corresponds to a P -value < 0.0001 and the null-hypothesis is rejected and the alternative hypothesis that the carbon content in Refined FeSi75 is lower than in Gransil is valid.

Comparison between Gransil and Standard FeSi75 for the same year gives $|t| = 4.53$ and the same conclusion can be drawn that the Gransil gives a significant lower C-content than standard FeSi75. From this we can also conclude that low Al must be lower in carbon than Std. FeSi75.

In table A.4 the $|t|$ -value along with the corresponding P -value is given for all the three years investigated.

TABLE A.4: Observed t values from the two-sided test comparing the C content in water-granulated FeSi75 (Gransil) versus Refined FeSi75 and Gransil vs. Standard FeSi75 and the corresponding P -value. The carbon analysis is from samples of shipments from Elkem Thamshavn for the period 1.1.1994 - 30.9.1996.

	Gransil® vs. Refined FeSi75		Gransil® vs. Standard FeSi75	
	$ t $	P -value	$ t $	P -value
1994	5.04	4.57e-07	4.53	5.92e-06
1995	9.97	0	2.80	0.0051
Q1-Q3, 1996	5.84	5.32e-09	5.95	2.76e-09

P -value = the probability of having a value of $|t|$ at least as great as the observed if there is not any difference between the two series compared

As seen from the above table there is an extremely small probability that the carbon content is equal in these products and we can therefore conclude that there is a significant difference in carbon contents so that $[\%C]_{\text{Refined}} < [\%C]_{\text{Gransil}} < [\%C]_{\text{Standard}}$.

Alternatively, since n_1 and n_2 are large, we may use the approximately normally distributed

$$Z = \frac{\bar{X}_1 - \bar{X}_2}{\sqrt{\frac{SD_1^2}{n_1} + \frac{SD_2^2}{n_2}}} \approx N(0,1) \quad (\text{A.3})$$

where SD_1^2 and SD_2^2 enter instead of σ_1^2 and σ_2^2 respectively. In the table below the Z - values are given with the corresponding P -values and it is seen that the conclusion is the same as with the t - test above.

An advantage of this statistic (A.3) is that it takes into account a possible difference in the standard deviations SD_1 and SD_2 [5].

TABLE A.5: Comparison of C content in shipment of Gransil vs. Refined FeSi75 and Gransil vs. Standard FeSi75 when assuming Z is normally distribution, $N(0,1)$. The shipments are for the period 1. January 1994 - 30. September 1996

	Gransil® vs. Refined FeSi75		Gransil® vs. Standard FeSi75	
	Z	P-value	Z	P-value
1994	5.22	1.73e-7	3.48	0.0005
1995	13.6	0	2.21	0.027
Q1-Q3, 1996	6.14	8.21e-10	5.3	7.77e-8

References

1. Box, G. E. P., Hunter, W. G. and Hunter J. S., *Statistics for Experimenters, An Introduction to design, Data Analysis and Model Building*, John Wiley & Sons, Inc (1978)
2. Spiegel, M. R., *Theory and Problems of Statistics*, Schaum Publishing Co., New York (1961)
3. Distance Teaching in Basic Statistics from University of Oslo, (1996)
4. Statistiske tabeller og formler, Tapir Forlag, Trondheim, Norway (1986)
5. Lindqvist, B. H., Personal Communication, NTNU, Trondheim, November 1996

Appendix B: Saltykov's Table

Saltykov's Table of Coefficients for Calculating Particle Distributions from Diameters [1]

	N _A (1)	N _A (2)	N _A (3)	N _A (4)	N _A (5)	N _A (6)	N _A (7)	N _A (8)	N _A (9)	N _A (10)	N _A (11)	N _A (12)	N _A (13)	N _A (14)	N _A (15)
N _V (1)	1.0000	0.1547	0.0360	0.0130	0.0061	0.0033	0.0020	0.0013	0.0009	0.0006	0.0005	0.0004	0.0003	0.0002	0.0001
N _V (2)		0.5774	0.1529	0.0420	0.0171	0.0087	0.0051	0.0031	0.0021	0.0015	0.0010	0.0009	0.0006	0.0006	0.0004
N _V (3)			0.4472	0.1382	0.0408	0.0178	0.0093	0.0057	0.0037	0.0026	0.0018	0.0013	0.0010	0.0007	0.0007
N _V (4)				0.3779	0.1260	0.0386	0.0174	0.0095	0.0058	0.0038	0.0027	0.0020	0.0016	0.0012	0.0009
N _V (5)					0.3333	0.1161	0.0366	0.0168	0.0094	0.0059	0.0040	0.0028	0.0021	0.0016	0.0013
N _V (6)						0.3015	0.1081	0.0346	0.0163	0.0091	0.0058	0.0041	0.0028	0.0022	0.0016
N _V (7)							0.2773	0.1016	0.0329	0.0155	0.0090	0.0057	0.0040	0.0029	0.0022
N _V (8)								0.2582	0.0961	0.0319	0.0151	0.0088	0.0056	0.0039	0.0028
N _V (9)									0.2425	0.0913	0.0301	0.0146	0.0085	0.0055	0.0039
N _V (10)										0.2294	0.0872	0.0290	0.0140	0.0083	0.0054
N _V (11)											0.2182	0.0836	0.0280	0.0136	0.0080
N _V (12)												0.2085	0.0804	0.0270	0.0132
N _V (13)													0.2000	0.0776	0.0261
N _V (14)														0.1925	0.0250
N _V (15)															0.1857

References

- DeHoff, R. T. and Rhines, F. N., *Quantitative Microscopy*, McGraw-Hill, New York (1968), p. 157

Appendix C: Numerical solution of eqn (4.26) - Powersim Model

Equation (4.26), ch. 4 can be written as

$$\frac{A(x(t) - B')}{x(t)} \frac{dx(t)}{dt} = 1 - \exp \left\{ - \frac{A(x(t) - B')}{B'} \frac{dx(t)}{dt} - C(x(t) - B')^2 \right\} \quad (C.1)$$

where [%C] = $x(t)$, $B' = B p_{\text{tot}}$ and $C = \phi_A / B p_{\text{tot}}$

At the suggestion of Wasbø [1], employing 1st order Euler-method, the derivative, $dx(t)/dt$, on the left-hand side can be approximated like this

$$\frac{dx(t)}{dt} = \frac{x(t + \Delta t) - x(t)}{\Delta t} \quad (C.2)$$

while to solve the implicit equation (C.1), the derivative on the right-hand side is substituted with the following approximation

$$\frac{dx(t)}{dt} = \frac{x(t) - x(t - \Delta t)}{\Delta t} \quad (C.3)$$

In the following: $x_k = x(t)$, $x_{k+1} = x(t + \Delta t)$, $x_{k-1} = x(t - \Delta t)$

Equation (C.1) can now be written as

$$\frac{A(x_k - B')}{x_k} \frac{(x_{k+1} - x_k)}{\Delta t} = 1 - \exp \left\{ - \frac{A(x_k - B')}{B'} \frac{(x_k - x_{k-1})}{\Delta t} - C(x_k - B')^2 \right\} \quad (C.4)$$

Equation (C.4) is now solved for x_{k+1}

$$x_{k+1} = x_k + \frac{x_k \Delta t}{A(x_k - B')} \left[1 - \exp \left\{ - \frac{A(x_k - B')}{B'} \frac{(x_k - x_{k-1})}{\Delta t} - C(x_k - B')^2 \right\} \right] \quad (\text{C.5})$$

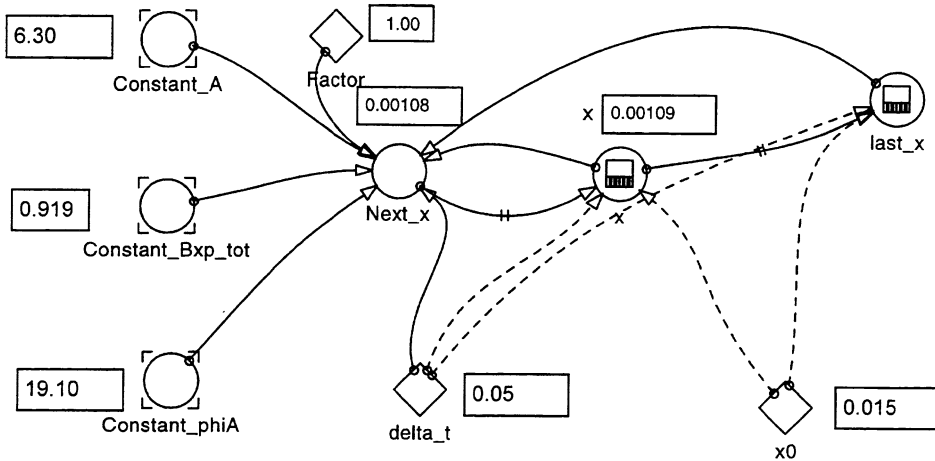
Using small time-steps, Δt , it is now possible to solve this equation numerically. The numerical solution is here performed employing the software package Powersim™. On the following pages the printout of the Powersim model is presented. The first five pages give the layout of the model, whereas the three last pages in this appendix give all the equations in the model. The data can be transferred to a text file for further treatment.

References

1. Wasbø, S. O., Personal Communication, Trondheim, NTNU, March 1995

Removal of Carbon from Si (l) and FeSi (l)

Numerical values are the same as in fig. 4.8, see eq. (4.26)



Input values

[large bubbles, $d_b > 15$ mm, $u_b = 0.711 \cdot \text{SQRT}(9.81 \cdot (d_b))$
 $d_b = f(Q, \sigma, \rho)$ but max. 40 mm]

Type of melt

0=Si, 1= FeSi

1.00



Melt_type

Temp. (OC)

1,600.00



Melt_temp

Melt volume (m3)

1.60



Volume_melt

Nozzle orifice (m)

0.002



Nozzle_orifice

Gas flow (Nm3/h)

15.00



Nm3perh

Input [%C]

0.015



x0

Height of bath

1.40



Bath_height

Mass transfer coeff.

0.0001



k_t

%C_in for different type of alloy and at different melt temperature

Type	1450	1500	1550	1600	1650	1700
Si	75	108	153	213	291	391
Si w/1%Al	89	127	178	246	334	447
FeSi75	50	73	104	145	200	271
FeSi75 w/1%Al	61	87	124	172	236	317

The constants A and B in the model see eqn. (4.26)

A

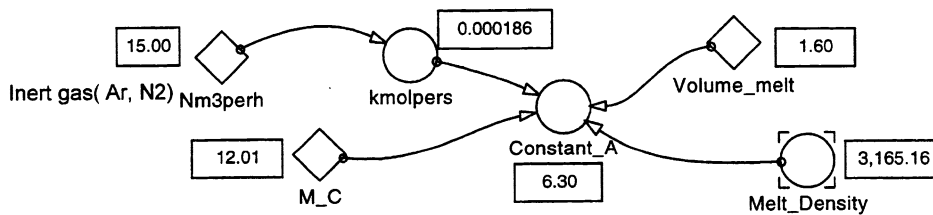
A = Volume of melt [m3] x density of melt [kg/m3] OVER 100 x molecular weight of C kg/kmol] x flow of Nitrogen [kmol/s]*3600 s/h

Volume of melt is 1.6 m3

Density of liquid (Fe)-Si-alloy
= f(mass% Si, T); see under C

Atomic weight of C is 12.011 kg/kmol

Flow of inert gas: 0 to 60 Nm3/h



B

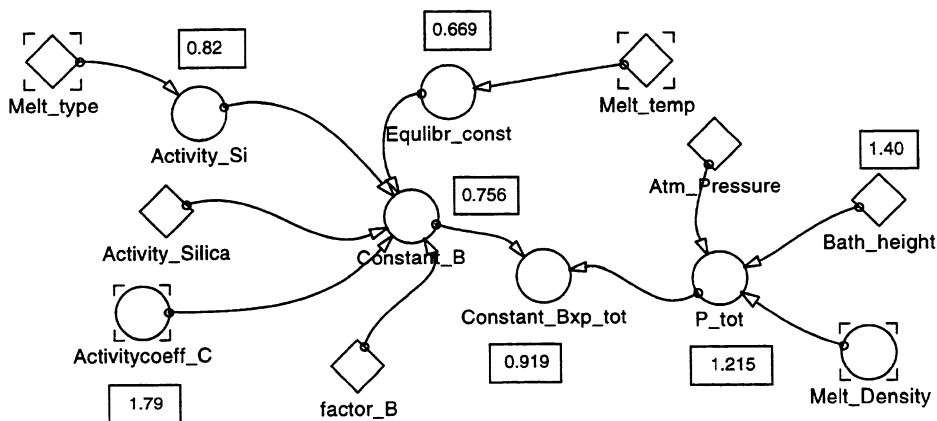
B = total pressure x (activity of Si OVER activity of silica) ^0.5 x 1 OVER (equilibrium constant x activity coefficient of carbon)

Total pressure = 1.2

Activity of silica and the activity coeff. of C is

Activity of silicon is 1 in pure liq. silicon and 0.83 in pure liq. FeSi75

The equilibrium constant $K = \exp(18.3 - 35,101/T)$



The constant phi_A in the model see eqn. (4.26)

phi_A

$$\text{phi_A} = (\text{Total bubble area [m}^2\text{]} \times \text{density of melt [kg/m}^3\text{]} \times \text{mass transfer coeff. [m/s]} \times \text{B}) \text{ OVER } (100 \times \text{atomic weight of C [kg/kmol]} \times \text{flow of inert gas [kmol/s]})$$

$$\text{Total bubble area (A_b)} = \text{Specific bubble area} \times \text{number of bubbles}$$

$$\text{Specific bubble area} = \text{phi} \times \text{square bubble diameter (d_b)}$$

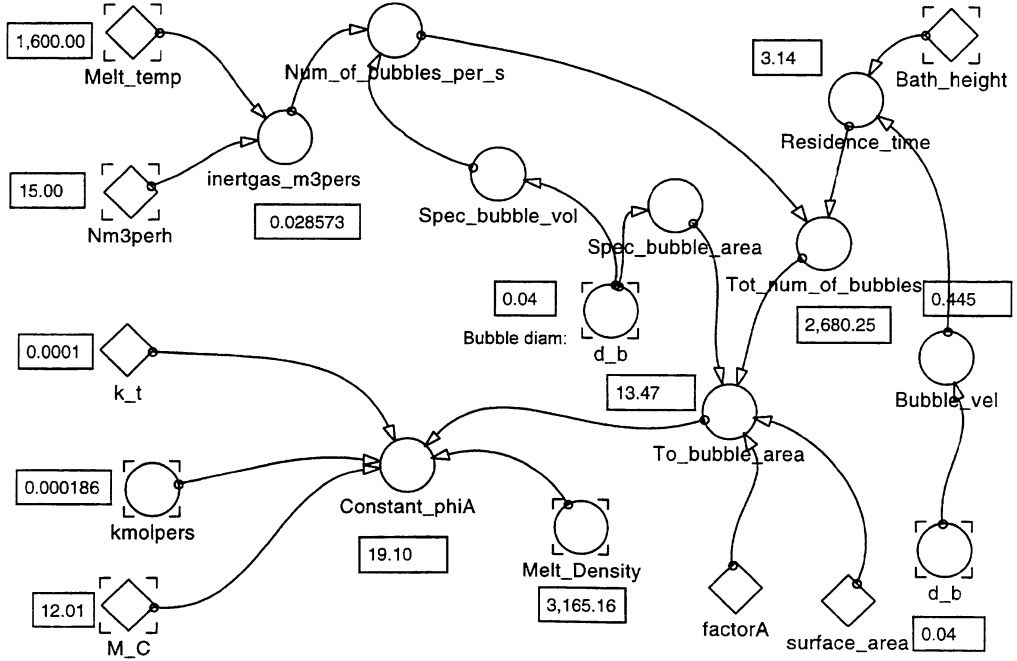
$$\text{Bubble diameter (d_b)} = 2$$

$$\text{Number of bubbles (N_b)} = \text{Number of bubbles per second} \times \text{residence time}$$

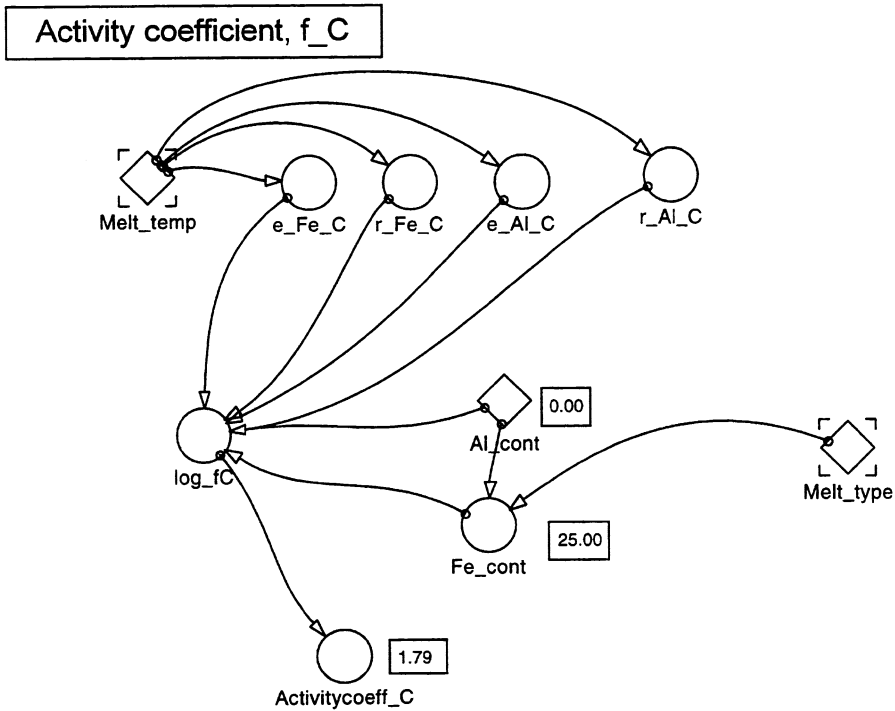
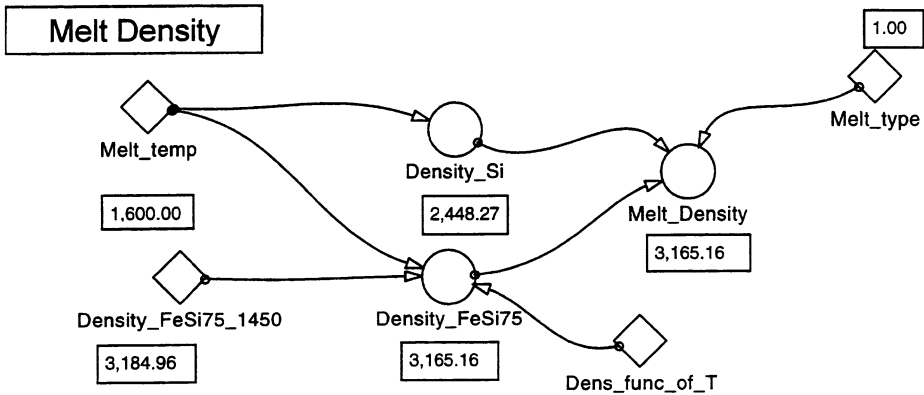
$$\text{Number of bubbles per second} = \text{Inert gas flow rate (m}^3\text{/s)} \text{ OVER specific bubble volume (m}^3\text{)}$$

$$\text{Inert gas flow rate (m}^3\text{/s)} = [\text{Inert Gas (Nm}^3\text{/h)} \text{ OVER } 3600 \text{ s/h}] \times [\text{Temperature of gas at nozzle orifice (K)} \text{ OVER } 273.15 \text{ K}]$$

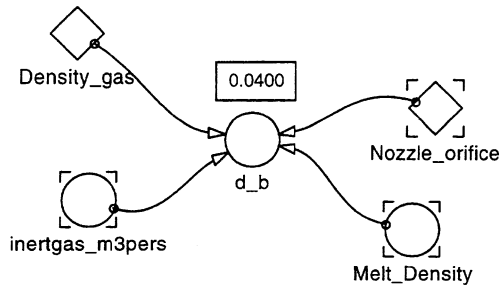
$$\text{Residence time (s)} = \text{Height of metal bath (m)} \text{ OVER velocity of a single bubble (m/s)}$$



The activity coefficient and the melt density cf. chapter 2.1 and 2.2

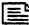





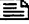



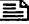
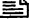




Calculation of bubble diameter (cf. Appendix D) and data transfer



 Transfer with file "C:\DATA\DR_INGAVHANDLI\DEKARB.SIM\DEKARB4.TXT"

- Activity_Si
= IF(Melt_type=1, 0.82, 1)
☒ Melt_type = 1 => FeSi75; i. e. a_Si=0.82, whereas Melt_type = 0 => Si-metal with a_Si=1
- Activitycoeff_C
= 10^{log_fC}
- Bubble_vel
= 0.711*SQRT(d_b*9.81)
- Constant_A
= (Volume_melt*Melt_Density)/(100*M_C*kmolpers)/3600
☒ The constant A is amount of gas over amount of melt. Deviding with 3600 s/h gives the time in hours and gives a smaller value of the constant A
- Constant_B
= (Activity_Si/Activity_Silica)^{0.5}/(Activitycoeff_C*Equibr_const)*factor_B
☒ The constant B takes care of the theremodynamics, see eq (4.10)
- Constant_Bxp_tot
= Constant_B*P_tot
- Constant_phiA
= (To_bubble_area*Melt_Density*k_t)/(100*M_C*kmolpers)
☒ PhiA_A er et dimensionless contact area given by eq. (4.15). Phi_A = (bubble area [m2] x mass transfer coeff. [m/s] x melt density [kg/m3]) OVER (100 x molar weight of C [kg/kmol] x kmol inert gas per sec [kmol/s])
- d_b
= IF((((3*inertgas_m3pers*(Nozzle_orifice/2)^{0.5})/(PI*9.81^{0.5}*(Density_gas/Melt_Density)^{0.25}))^{1/3})>0.04,0.04,(((3*inertgas_m3pers*(Nozzle_orifice/2)^{0.5})/(PI*9.81^{0.5}*(1.42/Melt_Density)^{0.25}))^{1/3}))
- Density_FeSi75
= IF(Dens_func_of_T=1, Density_FeSi75_1450 - 0.132*(Melt_temp-1450), Density_FeSi75_1450)
- Density_Si
= 2534-0.456*(Melt_temp-1412)
☒ Density for Si(l) from thesis based on Yaws et al.
- e_Al_C
= 0.0304-174.54/(Melt_temp+273.15)
- e_Fe_C
= 0.0165-15.24/(Melt_temp+273.15)
- Equibr_const
= EXP(-35069/(Melt_temp+273.15)+18.32)
☒ Equibr. constant given by eq (4.6), ch. 4
- Fe_cont
= IF(Melt_type=1, (25-Al_cont), 0)
- inertgas_m3pers
= (Nm3perh/3600)*((Melt_temp+273.15)/273.15)
☒ Amount of gas going into the metal bath per sec. is Q/3600 multiplied with T/273.15 (correction for the expansion due to temperature)
- kmolpers
= Nm3perh/(3600*22.414)
☒ kmol inert gas per sec. = volume flow inert gas (Nm3/h) over 3600 s/h and 22.414 Nm3/kmol
- last_x
= DELAYPPL(x,delta_t,x0)
☒ Value of C at the previous time step
- log_fC
= e_Al_C*Al_cont+e_Fe_C*Fe_cont+r_Al_C*Al_cont²+r_Fe_C*Fe_cont²
- Melt_Density
= IF(Melt_type=1, Density_FeSi75, Density_Si)
- Next_x
= x+(x*delta_t/(Constant_A*(x-Constant_Bxp_tot)))*(1-Factor*EXP(-Constant_A*(x-Constant_Bxp_tot)*(x-last_x)/(Constant_Bxp_tot*delta_t)-Constant_phiA*(x-Constant_Bxp_tot)²/Constant_Bxp_tot))
☒ Calculation of C-content at next time step
- Num_of_bubbles_per_s
= inertgas_m3pers/Spec_bubble_vol
- P_tot
= 0.5*(Atm_Pressure+Atm_Pressure+Melt_Density*9.81*Bath_height/(1.013*10⁵))
- r_Al_C
= 2.5e-5-0.07/(Melt_temp+273.15)

- r_{FeC}
= $-4.84 \cdot 10^{-4} + 1.0374 / (\text{Melt_temp} + 273.15)$
- Residence_time
= Bath_height/Bubble_vel
 The bath height in meter / bubble velocity in m/s
- Spec_bubble_area
= $\text{PI} \cdot d_b^2$
- Spec_bubble_vol
= $4/3 \cdot \text{PI} \cdot (d_b/2)^3$
- To_bubble_area
= IF(factorA=0, Spec_bubble_area*Tot_num_of_bubbles, surface_area)
- Tot_num_of_bubbles
= Num_of_bubbles_per_s*Residence_time
- x
= DELAYPPL(Next_x, delta_t,x0)
 present value of carbon
- ◇ Activity_Silica
= 1
- ◇ Al_cont
= 0
 Zero for "pure" FeSi75
- ◇ Atm_Pressure
= 1
- ◇ Bath_height
= 1.4
- ◇ delta_t
= .05
 Length of each time step in hours (entire multiples of the length of the time step given in Simulation setup)
- ◇ Dens_func_of_T
= 1
 If 1, the density is dependant of the temperature as shown in Density_FeSi75. If 0 is the density constant and equal to 3185 kg/m3
- ◇ Density_FeSi75_1450
= $7106 \cdot \text{EXP}(-0.0107 \cdot 75)$
 Density for FeSi(l) at 1450 C from thesis based on Dumay and Cramb
- ◇ Density_gas
= 1.42
 This is the density of a 50/50 argon and air mixture
- ◇ Factor
= 1
 Factor=0; the exponential component in next x (eqn. 4.25) is diregarded. This is equal to the case of equilibrium as described in eqn. 4.29.
- ◇ factor_B
= 1
- ◇ factorA
= 0
 Bubblesr=>factorA=0, only surface of the bath=>factorA=1
- ◇ k_t
= $1e-4$
- ◇ M_C
= 12.011
- ◇ Melt_temp
= 1600
- ◇ Melt_type
= 1
 FeSi75=1 and Si-melt=0
- ◇ Nm3perh
= 15
 In Nm3/h
- ◇ Nozzle_orifice
= $2e-3$
 Size of nozzele

- ◇ surface_area
 - = 1.385e-3
 -  Surface area if no bubbles, Maeda & Sakaguchi
- ◇ Volume_melt
 - = 1.6
- ◇ x0
 - = 150e-4
 -  Start value for Carbon content

Appendix D: Rising Velocity of Bubbles in Liquids

Large contact area is achieved with small bubbles and low rising velocity, see equation (5.36). However, creating small bubbles is difficult in a metallurgical gas injection system. Therefore, only rising velocity for bubbles of intermediate size and large bubbles are discussed here, cf. figure D1.

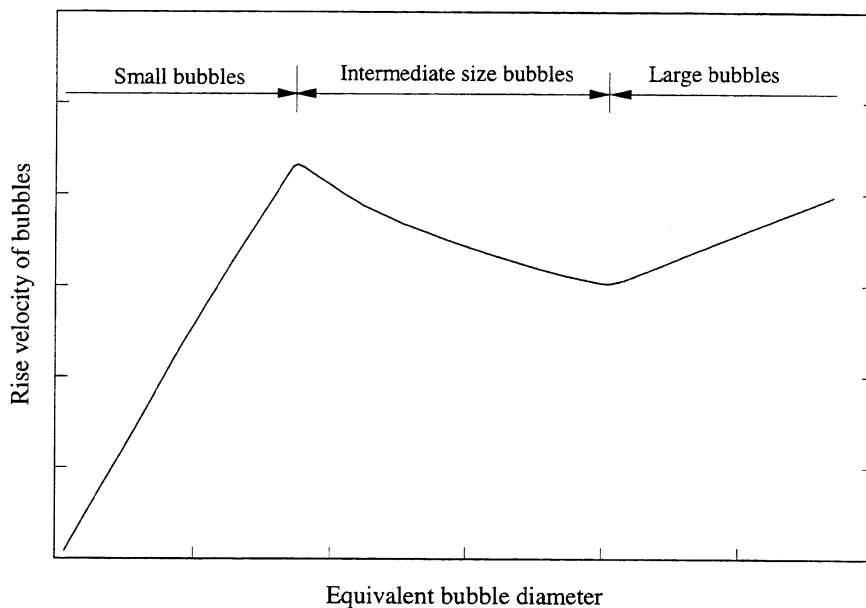


Figure D.1: Free rise velocity of gas bubbles in liquid metal (for instance Si). The bubbles size is given as equivalent spherical diameter [1].

Intermediate size bubbles

The rising velocity of bubbles in liquids is described in chapter 7.6 in the textbook Principles of Metal Refining by T. A. Engh [1]. The rise velocity depends on the equivalent bubble diameter as shown in figure D1. For $Re > 100$, the bubbles in water tend to oscillate strongly which is effecting the drag. Oscillation depends on

the interplay between gravitational, viscous, surface tension, and inertial forces. The dimensionless groups Morton, M , and Eötvös, Eo , have proved to be useful in describing the behaviour of bubbles.

$$M = \Delta\rho\rho^2g\frac{v^4}{\sigma^3} \quad (D.1)$$

and

$$Eo = \frac{\Delta\rho gd_b^2}{\sigma} \quad (D.2)$$

In contaminated liquids we have [1,2]

$$ReM^{0.149} + 0.857 = 3.42H^{0.4441} \quad \text{if } M < 10^{-3} \text{ and } Eo < 40 \quad (D.3)$$

where

$$H = \frac{4}{3}EoM^{-0.149}(\mu/\mu_w)^{-0.14} \quad \text{if } H > 59.3 \quad (D.4)$$

From equation (D.3) we get the Reynolds number and we can calculate the bubble velocity

$$u_b = \frac{Re \times v}{d_b} \quad (D.5)$$

From chapter 2.2 we have the following physical data for liquid silicon and FeSi75 at 1500 °C

TABLE D.1: Physical data for Si (l) and FeSi75(l) at 1500 °C

	Silicon	ref.	FeSi75	ref.
Density, ρ [kg/m ³]	2,499	eqn (2.4)	3,185 ¹⁾	eqn (2.6)
Surface Tension, σ [N/m]	0.86	eqn (2.10)	0.75 ²⁾	fig. 2.5
Kinematic Viscosity, ν [m ² /s]			0.338×10 ⁻⁶	fig. 2.7
Viscosity, μ [Ns/m ²]	7.02×10 ⁻⁴	eqn (2.11)		

¹⁾ at 1450 °C ²⁾ at 1600 °C

For bubbles in liquid silicon we have $M = 1.49 \times 10^{-15}$ and further for a bubble with $d_b = 0.004$ m, the Eötvös number, $Eo = 0.456$. Since $M < 10^{-3}$ and $Eo < 40$ we have $H = 102$. With also the requirement for H fulfilled, we obtain the Reynolds number, Re to be 4,133 by employing equation (D.3). This gives then a bubble velocity, $u_b = 0.289$ m/s for a bubble with diameter 0.004 m.

In figure D.1 the rising velocity of bubbles in liquid silicon and ferrosilicon with 75 mass% Si is presented for bubble diameters from 3 to 15 mm. The relation between the rising velocity and bubble diameter can be described by a polynomial of order three. For liquid silicon we have

$$u_b = -14,844 \times d_b^3 + 604.63 \times d_b^2 + 10.321 \times d_b + 0.3215 \quad (D.6)$$

and for liquid FeSi75

$$u_b = -13,929 \times d_b^3 + 566.22 \times d_b^2 + 9.6327 \times d_b + 0.2979 \quad (D.7)$$

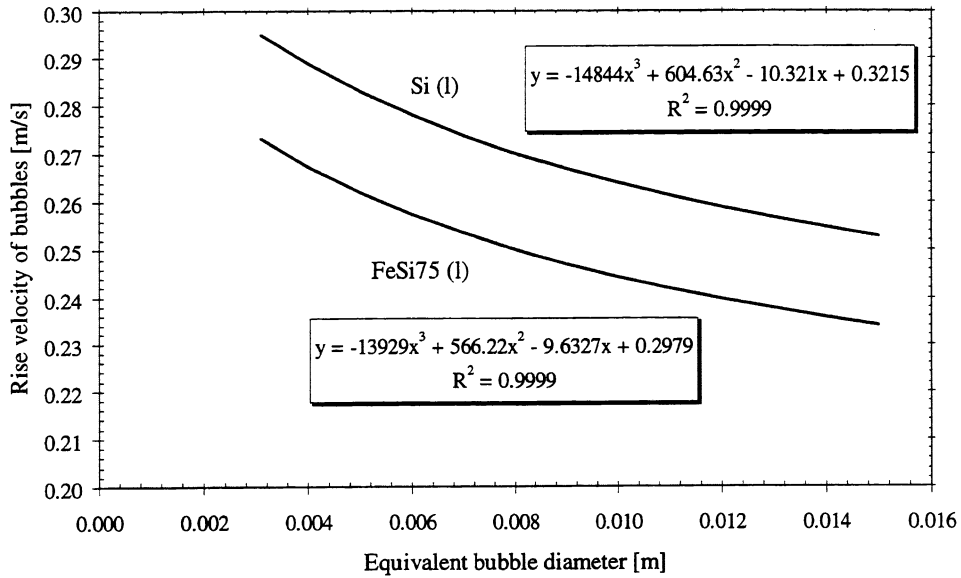


Figure D.2: Calculated free rise velocity of bubbles of intermediate size in liquid silicon and FeSi75; $3 < d_B \leq 15$ mm. The bubble is assumed spherical.

Large bubbles

For bubbles greater than 15 mm, the following relation from R. Clift et. al [2], is employed

$$u_b = 0.711\sqrt{gd_e\Delta\rho/\rho}; \quad Re > 150, \quad Eo \geq 40 \quad (\text{D.8})$$

where the d_e is the diameter of a volume equivalent sphere

References

1. Engh, T. A., *Principles of metal refining*. Oxford University Press (1992), pp. 317-319
2. R. Clift, J. R. Grace and M. E. Weber, *Bubbles, Drops, and Particles*. Academic Press (1978), pp. 203-207

Appendix E: Turbulent Removal of Particles and Specific Stirring Power

E.1 Turbulent removal to walls and top slag

The fluid mechanics of transfer of particles in molten metal to the walls or top slag in a ladle is treated by several authors [1-3].

In the following it is assumed that once an inclusion touches the wall it adheres to it and due to turbulence the inclusions are completely mixed in the bulk melt. According to classical hydrodynamic theory a boundary layer is present at the melt-wall interface as shown schematically in figure A.1. The boundary layer is split up into three parts as originally proposed by Levich [4]; the turbulent wall layer, the restricted turbulence layer at distance δ_1 from the wall and the inner viscous layer with laminar flow.

From [1] we have

$$-c_{\delta_1}(a) = \frac{\dot{n}_a \left(\frac{1}{e^2} - \frac{1}{\delta_1^2} \right) \times v^2}{u_o^3 \times 2.88 \times 10^{-3}} \quad (\text{E.1})$$

This equation applies only when the protrusion height e is less than the boundary layer thickness δ_1 . For the region $\delta_1 < z < \delta_b$ one may according to [1] use the equation of the Reynolds analogy

$$-\frac{\dot{n}_a}{\tau_o} = \frac{c_b(a) - c_{\delta_1}(a)}{\rho(u_m - u_{\delta_1})} \quad (\text{E.2})$$

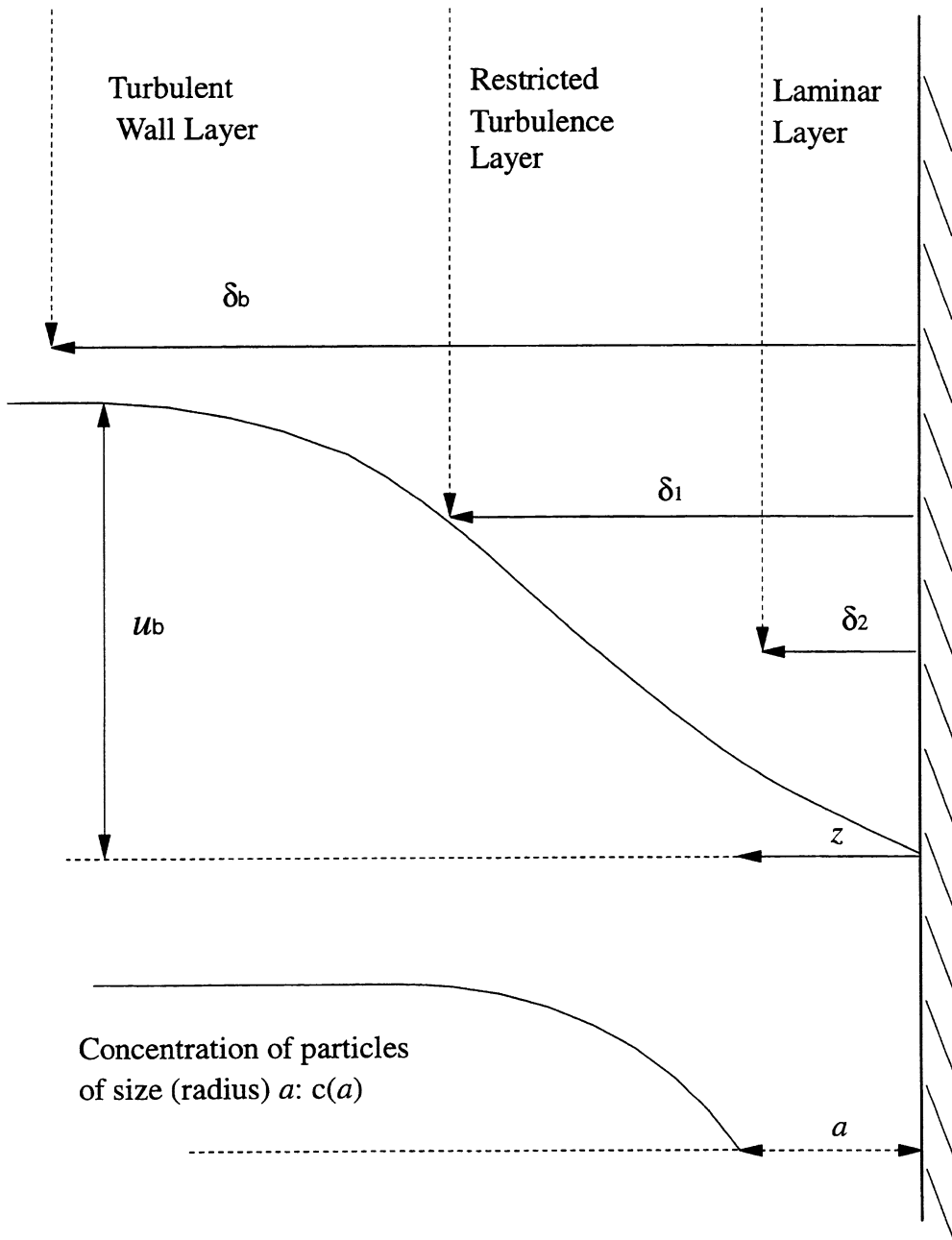


Figure E.1: Velocity and particle concentration along a ladle wall [1]

where $c_b(a)$ is the concentration of inclusions of size a and u_m is the mean velocity in the pipe and u_{δ_1} is the velocity at $z = \delta_1$. The basis for eqn. (5.40) is the assumption that the mean eddy length for the transfer of mass and momentum are the same. Thus concentration and velocity vary proportionally to each other. \dot{n}_a is proportional to $c_b(a) - c_\delta(a)$ and $-\tau_0$ is proportional to $\rho(u_m - u_{\delta_1})$. Then the ratio between \dot{n}_a and $-\tau_0$ is given by equation (5.40). The velocity, u_{δ_1} , between the restricted turbulence layer and the turbulence wall layer is equal to $5u_0$. Furthermore, according to [1], the thickness of the restricted turbulence layer δ_1 decreases with u_0 as $\delta_1 = 5\nu/u_0$. Eliminating δ_1 and u_{δ_1} from eqns. (5.39) and (5.40) gives

$$-\frac{\dot{n}_a}{c_b(a)} = \frac{1}{\frac{1}{u_m \phi} + \phi^{\frac{1}{2}} \left(\frac{347\nu^2}{e^2 u_0^2} - 19 \right) / u_m \phi} \quad (\text{E.3})$$

where

$$\phi = \frac{u_0^2}{u_m^2} = \frac{\tau_0}{\rho u_m^2} \quad (\text{E.4})$$

is the friction factor for the pipe. The denominator on the right-hand side in equation (5.42) gives the total resistance in the two boundary layers and $1/(u_m \phi)$ is the resistance in the turbulent wall layer.

Resistance in the restricted turbulence layer dominates when the protrusions are small and equation (5.41) can be simplified to

$$-\frac{\dot{n}_a}{c_b(a)} \approx \frac{u_m \phi^{1/2} e^2 u_0^2}{347\nu^2} \quad (\text{E.5})$$

while resistance to particle transfer prevails for large e giving

$$-\frac{\dot{n}_a}{c_b(a)} \approx u_m \phi \quad (\text{E.6})$$

Equation (5.44) is then valid for the turbulent wall layer.

The specific stirring power, $\dot{\epsilon}$, is according to Kolmogorov [4] proportional to the flow of kinetic energy per unit mass, that is to the third power of the mean velocity.

In the terms of the shear velocity this gives

$$\dot{\epsilon} = \frac{uv_0^3}{l_e} \quad (\text{E.7})$$

where l_e is a characteristic length of the energy containing eddies. Equation (5.45) says that $\dot{\epsilon}$ is proportional to u_0^3 with $1/l_e$ as the proportionality constant. For pipe flow it is found experimentally that l_e is proportional to the diameter d and has a weak dependence on the Reynolds number [4].

$$l_e = 0.05 d \text{Re}^{-\frac{1}{8}} \quad (\text{E.8})$$

where $\text{Re} = u_m d/v$. For resistance in the restricted turbulent layer, eqn. (5.43) we get for the mass transfer coefficient $k_t = \dot{n}_a/c_b(a)$

$$-\frac{\dot{n}_a}{c_b(a)} = \frac{\dot{\epsilon} e^2 \text{Re}^{-1/8} d 144 \times 10^{-4}}{v^2} \quad (\text{E.9})$$

while equation (5.44) valid when resistance is determined by the turbulent wall layer, becomes

$$-\frac{\dot{n}_a}{c_b(a)} = 0.37 \dot{\epsilon}^{1/3} \phi^{1/2} \frac{1}{2} \text{Re}^{-1/24} d^{1/3} \quad (\text{E.10})$$

E.2 Specific Stirring Power

The specific stirring power by gas stirring with a gas flow \dot{G} , mol per second is composed of two parts as shown in the following equation taken from [1]

$$\dot{\varepsilon} = \frac{\dot{G}}{M} \left[RT \ln \left(1 + \frac{p_{\text{in}}}{p} \right) + R(T - T_{\text{in}}) \right] \quad (\text{E.11})$$

One part is due to the decrease in static pressure from p_{in} to p when the gas bubbles rise from the inlet to the outlet. The second part arises from thermal expansion of the gas from the inlet temperature T_{in} to the melt temperature T . The last term is disregarded by some authors. F. Oeters [5] state that the gas is most likely heated at the nozzle orifice and therefore produce no expansion work on the metal in the ladle. Keeping the expansion work, equation (E.11) can be transformed to

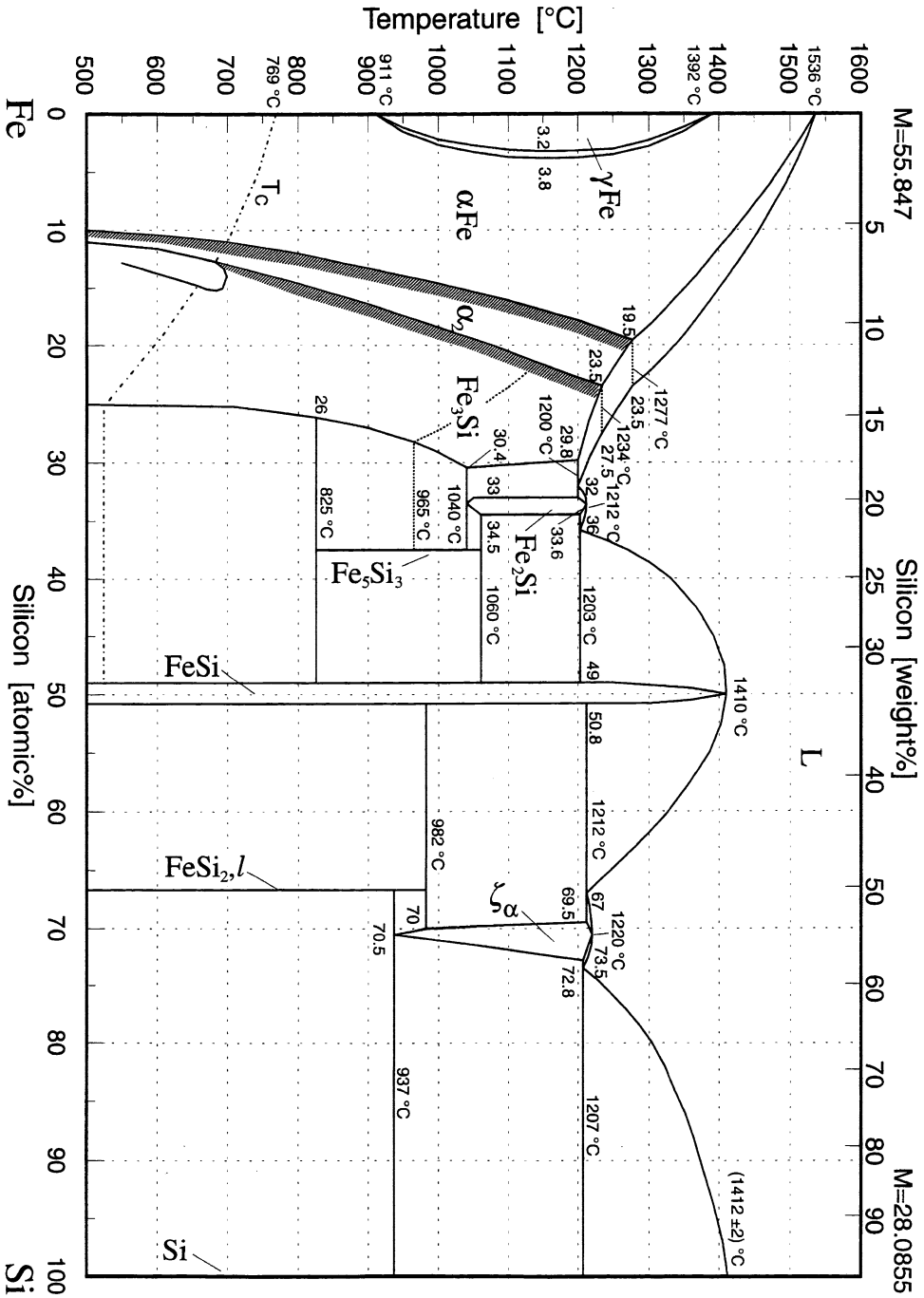
$$\dot{\varepsilon} = \frac{\dot{Q} \times R}{M \times 22.414 \times 60} \left[T \ln \left(1 + \frac{\rho g H}{1.013 \times 10^5} \right) + (T - T_{\text{in}}) \right] \quad (\text{E.12})$$

where \dot{Q} , is the flow of gas in NI/min and H is the depth of the metal bath in meter. g is the acceleration of gravity and ρ is the melt density in kg/m^3 .

References

1. Engh, T. A., *Principles of metal refining*,. Oxford University Press (1992), pp. 263-276.
2. Sandberg, H., Engh, T., Andersson, J. and Olsson, R., "Omröringens betydelse vid Al-desoxidation i en ASEA-SKF-skänkugn", *Jernkontorets Annaler* **155** (1971) pp. 201-216 (in Swedish).
3. Engh, T.A. and Lindskog, N., "A fluid mechanical model of inclusion removal", *Scandinavian Journal of Metallurgy* **4** (1975) pp. 49-58.
4. Davies, J. T., *Turbulence Phenomena*, Academic Press (1972)
5. Oeters, F., *Metallurgie der Stahlherstellung*, Springer-Verlag Verlag Stahleisen (1989) pp. 252-254.

Appendix F: Fe-Si Phase-Diagram



Redrawn by E. Hoel after O. Kubaschewski, Iron-Binary Phase Diagrams, Springer-Verlag, Berlin, 1982, p 136-9

Appendix G: Chemical analyses of fines and lumpy FeSi75

TABLE G.1: Analyses of 0-1, 1-3 and +10 mm fractions. Samples drawn during production at the crushing and screening plant on three different days, one day with refined FeSi75 (10. October 1996). Carbon is analysed employing the LECO CS125 combustion analyser, whereas the other elements are analysed on a Philips PW1480 X-ray spectrometer. # of parallel is the number of parallel samples.

	7.10.96.			10.10.96			16.10.96.		
	0-1 mm	1-3 mm	+10 mm	0-1 mm	1-3 mm	+10 mm	0-1 mm	1-3 mm	+10 mm
%Si	73.24	75.51	75.85	73.43	75.26	75.87	71.66	75.00	75.98
%Al	0.675	0.626	0.545	0.126	0.118	0.050	0.604	0.572	0.497
%Ca	0.153	0.144	0.098	0.069	0.088	0.010	0.121	0.113	0.041
%Ti	0.060	0.058	0.044	0.049	0.049	0.040	0.072	0.065	0.064
%P	0.009	0.010	0.010	0.010	0.011	0.011	0.009	0.010	0.012
%Mn	0.048	0.042	0.040	0.043	0.040	0.039	0.043	0.046	0.045
%Fe	25.69	23.62	23.52	26.01	24.35	24.04	27.23	24.15	23.55
%Cr	0.010	0.009	0.008	0.012	0.011	0.011	0.012	0.010	0.009
%Cu	0.005	0.004	0.003	0.003	0.002	0.002	0.006	0.005	0.005
%Mg	0.044	0.015	0.005	0.046	0.040	0.016	0.078	0.026	0.011
%Ni	0.002	0.002	0.002	0.004	0.003	0.003	0.003	0.003	0.002
%C	0.035	0.034	0.020	0.023	0.019	0.011	0.037	0.032	0.020
Sum	99.96	100.07	100.15	99.82	99.99	100.10	99.87	100.03	100.24
ppm C	350	340	201	234	191	106	368	318	201
# of parallel	2	2	2	4	4	4	4	4	4

